6-18-2021

An Engineered Tensile Energy Dissipation Device Exploiting a Cutting Deformation Mode

Anthony Gudisey
University of Windsor

Recommended Citation
Gudisey, Anthony, "An Engineered Tensile Energy Dissipation Device Exploiting a Cutting Deformation Mode" (2021). *Electronic Theses and Dissertations*. 8598.
https://scholar.uwindsor.ca/etd/8598

An Engineered Tensile Energy Dissipation Device
Exploiting a Cutting Deformation Mode

by

Anthony Gudisey

A Thesis

Submitted to the Faculty of Graduate Studies

through the Department of Mechanical, Automotive and Materials Engineering

in Partial Fulfillment of the Requirements for

the Degree of Master of Applied Sciences

at the University of Windsor

Windsor, Ontario, Canada

An Engineered Tensile Energy Dissipation Device Exploiting a Cutting Deformation Mode

by

Anthony Gudisey

APPROVED BY:

H. Hu

Department of Mechanical, Automotive & Materials Engineering

A. Chernaiev

Department of Mechanical, Automotive & Materials Engineering

W. Altenhof, Advisor

Department of Mechanical, Automotive & Materials Engineering

March 26, 2021

Declaration of Co-Authorship / Previous Publication

I. Co-Authorship

I hereby declare that this thesis incorporates material that is result of joint research, as follows:

Chapters 2, 3 and 7 contain material published within a peer-reviewed journal paper which was developed in collaboration with John Magliaro and Professor William Altenhof. The analytical modelling was performed in collaboration with John Magliaro. I certify that I interpreted the data and took a leading role in authoring and preparing this journal paper.

Chapter 3 contains an illustration published in an SAE journal paper. It was written in collaboration with Professor William Altenhof and John Magliaro. I certify that I interpreted the data and took a leading role in authoring and preparing this journal paper.

I am aware of the University of Windsor Senate Policy on Authorship and I certify that I have properly acknowledged the contribution of other researchers to my thesis and have obtained written permission from each of the co-author(s) to include the above material(s) in my thesis.

I certify that, with the above qualification, this thesis, and the research to which it refers, is the product of my own work.

II. Previous Publication

This thesis includes 2 original papers that have been previously published/submitted for publication in peer reviewed journals, as follows:

Thesis Chapter	Publication title/full citation	Publication status*
Chapter [2, 3, 7]	A. Gudisey, J. Magliaro and W. Altenhof, "High capacity, adaptive energy absorption under tensile loading conditions utilizing an axial cutting deformation mode," Forces in Mechanics, vol. 2, 2021, https://doi.org/10.1016/j.finmec.2020.100004.	*Published*
Chapter [3]	Gudisey, A., Altenhof, W., and Magliaro, J., "Experimental Investigation of Axial Cutting of AA6061 Extrusions under a Tension Deformation Mode," SAE Int. J. Adv. & Curr. Prac. in Mobility 2(6):3116-3125, 2020, https://doi.org/10.4271/2020-01-0206.	*Published*

I certify that I have obtained written permission from the copyright owner(s) to include the above published material(s) in my thesis. I certify that the above material describes work completed during my registration as a graduate student at the University of Windsor.

III. General

I declare that, to the best of my knowledge, my thesis does not infringe upon anyone's copyright nor violate any proprietary rights and that any ideas, techniques, quotations, or any other material from the work of other people included in my thesis, published or otherwise, are fully acknowledged in accordance with the standard referencing practices. Furthermore, to the extent that I have included copyrighted material that surpasses the bounds of fair dealing within the meaning of the Canada Copyright Act, I certify that I have obtained written permission from the copyright owner(s) to include such material(s) in my thesis.

I declare that this is a true copy of my thesis, including any final revisions, as approved by my thesis committee and the Graduate Studies office, and that this thesis has not been submitted for a higher degree to any other University or Institution.

Abstract

The current state-of-the-art for sacrificial tensile energy absorbers presents a plethora of issues, ranging from, but not limited to, erratic fluctuations, unrepeatability and unstable force responses. Energy absorption in a tensile application is a field of study where limited research has been conducted, in comparison to compressive energy absorption. Axial cutting, a mode of energy absorption which has been studied extensively under compressive experimental conditions, provides steady force-displacement responses. The impetus of this study involves the design of a novel test apparatus to implement axial cutting in a tensile mode of deformation. A pre-existing analytical model was utilized to design, size and precisely engineer energy absorbers with adaptive profiles to produce unique force responses under tensile loading. The experiments were conducted under a quasi-static loading condition, utilizing fixtures to modify a hydraulically powered tensile apparatus with a maximum loading capacity of 300 kN. AA6061 T6 and T4 extrusions were utilized as energy absorbers, with wall thicknesses varying from 0.799 mm to 3.175 mm. Tensile force efficiencies ranged from 75% to as high as 95%. Total energy absorption values ranged from 2.2 kJ to 7.7 kJ. Specific energy absorption values ranged from 12 kJ/kg to 16 kJ/kg. These values exceed standards imposed by currently existing tensile energy absorbers. High stability and repeatability were observed between tests, with limited variance. High accuracy numerical models were created and simulated on LS-DYNA ®. Validation metrics and cumulative errors of 0.904 and 0.095 were computed, respectively.

Dedication

To my father, William Gudisey for being a great role model and pushing to pursue my Master's degree, I greatly appreciate his support. My mother, Monica Eda and my sister, Maria Gudisey for their constant encouragement throughout my thesis. My partner, Liza-Anastasia DiCecco for being by my side and supporting me.

Acknowledgements

I would like to thank my advisor Dr. Altenhof for his guidance, moral and financial support throughout the course of my research at the University of Windsor. His direction and advice have been greatly helpful to me in the completion of my project. I have furthered my experience with designing within outlined constraints and restrictions, among other design challenges. I would like to emphasize my gratitude for his guidance during the numerical modelling procedure, leading to my exposure to the finite element solver LS-DYNA and pre/post processing software. These are skills which will be highly transferable in my engineering career.

Next, I would like to extend my thanks to the technicians at the University of Windsor, both in the Faculty of Engineering and with the Technical Support Center. In particular, I would like to thank Mr. David Tremblay, Mr. Kevin Harkai and Mr. Dean Poublon for machining material for me, as well as assisting me while I worked in the shop. Additionally, I would like to thank Mr. Brian Aldington from Anchor Danly for assistance with machining process of the fixturing utilized in this testing.

I would like to extend my thanks to Mr. John Magliaro for his assistance throughout my project, both in terms of experimentation and the analytical modelling approaches utilized within this study.

Finally, I would like to take this opportunity to express my gratitude to the Natural Sciences and Engineering Research Council (NSERC), the Ontario Graduate Scholarship (OGS) and the Queen Elizabeth II Graduate Scholarship (QEII-GST), for the financial support provided to me through this research.

Table of Contents

List of Tables

List of Figures

List of Appendices

List of Abbreviations/Symbols

AA	aluminum alloy
AISI	American Iron and Steel Institute
ALE	arbitrary Lagrangian-Eulerian
ASM	American Society for Metals
CFRP	carbon fiber reinforced plastic
CNC	computer numeric controlled
EFG	element-free Galerkin
FEA	finite element analysis
GFRP	glass fiber reinforced plastic
OD	outer diameter
PA	passive adaptive
PFAS	personal fall arrest system
SMP	shared memory processing
UNC	unified coarse
UNF	unified fine
WHO	World Health Organization

Nomenclature

A_c	contact area between blade and extrusion
B	half-width of wedge/blade shoulder
C	cumulative error
D_{ss}	distance between the plastic deformation tip and blade shoulder
E	elastic modulus of extruded material
F	total axial cutting resistance force
K_θ	membrane stretching coefficient
l_b	blade wedge length
n	number of cutting blades
P_m	mean cutting force
P_{max}	peak cutting force
R_a	axial bend radius for cut petalled sidewalls
r_i	inner radius of an extrusion
r_m	mean radius of an extrusion
r_o	outer radius of an extrusion
R_Q	relative error
R_r	rolling radius of curls at the side of the wedge/blade
SEA	specific energy absorption
t	wall thickness of an extrusion
T	blade tip width

TEA	total energy absorption
TFE	tensile force efficiency
V_M	validation metric

Greek Letters

δ	crosshead displacement
θ	wedge/blade semi angle
μ	coefficient of friction
σ_o	flow stress of extrusion material

Introduction

Impact conditions are present in a variety of situations including, but not limited to, vehicular collisions and accidental falls. These events are often accompanied by a combination of sudden accelerations and erratic forces. The World Health Organization estimates that the annual economic cost of these incidents is in the vicinity of $600 billion (USD) worldwide [1]. Sacrificial energy absorbers are utilized in these situations to mitigate injury and damage to the occupant. The current state-of-the-art for energy absorbers are accompanied by a variety of issues which can range from highly unstable force responses to high unpredictability and repeatability between repeated impact events. The ideal characteristics for energy absorbers include high force efficiency, high specific energy absorption, minimal inertial effects and strain rate insensitivity [2]. Extensive research has been conducted in the field of energy absorbers for compressive applications [3, 4] whereas significantly less research exists exploring high capacity and efficient tensile energy dissipation.

The motivation behind this study emanates from the fact that tensile energy absorbers are not as readily available as their compressive counterparts. In addition, the ones which are available are either highly specialized for specific purposes or are plagued with numerous issues similar to the compressive energy absorbers.

Axial cutting is a method of energy absorption which has been proven to eliminate high fluctuations in the force responses. It has been tested extensively under compressive loading conditions and varying loading rates, ranging from quasi-static to dynamic. A large array of cutting tools with varying blade numbers have been implemented during these experiments. Additionally, analytical modelling attempts are currently in place which provide high quality predictions in comparison to the experimental force responses [5, 6]. Numerical modelling schemes have also been employed to define the deformation modes present during this process, and to accurately predict the behaviour of extrusions under axial cutting [7, 8].

The impetus of this study is to design a test apparatus capable of implementing a tensile mode of deformation through axial cutting. A 4-bladed cutting tool will be utilized for this purpose and this tool is identical to the one presented in [9]. A currently existing machine within the Crashworthiness, Impact and Materials Deformation (CIMD) lab will be fit with fixtures to ready it for a tensile axial cutting test. The fixtures will be modelled and drafted on CATIA V5. The parametric scope for this study will include hollow extrusions made from AA6061 material including both constant thickness specimens and those with varying wall thickness to act as energy dissipation devices with passive adaptive force/displacement responses. The geometries of the passive adaptive energy dissipation structures will be designed based on analytical predictions. Numerical models will be created to replicate test conditions. Upon fabrication of the fixtures and extrusion material, experimental testing will be carried out. This study aims to illustrate the capacity of axial cutting to provide highly stable and repeatable force responses under a tensile deformation mode. Additionally, validation will be carried out between the analytical and numerical predictions, and experimental observations.

Chapter 1: Literature Review

Falls are classified as a leading factor contributing to worldwide injury and death [10]. Sacrificial energy absorbers implemented in these situations utilize progressive tearing of stitched fabrics [11, 12]. A myriad of stitching techniques are employed, however, they all generally produce force-displacement responses with similar erratic trends [11, 12]. The ideal properties of an energy absorber for this application requires a rigid, perfectly plastic material with no elasticity to eliminate any rebound. Due to the nature of the energy absorber, deformation mode and material, there is an inherent amount of elasticity left remaining in the system. This elasticity leads to rebounds which translate to force fluctuations.

The design and selection basis for personal fall arrest systems (P.F.A.S). are based on maintaining a pre-defined maximum load while not exceeding a certain amount of energy absorber extension [13]. This criterion provides a means of minimizing the amount of deceleration to levels which can be managed by the human body but does not mitigate them completely [14]. An illustration of a representative fall event and force response from this energy absorption method are illustrated in Figure 1. The representative loading regions are highlighted utilizing different colours and labels to correlate each region of the force response to its respective location during the fall event [15]. It can be seen in region 1 that the peak force in achieved fairly quicky, followed by subsequent fluctuations caused by inherent elasticity of the rope. Following this region, less pronounced ringing occurs indicating that the worker is swinging back and forth after the impact event. The sizing and selection of P.F.A.S. for individual workers is flawed and utilization of over or under sized energy absorbers can lead to further injury [16]. This is a problem which is more prevalent in relation to heavier workers, where this sizing and selection criterion does not function as robustly and higher peak forces and accelerations result and in severe cases, failure is observed [16, 17, 18].

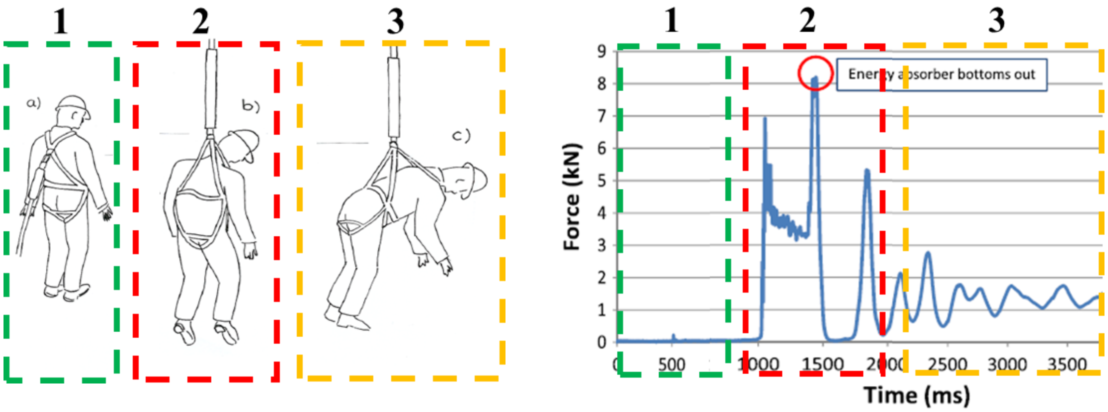

(a) (b)

Figure 1: a) Phases of fall event, b) representative force response caused by energy absorbers in P.F.A.S [11, 16].

Traffic collisions are a highly studied field of research. A myriad of energy absorbers have been designed to increase vehicle safety during low through high speed impact scenarios. It should be noted that these safety measures are implemented into the vehicle cabin and are designed to dissipate energy through deformation [19, 20]. 30% of vehicle collisions occur as a result of impact with a roadside barrier, as observed by the International Road Federation [21]. Road-side safety barriers are implemented along the sides of highways, narrow roads and sharp turns to prevent vehicles from veering into oncoming traffic in the opposite lane [22]. Vehicles impact along the barrier creates large scale elongation and tensile loading conditions. Three types of road-side safety barriers are commonly utilized for this purpose and are classified by their rigidity [23]. Metal cables hoisted along the road by posts provide high deformability, however the cable can become taught and can tear through the vehicle frame. Semi-rigid barriers provide a middle ground in terms of deformability and rigidity. Rigid barriers usually placed along highways, prevent off-roading in high speed environments. Rigid barriers experience limited deformation upon impact and consequently the energy absorption is carried out through deformation of the vehicle cabin. An experimental study recreating impact conditions was conducted by Jiang et al. and the representative deceleration vs time response is exhibited in Figure 2. Extremely large decelerations in the vicinity of 30 g were measured [24]. Decelerations of this magnitude have been proven to cause severe injury and in severe cases, death [25, 26, 27].

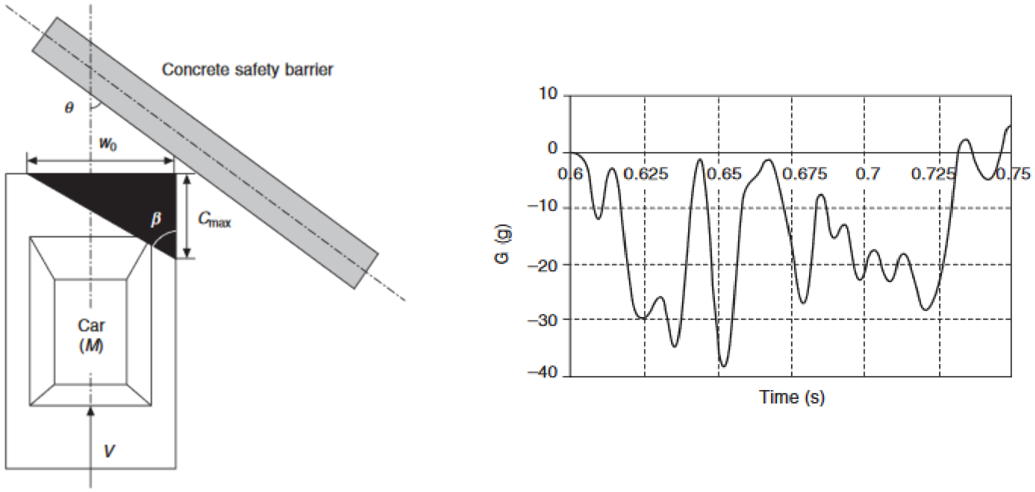

(a) (b)

Figure 2: a) Schematic of vehicular impact with concrete road-side barrier, b) deceleration of the vehicle upon impact with the concrete barrier [25].

Progressive tearing of composite plates was studied experimentally by pulling a metal bolt though a fixated composite plate [28]. Several fiber orientations were experimented on and repeatability and stability varied depending on orientation. Generally, the forces presented were highly stable and repeatable. Additionally, due to the extremely light weight characteristics of the composite plates, the specific energy absorption (*SEA)* values were extremely high. *SEA* is defined as the amount of energy absorbed per unit mass of the energy absorber. An application of this concept was employed in a full-scale cargo-airplane [29, 30], Figure 3 provides a visual illustration of the concept. The floor of the cabin was anchored to the cabin frames utilizing bolts and the progressive tearing concept was implemented in this region. Impact scenarios where the cabin changed in shaped from a circle to oval were recreated and a tensile loading condition was created along the floor of the cabin. High initiation loads were observed, followed by steady loads in the mid region and finally high loads were observed nearing the end of the domain region. This led to lower stability in the overall force-response. Further exploration of this concept and the effects of pin diameter, laminate thickness and stacking patterns was conducted [31]. Small pin diameters and dispersed stacking sequences were observed to produce the highest energy absorption modes. Numerical modelling of this failure mode was conducted by Feser et al. which presented high accuracy to experimental findings [31].

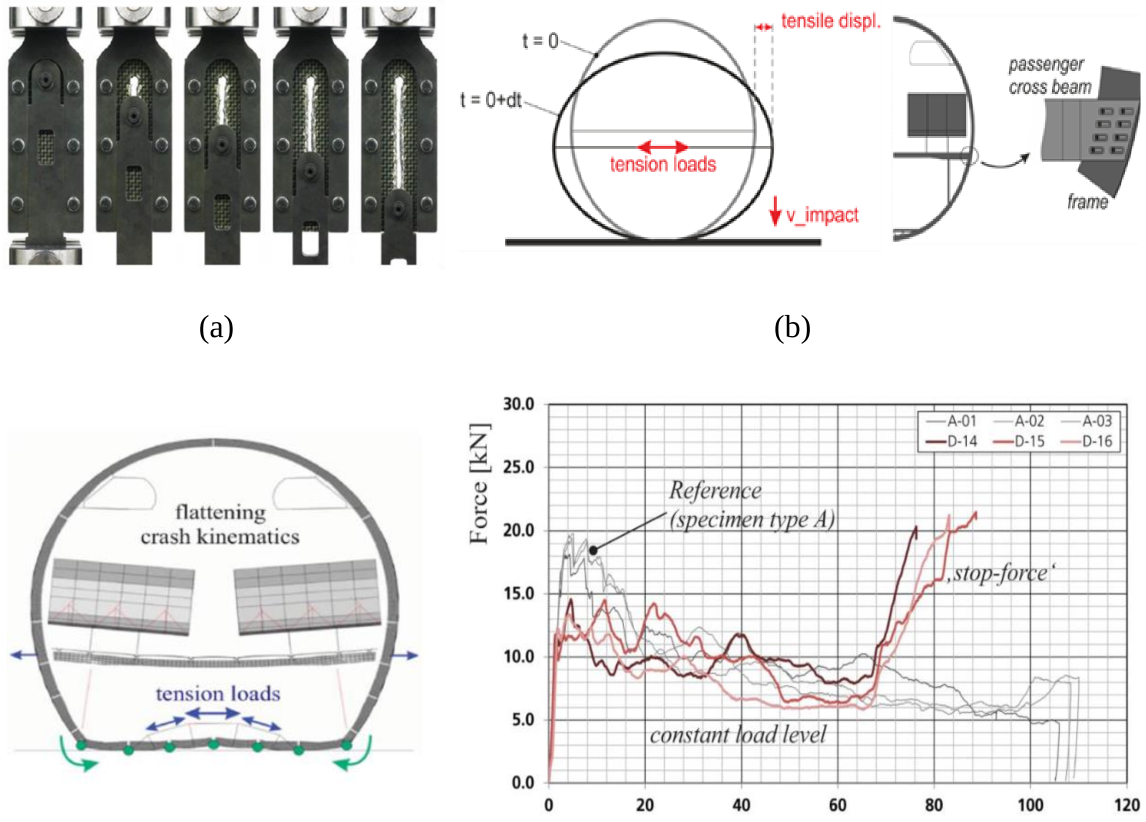

(a) (b)

(c) (d)

Figure 3: a) Apparatus set-up of the progressively torn composite plates [29], b) ‘ovalization’ effect of the cabin frame [30], c) visualization of airplane cabin during impact scenario [30], d) representative force responses of bolt tearing implemented along cabin frame [30].

Additional concepts for a composite tensile energy absorber were explored by Heimbs et. al. in [32]. The concept of bolt pull-out and shearing was considered as an energy absorption method within this study. Quasi-static and dynamic tests were conducted utilizing two carbon fiber reinforced plastic (CFRP) plates held together with a bolt and a locking nut. Two different geometries were explored, and the main purpose of the study was to explore the strain effects of the CFRP plates. The general force response for this deformation mode exhibited a steady increase in force until the peak, followed by a steady drop back to zero after failure due to pin pullout. The experimental set-up and force responses are illustrated in Figure 4. Several composite specimens were tested within this study and the repeatability between the test categories was high. Additionally, similar methods of pull out failure were observed between tests. No visible or macroscopic differences between the dynamic and quasi-static tests were noticed and this led to the conclusion that the CFRP plates presented strain-rate insensitivity. Peak forces as high as 14 kN were recorded. Detailed FE modelling of this deformation mode was completed by Stocchi et al. in [33]. The FE model predictions were shown to have good accuracy and correlation to experimental results. Critical locations were easily identifiable in the FE model. Deformation modes within the CFRP plates were identified with very good accuracy. Experimental testing and numerical modelling of hybrid double-lapped aluminum glass fiber reinforced plastic (GFRP) joints were explored [34] in a similar method as the CFRP joints in [32]. The performance of the GFRP joints was evaluated in tandem to the GFRP reinforced with aluminum to observe the differences in force responses. The aluminum reinforced joints presented far higher force responses with peak forces increasing from 4 to 6 kN to up to 12 kN. Numerical analysis of this deformation mode exhibited that the inclusion of the aluminum reinforcement assisted with a reduction in shear forces at the bolt interface by a factor of 2.

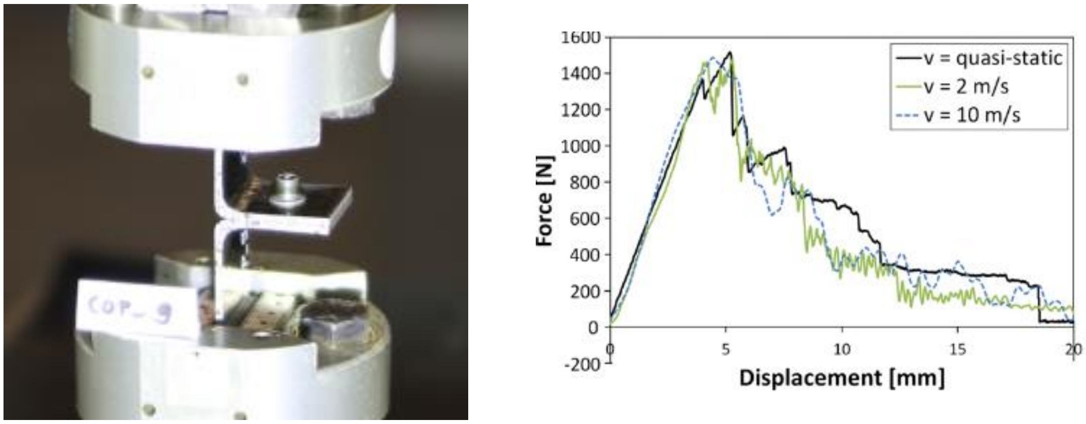

(a) (b)

Figure 4: Test set-up for composite pin pull out experiment, b) force-response from this mode of deformation [32].

Axial splitting of aluminum and steel extrusions is a novel deformation mode initially studied by Reddy and Reid [35]. The scope of this research included experimentation in both quasi-static and dynamic loading conditions. Impact was carried out in both normal and oblique loading configurations. The extrusions were fitted onto a die containing notches. The pressure created from the notches along the extrusions surface propagated a split within the extrusions. The split petals then moved along the profile of the die, causing the petals to curl. Lubrication between the die and the extrusion caused a change in peak force levels. An angled wedge was implemented underneath the die and the impact tests conducted in this configuration exhibited a combination of deformation modes, in addition to the already present splitting mode. The difference in performance between the materials utilized exhibited that the strain rate effects were far more evident in the steel extrusions in comparison to the aluminum ones, in both test conditions and loading conditions. The strain hardening within the steel extrusions amplified the recorded force by a factor of approximately 2. In all these loading cases, a relatively steady and repeatable force response was observed. Representative force responses and a post-test extrusion are illustrated in Figure 5.

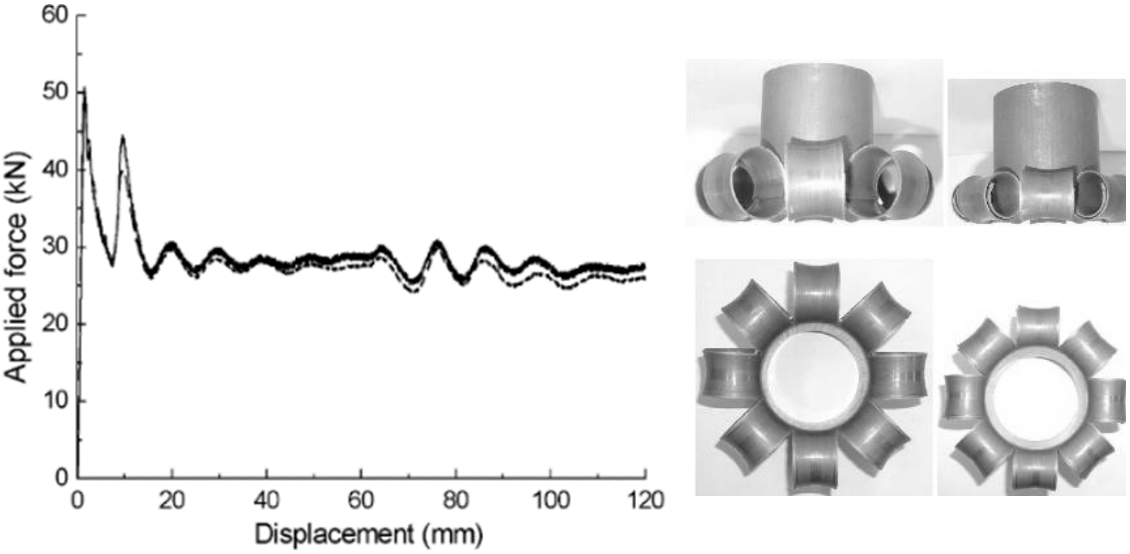

(a) (b)

Figure 5: a) Force response of axial splitting experiments, b) axially split specimens post-test [36].

This deformation mode was exploited in a tensile loading application by Lianpeng et al. [37]. Splitting tests were completed in both quasi-static and dynamic loading conditions. The apparatus designed and utilized within this study recreated conditions of the failure of an anchor hoisting mechanism. An anti-friction gasket was affixed as a plug to the top of an extrusion, a threaded rod was attached to the gasket utilizing a nut. A die was implemented near the end of the extrusion which was not plugged and the initiation of contact between the extrusion and the die initiated a splitting process. The material utilized within this study was Q235 steel. The experiments were conducted under quasi-static, dynamic, normal and oblique/eccentric loading conditions. The resulting forces were extremely high and relatively stable. A graphic of the energy absorber and the force responses are shown in Figure 6.

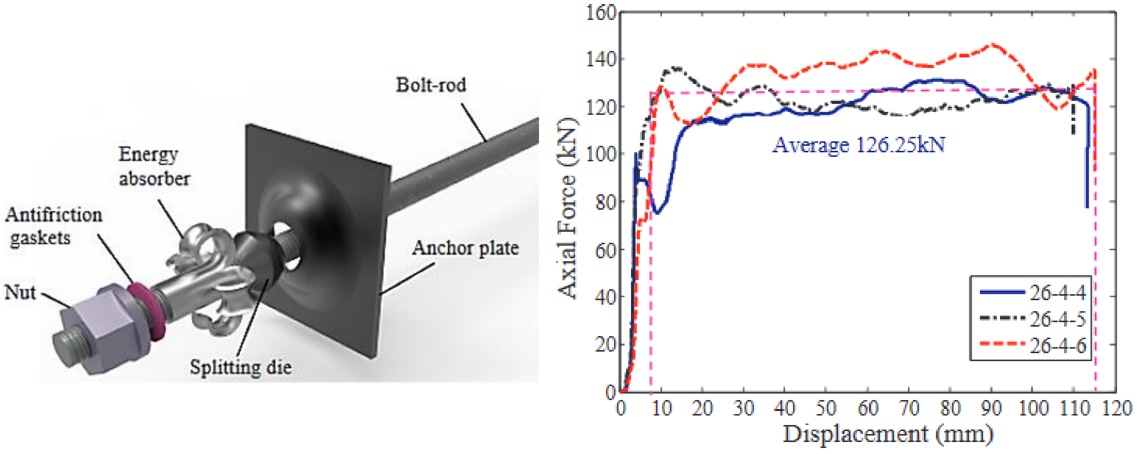

(a) (b)

Figure 6: a) Schematic of anchor arresting mechanism, b) experimental force responses of energy absorber implemented in this configuration [37].

Lianpeng et al. [38] completed an additional study further exploring this deformation mode and implementing modifications to the energy absorber, however this study was completed under compression. Experimental results between similar test conditions within the specimens studied in [37] and [38] produced force-displacement responses and energy absorption values that were comparable with each other, with respect to mean forces and total energy absorption values. These modifications included the influence of utilizing different materials, diameter to thickness ratios, split inducing dies and anti-curling measures. Similar to the previous study, Q235 steel was employed as the material for the extrusion. It was determined that optimal conditions for the extrusion included four pre-cut slits, with free flowing, unrestricted curling. Testing of these extrusions was conducted under normal, 5°, 10° and 15° oblique test configurations. The repeatability between tests was consistent and the oblique loading conditions presented slightly higher forces. Figure 7 illustrates an extrusion in oblique loading conditions, followed by the force responses for extrusions at 5°, 10° and 15° loading configurations.

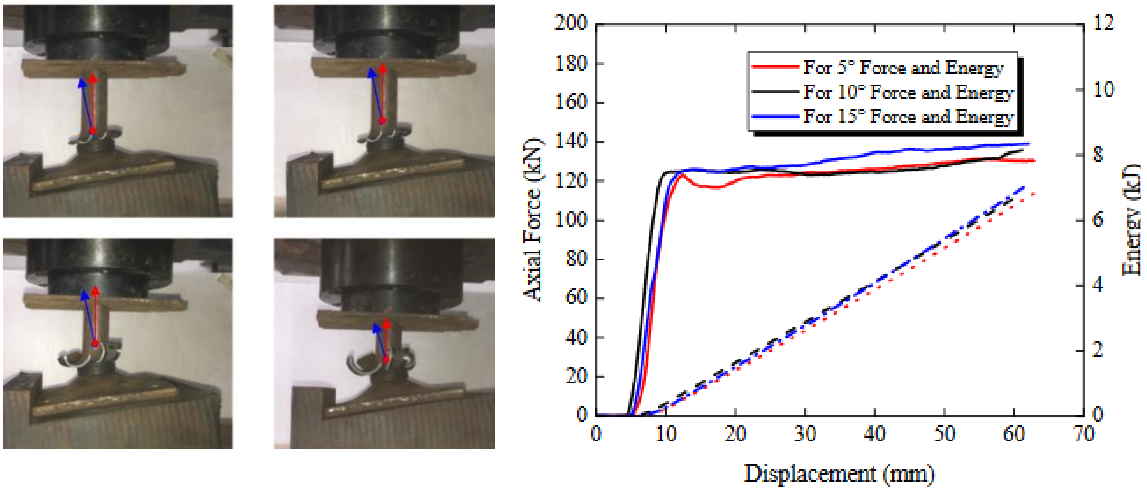

(a) (b)

Figure 7: a) Oblique loading test configuration, b) representative experimental force responses [38].

Tube inversion is a deformation mode which as its name implies is the inversion of the tube through a curling process, utilizing a die and restricting the deformation of the petals, it introduced in [39]. This study pursued an experimental and theoretical approach to tube inversion, investigating the force responses, energy absorption capabilities and effect of die angle. A theoretical analysis of the inversion of a thin-walled metal extrusion was completed by Chirwa [40]. A refined analytical approach was explored by [41]. Modifications were added to previously existing models and these refinements assisted in an increased accuracy regarding the experimental results. Force responses were observed to be repeatable and deformation was noted to be stable. Representative force responses are illustrated in Figure 8.

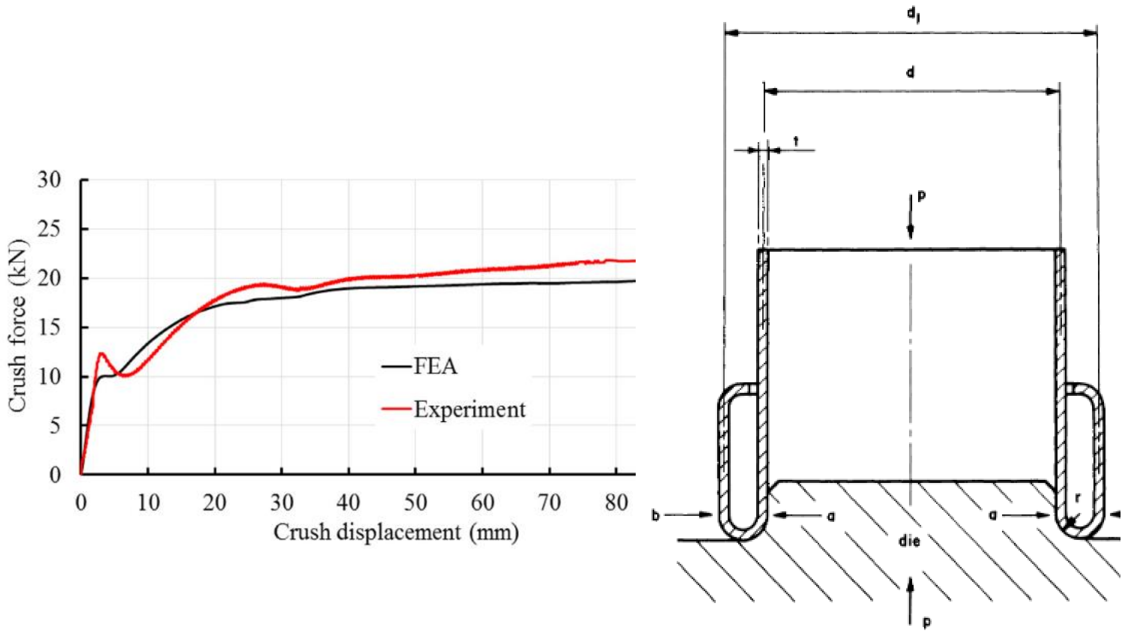

(a) (b)

Figure 8: a) Schematic of tube inversion, coupled with experimental force responses, b) schematic of inverted tube [39].

Axial cutting is a novel energy absorption system developed by researchers at the University of Windsor. It was developed as an alternative to progressive folding, which is the current state-of-the-art in terms of energy absorption in impact scenarios. Axial cutting is a deformation mode which utilizes lightweight AA6061-T6 and T4 extrusions under a consistent deformation mode [42, 43]. As mentioned, axial cutting provides a consistent mode of deformation utilizing multiple custom built cutting tools, fabricated from AISI 4140 steel, a low-alloy steel, having undergone a two stage heat-treatment process to increase durability. In compression tests, the points of pressure between the tip of a cutting tool and the free surface of the extrusion caused plastic deformation of the aluminum extrusion. The result of this is that the force responses produced by the axial cutting deformation mode exhibit high stability and steadiness. The crush force efficiency (*CFE)* produced is very high, with best case scenarios providing values as high as 95%. This presents large improvements in comparison to progressive folding, since progressive folding is plagued by highly fluctuating loads, erratic force responses and low CFE's.

Experimental analyses of axial cutting were conducted with many variations in the number of cutting blades within the cutting device, loading rates and extrusion geometries [9, 44, 45]. The quasi-static experiments were conducted utilizing an MTS machine. The cutter was fastened to a wedge fabricated from the same material as the cutter and placed on top of the extrusion. A strain-gauge based load cell was implemented on the bottom plate of the MTS machine and the extrusion was placed on top of the load cell. The bottom plate of the MTS machine translated upwards and upon reaching the stationary top plate, cutting was initiated. Dynamic tests were conducted utilizing a drop tower and a pneumatic gun. In both cases, a load cell was positioned behind the cutter set-up and securely bolted to the impacting surface to prevent discrepancies due to insecure attachment. The results of these studies exhibit the capability of axial cutting to exceed progressive folding in certain cases [5]. Figure 9 provides a schematic for the quasi-static axial cutting tests.

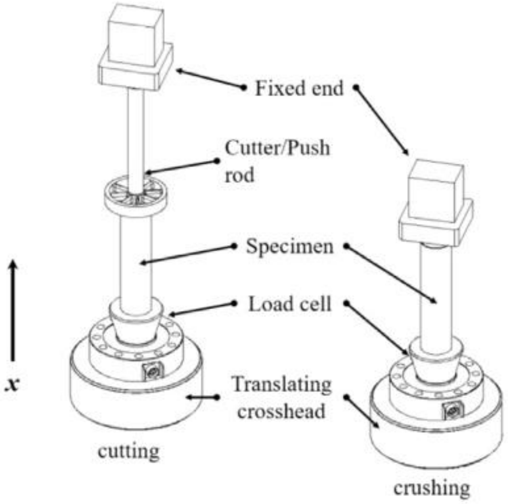

Figure 9: Schematic of the experimental test set-up for the compressive axial cutting experiments, with the specified direction of translation [5].

Passively adaptive energy absorbers were developed exploiting cutting deformation with the ability to change their force response along the axial length of the extrusion. This application of the axial cutting deformation mode provides an advantage that is not presented in progressively folded energy absorbers. Passive adaptivity allows for a user or designer to create unique, tailored force responses based on varying the extrusion thickness at different locations along the length of the extrusion. This is especially useful in applications where a slow ramp in acceleration and consequently the resistance force is required at the initiation of an impact event; due to minimization of impact to an occupant, but a larger energy absorption (force absorbed) capability is necessary at a later point in the deformation regime. This process, which would likely require multiple energy absorption devices with the current state-of-the-art, can be accomplished with one properly sized and designed extrusion utilizing axial cutting. This passive adaptivity was experimentally studied in [46] where extrusions were tested quasi-statically, on a Tinius

Olsen compression testing machine and dynamically, on a drop tower with a pneumatic accelerator. Furthermore, tests were conducted under different loading rates using extrusions machined to identical geometries. Figure 10 provides an example of a passively adaptive geometry with its corresponding force/displacement response under quasi-static and dynamic loading conditions. It can be noticed that the force responses are nearly identical and present no strain-rate sensitivity effects. Additionally, observations can be made through the highlighted regions in Figure 10 (a) and (b) that the corresponding thickness regions perfectly coincide with the force responses, highlighted similarly.

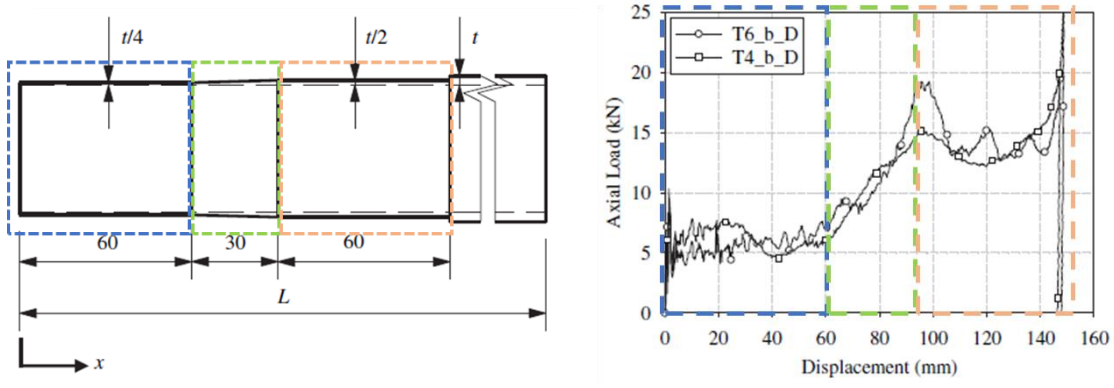

(a) (b)

Figure 10: (a) Schematic of passively adaptive geometry, (b) corresponding force response for specified geometry [46].

Analytical models were created to predict the force responses produced by this cutting mode of deformation. Analytical models developed within this study were based on prior empirical studies exploring steady state cutting of a flat plate with a wedged cutter with wedge angles of 10° and 20° [47]. The effect of wedge length was explored in [48, 49] and it was concluded that a fully wedged cutter with no transition to a flat shoulder led to a continuous increase in force. Three distinct cutting modes were identified by [50] through a culmination of experimental studies including clean and stable cutting, unsteady braided cutting and concertina tearing, the latter two producing far more unsteady force responses. Figure 11 exhibits characteristic force responses for braided cutting [51, 52], concertina tearing [53] and stable cutting, respectively.

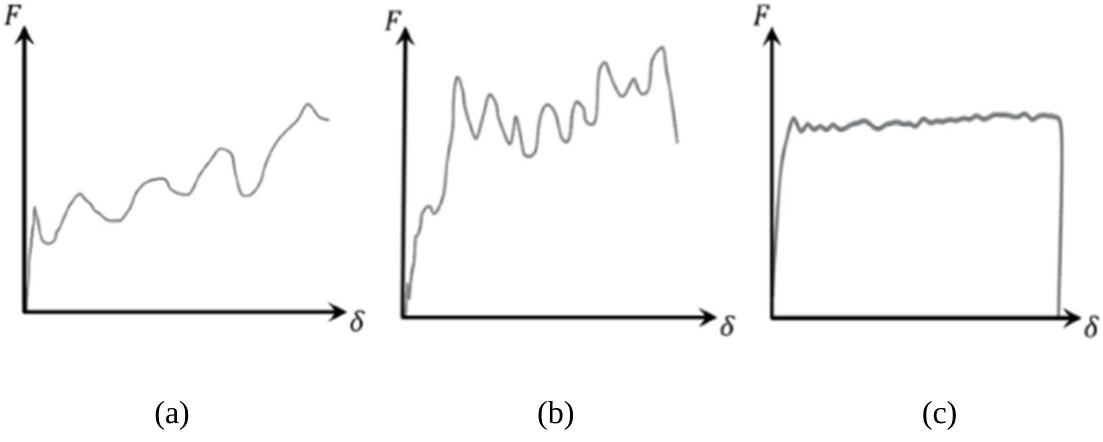

(a) (b) (c)

Figure 11: Representative force-displacement responses for (a) braided cutting, (b) concertina tearing and (c) stable cutting [54].

The first fully functional analytical model capturing the deformation modes as well as the force responses was implemented by Simonsen and Wierzbicki [50]. An Eulerian motion description was employed to fully explore the cutting phenomenon, such that the influx of material into a stationary cutter blade occurred. This model also utilized the principle of virtual power. The crucial modes of deformation and energy absorption produced within a cutting situation were derived from these models and are listed as follows: bending/membrane deformation, crack tip propagation and frictional contributions. The fundamental approach employed by this study was implemented towards developing an analytical model for axial cutting by Jin and Altenhof [42]. This model was developed for low-speed and quasi-static impact scenarios and presented good accuracy within this scope.

The inclusion of a higher number of cutter blades and dynamic loading conditions caused deviations in the predictions and further modifications were implemented by Magliaro et al [5] leading to a considerable increase in prediction accuracy. However, this model still presented some shortcomings in predictions of the clamping effects visible in the cutting deformation mode. Magliaro et al. rectified this by developing a model to analyze the effects and contributions of the hybrid cutting/clamping deformation mode [6]. Investigations were also conducted on the cutting of magnesium extrusions. The key difference noted in the cutting of magnesium tubes was the occurrence of fracture, which was not observed within the aluminum extrusions. As a result, the analytical models were revised to include the strain energy release rate within the magnesium extrusions [55]. It was observed by Simonsen and Wierzbicki [50] that for materials with sufficient ductility such as steel, this term could be omitted, and this was concluded to be the case for aluminum in a later study by Jin [42].

Several investigations have been undertaken to accurately model the cutting of metals. Early attempts modelling orthogonal cutting range from utilization of conventional and familiar Lagrangian elements with failure algorithms to meshless element formulations such as Element-Free-Galerkin (EFG) [56] and Arbitrary Lagrangian-Eulerian (ALE) [7] which do not utilize failure algorithms. It was noted that in the Lagrangian simulations that prediction capabilities presented good accuracy until the onset of fracture, after which the force predictions varied erratically from experimental observations. This problem was far less prevalent in meshless methods such as EFG and ALE based simulations and prediction capabilities were far more accurate and consistent. As the mesh free approach for numerically modelling orthogonal cutting seemed to provide more favourable results, an

Eulerian element formulation was utilized to predict the performance of axial cutting. Majumder et al. developed numerical models utilizing the non-linear FEA solver LS-DYNA®. Model prediction capabilities presented high accuracy in terms of force responses and deformation modes. This approach has been exploited over time in multiple test conditions considering axial cutting [8] with similar accuracy. Figure 12 illustrates both these capacities.

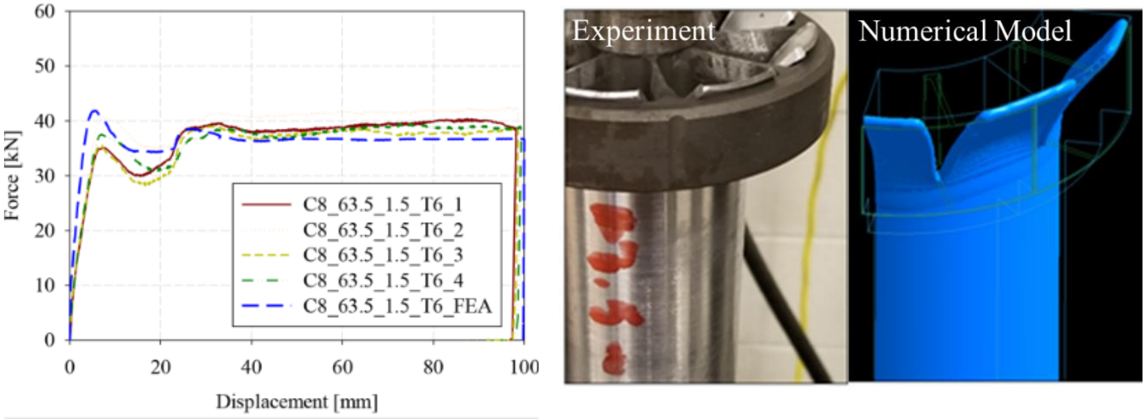

(a) (b)

Figure 12: a) Comparison of experimental force responses against numerical model predictions, b) deformation modes of extrusion predicted by Eulerian numerical model [57].

Impact situations which rely on tensile energy absorption have varying applications. The number of energy absorbers currently available for these applications is scarce in comparison to energy absorbers for compressive applications. Furthermore, a number of these traditional tensile energy absorbers contain disadvantages ranging from erratic force-displacement responses with large fluctuations in force, to inconsistent behaviour through repeated tests. These characteristics result in a certain degree of unpredictability in their performance. In applications where the performance of an energy absorber directly impacts the well-being of the occupant, such as P.F.A.S. and road-side safety barriers [13]- [27], the mitigation of these factors is crucial. Research endeavors undertaken to address these issues can be found within the literature. Progressive tearing of composite plates provides highly stable steady-state forces, however, extremely high forces in excess of the steady state force are present within the initial and termination regions of the domain of displacement [28]- [32]. Tube splitting was completed utilizing Q235 steel and utilized within an anchor arresting mechanism tested under oblique, compressive loadings [33]- [38]. The force-displacement responses within both scenarios were nearly identical under similar loading conditions, exhibiting high repeatability. Tube inversion also presented stable force-displacement responses through the entire domain of displacement, with the main drawback being that inversion works best with lower wall thickness tubes/extrusions, limiting the overall force which can be attained [39]- [41]. Axial cutting [42]- [45] is a method of energy absorption which utilizes a cutting device to penetrate through hollow aluminum extrusions providing highly steady force-displacement responses, with high repeatability and consistency. Quasi-static and high-rate experiments have been conducted and the influence of the number of blades within a cutting device and extrusion geometry have been investigated. In addition, reliable analytical [47]- [55] and numerical modelling [7, 8] schemes are available for this mode of deformation which predict force-displacement responses and deformation features with high accuracy. Axial cutting presents advantages such as steady force-displacement responses, high repeatability and predictability which are currently unavailable in currently existing tensile energy absorbers. Furthermore, cutting has been studied extensively under compressive loading conditions, with no studies exploring its capabilities in tensile energy dissipation.

Chapter 2: Analytical Modelling

2.1: Model Overview

The analytical model is explained in [42], so readers are encouraged to explore this study to learn about the derivation process for the analytical modelling procedures. Passive adaptivity are also analytically modelled within [58], whose unique force-displacement responses were presented within the literature review. The complete analytical model was exploited within this study to design theoretical force responses for passively adaptive extrusions. These theoretical responses were utilized to reverse engineer and design test extrusions. The modelling procedures for the complete force-displacement response, presented within the sub-sections below were developed by Mr. John Magliaro and the text provided within this section consequently summarizes his work. The models developed were exploited within this study and likewise, the conceptual force responses presented were completed in close collaboration with Mr. John Magliaro.

2.2: Steady State Cutting Force

The analytical modelling procedure for large deformation problems such as cutting involves the classification of deformation modes present within the problem, utilizing of principles such as virtual power. This approach is explained in further detail within [54] where a robust explanation for the assumptions and considerations made are listed. Equation (1) provides the expression utilized to determine the analytical mean force during an "*n*-bladed" cutting experiment. The first bracketed term multiplied by the term, *n* (defining the number of blades within the cutter), defines the combination of the resistance force contributed by each deformation mode and frictional contribution from contact. The frictional coefficient utilized within this analytical model was 0.3, which was determined upon from a number of reasons. Firstly, this value had been utilized in previous analytical modelling attempts highlighted within [42, 58] and had provided a high validation metric in comparison to experimental results. Further justification for the use of this value is found within a study conducted to explore the dry sliding between AA6061 and tool steel [59]. The conclusions of this study presented a recommendation that under conditions where severe wear was evident, as is the case with axial cutting, a coefficient of friction of 0.3 should be utilized.

$$F = n\left(1 + \mu \cot\theta \cos\frac{\theta}{2}\right) \cdot \frac{2\sigma_o t}{\sqrt{3}} \begin{bmatrix} \dfrac{t(B + R_r)}{4\sqrt{3}} \cdot \left(\dfrac{1}{R_r \cos\theta} + \dfrac{1}{r_0 + r_m} - \dfrac{1}{r_m + r_i}\right) \\ + B\theta + T + \dfrac{K_\theta R_r}{2} + \dfrac{\pi t r_m}{2nR_a} \end{bmatrix} \tag{1}$$

Each term within the second bracketed expression is associated with a deformation mode present within the cutting phenomenon. Prior to the explanation of these modes, the rolling radius needs to be defined. The rolling radius, R_r, defines the amount of curvature present at the interface of the extrusion and the side of the cutter. This term is essential for the calculation of several other terms as presented within Equation (1). The rolling radius is computed through the utilization of Equation (2), derived in [58].

$$R_r = \left[\left(\frac{Bt}{4\sqrt{3}K_\theta \cos\theta} - \frac{T^2}{2}\right) + \sqrt{\left(\frac{T^2}{2} - \frac{Bt}{4\sqrt{3}K_\theta \cos\theta}\right)^2 + \frac{T^2}{K_\theta}\left(\frac{Bt}{2\sqrt{3}\cos\theta} + \pi t r_m \tan^2\theta\right)}\,\right]^{1/2} \tag{2}$$

The terms defined within this paragraph are all utilized within Equation (3). This equation is eventually used within Equation (1) to determine the steady state force. The term K_θ, defines the membrane stretching coefficient, which is quantified through Equation (3). The radial increment, Δr, is computed through Equation (4). The deformed shoulder length,

D_{ss},, is computed through Equation (5) The term R_a, defining the axial bend radius, is defined through Equation (6).

$$K_\theta = 0.366(1 + 0.55\theta^2) \cdot \cos^2\theta \tag{3}$$

$$\Delta r = \frac{nB}{\pi} \tag{4}$$

$$D_{ss} = \left(R_r + \frac{1}{2}T\right)\cot\theta + l_b \tag{5}$$

$$R_a = \frac{D_{ss}^2}{\Delta r} + \frac{\Delta r}{2} \tag{6}$$

The deformation modes presented within the second bracketed term will be explained in this paragraph, Figure 13 (a) and (b) provides visual illustrations of these deformation modes. Moving from left to right within the second bracketed expression, the first term refers to the far-field bending effect, it is highlighted in green. The far-field bending occurs when the extrusion has successfully cleared the wedged portion of the cutter blade and is within the steady state, flat region of the blade, called the ‘stable flap’. This is followed by the transient membrane deformation, highlighted brown, which occurs along the wedged portion of the cutter blade where the force is steadily developing, it is referred to as the ‘transient flap’. The continuous chip formation zone is an area directly in the vicinity of the contact region between the cutter tip and the extrusion, illustrated in red, where metal chips form due to this interaction. The extrusion material stretches circumferentially ahead of the cutter tip due to the pressure exerted by the blunt cutter tip against the extrusion, shown in gray, is expressed within the fourth term of this expression. Finally, the formation of the petalled sidewalls is captured within the last term and is shown in Figure 13 (b). The petalled sidewalls occur due to the clearing of the petals from the cutter’s blades. The free petals curl with a certain curvature, further contributing to the force response.

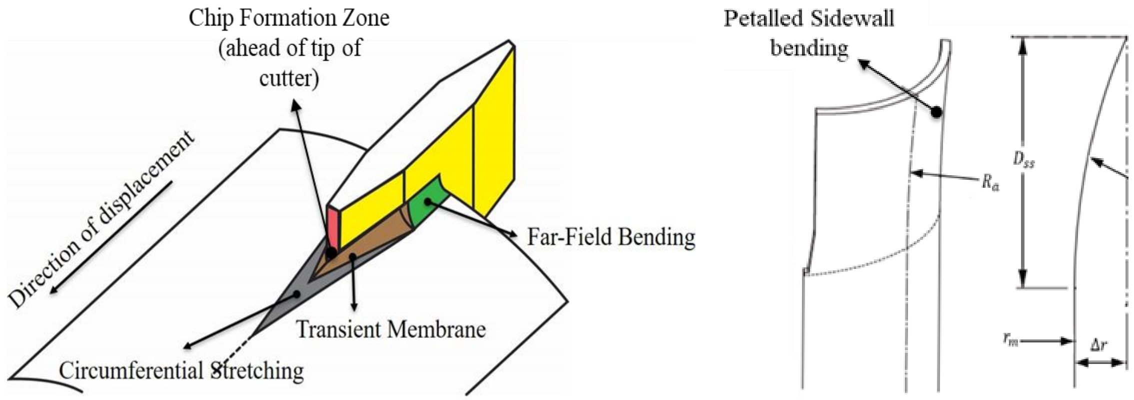

(a) (b)

Figure 13: Schematics (a) deformation modes for an extrusion subject to axial cutting, (b) petalled sidewalls forming upon exiting cutter [42, 5].

2.3: Complete force-displacement response modeling

The steady state force response, while providing the force response for the majority of the test, does not paint the complete picture in terms of the overall force-displacement response. To fully capture this, the onset of the force response until the steady state region and for passive adaptivity were modelling separately, and they are outlined within the following sub-sections.

2.3.1: Transient loading

The beginning of the force response is captured through an elastic indentation force caused by the penetration of the wedge. There is a small amount of highly localized plasticity at the onset of the contact. However, elasticity is the dominant factor within this region. This is followed by an increase in load to the steady state force. The generalized derivation for the elastic indentation force is presented in Equation (7). This derivation was presented in

[58] and was derived through consideration of the pressure of the wedge on the unblemished extrusion.

$$F_e = n\sum_{i=1}^{N}\sigma_i \cdot A_{c_i} = \frac{nE}{L}x \cdot \sum_{i=1}^{N} A_{c_i} \tag{7}$$

The term A_{c_i} was utilized to define the contact area between the blunt edge of the cutter and the extrusion. An illustration of this contact area is exhibited in Figure 14. Two expressions are presented in Equation (8). The first expression represents the contact area at the blunt interface of the cutter. The second expression represents the contact area past the blunt tip of the cutter blade. The rolling radius past the blunt blade tip was defined as $R_r \cos\theta$ [42].

$$\begin{cases} A_{c_{tip}} = T(2R_r\cos\theta + t) \\ A_{c_{circ}} = 2(2R_r\cos\theta + t)\cdot x, 0 \le x \le \delta_Y \end{cases} \tag{8}$$

The elastic indentation zone of deformation persists up until a certain penetration depth, which will be labelled, δ_Y. Beyond this depth, the material yields, and this zone will be referred to as the post-yield deformation area. This penetration depth is defined in Equation (9). This expression was validated for extrusions equal to or below 300 mm in axial length [58].

$$\delta_Y = L \cdot \frac{\sigma_o}{E} \tag{9}$$

Through substitution of the expressions derived in Equation (8) and Equation (9) into Equation (7), an expression can be derived for the instantaneous elastic indentation force between the bounds of 0 mm of penetration to δ_Y. Substitution δ_Y into Equation (10) provides the expression for the maximum elastic indentation force and this can be found in Equation (12).

$$F_e(x) = \frac{nE(2R_r\cos\theta + t)}{L} \cdot (2x\tan\theta + T)x, 0 \leq x \leq \delta_Y \tag{11}$$

$$F_E = n\sigma_o(2R_r\cos\theta + t)(2L\tan\theta + T) \tag{12}$$

The loading region following the elastic indentation is identified as the post-yield region. As the name suggests, the extrusion material has yielded to the pressure applied onto the extrusion surface by the cutter blade. This force is identified as F_{PY}, within this study. Carrying on from the last term, this post-yield region exists for a displacement domain starting at the penetration depth δ_Y until the blade wedge length, l_b [58]. Past this point, the force was considered to be fully developed and steady state, the expression presented in Equation (1) prior within this section was utilized to calculate the force within this region.

$$F_{PY} = \frac{F_Y - F}{(\delta_Y - l_b)^2} \cdot [x^2 - 2l_bx + l_b^2] + F \tag{13}$$

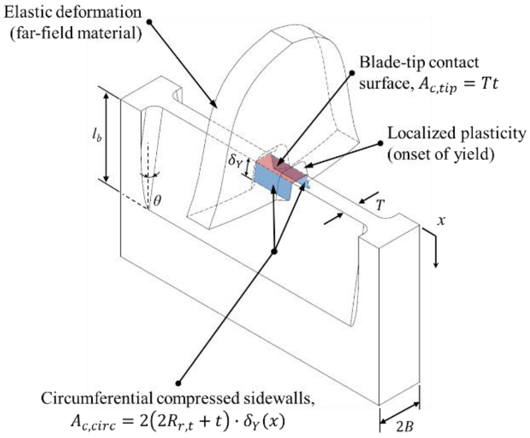

Figure 14: Schematic of an elastically indented extrusion with highlighted contact regions.

2.3.2: Variable thickness considerations for passive adaptivity

One unique feature of axial cutting that it offers a high degree of controllability in terms of force/displacement response. This was established with the creation of passively adaptive extrusions. These extrusions consisted of wall thicknesses which varied along their axial length [46]. This allowed for the creation of highly unique, sophisticated and highly repeatable force responses, not replicable by other energy absorbers. The force responses for these passively adaptive geometries were analytically modelling through the utilization of step functions which accounted for the change in wall thickness along the axial length. Additionally, the force/displacement response was modified to act as a function of the axial position, x, in addition to the wall thickness, t [58], as shown in Equation (14).

$$F = f\{t(x)\} \tag{14}$$

A combination of the approaches explained earlier within this sub-section was utilized to fully model the development of the force response from its initiation to its steady state behavior. As mentioned prior, a piecewise function approach was implemented to accurately model extrusion wall thickness changes. One new issue which was encountered was that the regions where the wall thickness change occurred had to be modelled. The transition between two stepped thickness regions does not equate to a stepped change in the force response. Due to the wedged shoulder of the cutter blade, a transitional zone, where the force developed to steady state between two thickness regions, lasting the length of the cutter wedge was implemented. An illustration of this modelling issue is shown in Figure 15.

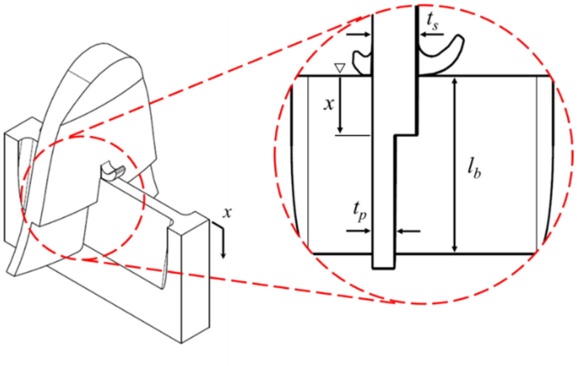

Figure 15: Visualization of an extrusion with a modified for passive adaptivity containing sudden, stepped transitions in the wall thickness [58].

$$t_T = \frac{t_s - t_p}{l_b} \cdot (x - \delta_T) + t_p \qquad (15)$$

An artificially transitioning wall thickness was implemented to accommodate for the development of the force response in this region. t_T and t_V were terms coined artificially introduce the transitions within the stepped wall thickness changes. Within Equation (15), the terms ts and tp represent the secondary and primary thicknesses in the stepped regions, respectively. The term δ_T represents the displacement where this junction or interface between the two wall thickness regions.

The expression presented in Equation (16) accommodates for the force response of the linearly varied thickness region. The term δ_v, signifies the displacement along which this linear transition occurs. The term L_v, represents the total length of the transitional zone.

$$t_V = \frac{t_p - t_s}{L_V} \cdot (x - \delta_V) + t_s \qquad (16)$$

2.4: Passive adaptive geometry design

Utilizing a combination of these analytical modelling approaches, three designs for passively adaptive extrusions were created. The impetus behind their creation was to illustrate the ability to utilize the analytical model as a high accuracy design tool. Within this study, three passively adaptive extrusion designs labelled; PA1, PA2 and PA3 were conceptualized and are shown in Figure 16. PA1 and PA3 were created with three force regimes; PA1 consisted of a high, medium and low force region, and PA3 consisted of a high, medium and high force region, respectively. PA2 was similar to PA1 in the sense that it followed a similar force region trend, the main difference was that a linearly varying force region was included in between the medium and low force region. Sample force displacement responses compiled from the analytical model and PA1, PA2 and PA3 are presented in Figure 17 (a), (b) and (c), respectively. Table 1, Table 2 and Table 3 illustrate the locations along the axial length along where the force regions are implemented.

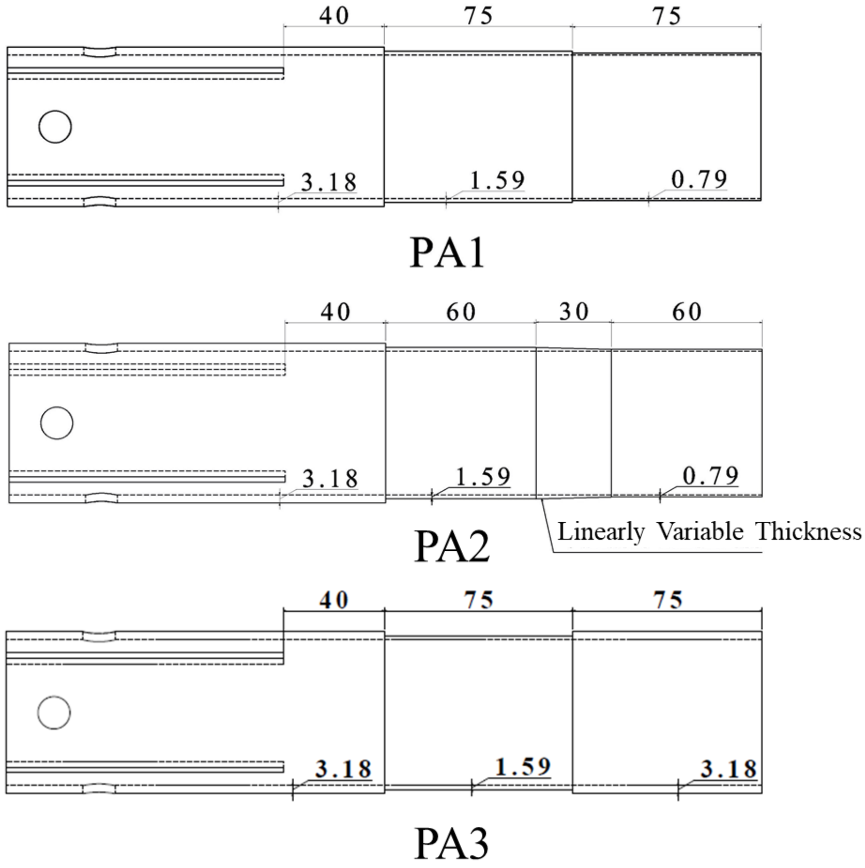

Figure 16: Wall thickness profiles of passively adaptive geometries; all dimensions in ‘mm’.

Additionally, the regions of stepped thickness changes are approximated as the wedge length of 6 mm. Validation of the analytical predictions with the experimental observations is conducted in Chapter 7. Identical configurations were machined into the 63.5 mm and 50.8 mm OD extrusions. The passively adaptive extrusions were machined from extrusions with the higher, 3.175 mm wall thickness.

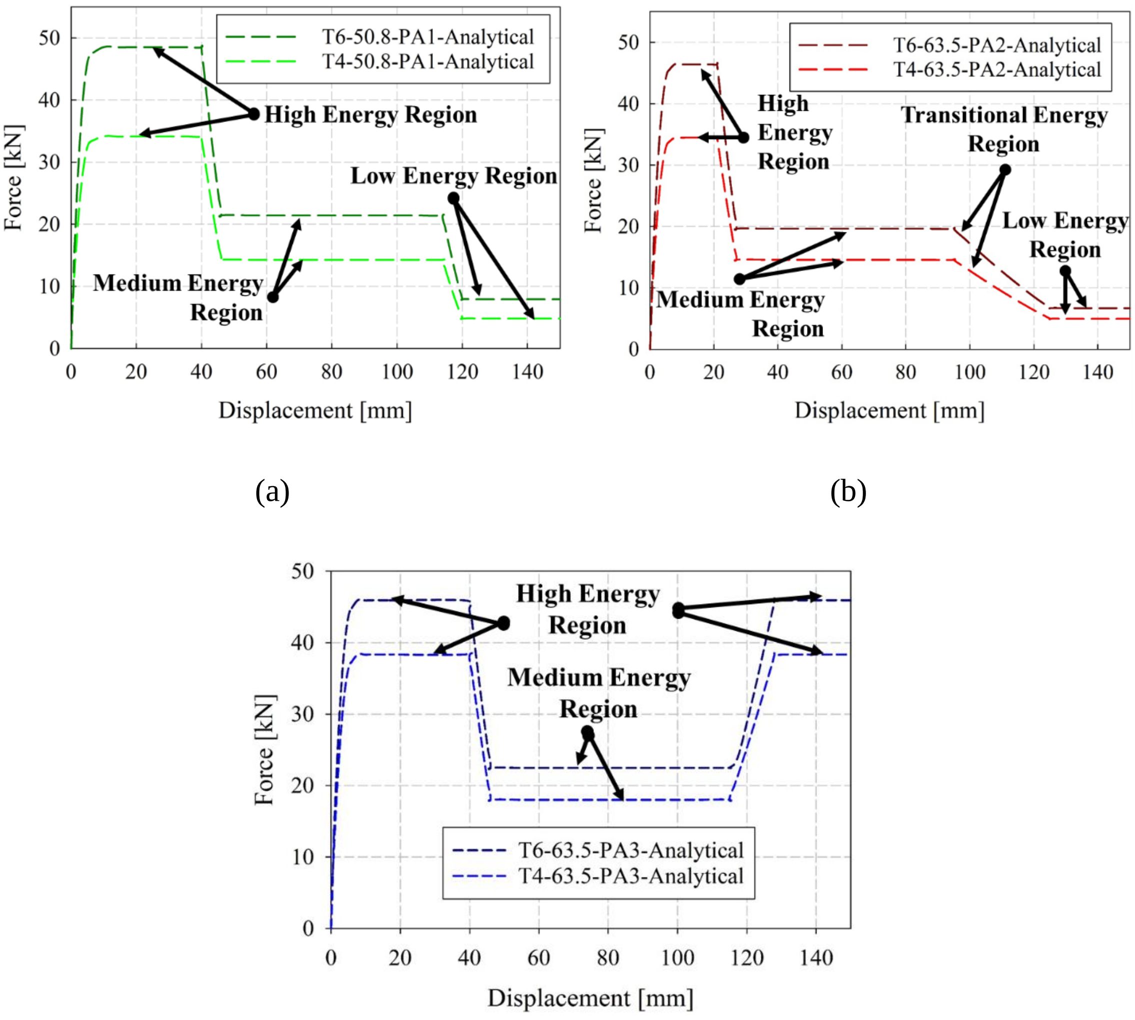

(a)

(b)

(c)

Figure 17: Analytical force responses for (a) PA1, (b) PA2 and (c) PA3 extrusions.

Table 1: Regions of the wall thickness profile necessary to replicate passive geometry PA1.

Adaptive region	Domain [mm]			Thickness $[t(x) =]$	Force $[F\{t(x)\} =]$
Linear-elastic phase	0.0	$\leq x <$	0.8	t_w	F_e, Eq. (11)
Post-yield phase	1.2	$\leq x <$	6.0	t_w	F_{PY},Eq. (14)
High energy region	6.0	$\leq x <$	40.0	t_w	F, Eq. (1)
Transitional phase*	40.0	$\leq x <$	46.0	$-\frac{t_w}{12} \cdot (x - 40) + t_w$	F, Eq. (15)
Medium energy region	46.0	$\leq x <$	115.0	$0.50t_w$	F, Eq. (1)
Transitional phase*	115.0	$\leq x <$	121.0	$-\frac{t_w}{24} \cdot (x - 115) + 0.50t_w$	F, Eq. (15)
Low energy region		$x \geq$	121.0	$0.25t_w$	F, Eq. (1)

Note: * True wall thickness was replaced with average wall thickness between the two stepped regions to compute accurate force responses, this was artificially introduced for analytical modelling purposes only and does not occur in the test extrusion of this geometry.

Table 2: Regions of the wall thickness profile necessary to replicate passive geometry PA2.

Adaptive region	Domain [mm]			Thickness [$t(x)$ =]	Force [$F\{t(x)\}$ =]
Linear-elastic phase	0.0	$\leq x <$	0.8	t_w	F_e, Eq. (11)
Post-yield phase	1.2	$\leq x <$	6.0	t_w	F_{PY},Eq. (14)
High energy region	6.0	$\leq x <$	20.0	t_w	F, Eq. (1)
Transitional phase*	20.0	$\leq x <$	26.0	$-\frac{t_w}{12} \cdot (x-20) + 0.50t_w$	F, Eq. (15)
Medium energy region	26.0	$\leq x <$	95.0	$0.50t_w$	F, Eq. (1)
Linearly varied region	95.0	$\leq x <$	125.0	$-\frac{t_w}{120} \cdot (x-95) + 0.50t_w$	F, Eq. (18)
Low energy region		$x \geq$	125.0	$0.25t_w$	F, Eq. (1)

Note: * True wall thickness was replaced with average wall thickness between the two stepped regions to compute accurate force responses, this was artificially introduced for analytical modelling purposes only and does not occur in the test extrusion of this geometry.

Table 3: Regions of the wall thickness profile necessary to replicate passive geometry PA3.

Adaptive region	Domain [mm]			Thickness [$t(x) =$]	Force [$F\{t(x)\} =$]
Linear-elastic phase	0.0	$\leq x <$	0.8	t_w	F_e, Eq. (11)
Post-yield phase	1.2	$\leq x <$	6.0	t_w	F_{PY}, Eq. (14)
High energy region	6.0	$\leq x <$	40.0	t_w	F, Eq. (1)
Transitional phase*	40.0	$\leq x <$	46.0	$-\frac{t_w}{12} \cdot (x - 40) + t_w$	F, Eq. (15)
Medium energy region	46.0	$\leq x <$	115.0	$0.50t_w$	F, Eq. (1)
Transitional phase*	115.0	$\leq x <$	121.0	$\frac{t_w}{24} \cdot (x - 115) + 0.50t_w$	F, Eq. (15)
High energy region		$x \geq$	121.0	t_w	F, Eq. (1)

Note: * True wall thickness was replaced with average wall thickness between the two stepped regions to compute accurate force responses, this was artificially introduced for analytical modelling purposes only and does not occur in the test extrusion of this geometry.

Chapter 3: Experimental Methodology

3.1: Specimen and fixture preparation

Within the scope of the study, energy absorbers were AA6061 extrusions in both T6 and T4 temper conditions. The tubing was received in stock lengths of either 12 ft or 20 ft. This tubing was then saw cut down to approximately 300 mm. The tubing was received in the T6 configuration, and heat treatment was performed to these tubes to achieve the T4 temper, in accordance with the ASTM B918 standard [60]. They were received as continuous entities without any seams or welds. The T4 extrusions presented far higher strain to failure and strain hardening, in comparison to the T6 counterpart. Representative stress-strain responses of the T6 and T4 extrusions are presented in Figure 18.

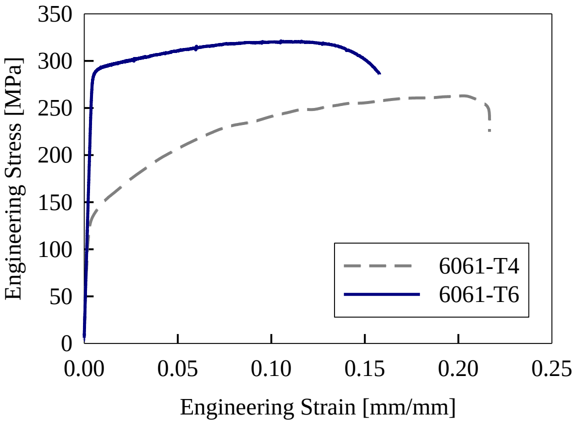

Figure 18: Engineering stress-strain response of extruded AA6061 in T6 and T4 temper conditions [46].

The differences in the mechanical properties between the material in both temper conditions can be related to their microstructures. The distribution and size of the precipitate grains within the material are crucial factors in determining a material's strength [61]. The presence of smaller, more evenly distributed grains through the material matrix prevents the motion of dislocations, thereby increasing the strength of the material. The opposite is true for materials with larger grains, which are less evenly distributed, they provide less resistance to the motion of the dislocations and therefore have lower mechanical properties and higher ductility [62, 63]. In addition, the cooling rate of the material affects the grain size, with higher cooling rates creating smaller, more distributed grains and lower cooling rates forming larger grains. The ASM handbook [64] defines the T6 temper condition as a solution heat treat with artificial aging for materials where mechanical properties have been greatly improved due to precipitation heat treatment. The T4 temper condition is defined as a solution heat treatment with natural aging. This directly correlates with the grain size of the precipitates within the material matrix. Finally, the process of treating the material to a T4 condition involves the removal of stresses that were built up during the extrusion process [63], the removal of these stresses also contributes to the lower strength of the T4 tempered material. Figure 19 illustrates the microstructure of AA6061 in the T6 and T4 tempers, respectively. It can be seen that under the same magnification scale, the T6 material contains much finer, needle shaped grains in contrast to the larger grains found in the T4 material, due to a combination of heat treatment and the slower cooling rate. The presence of the finer, needle shaped grains provides for higher strength characteristics of the T6 temper, compared to the T4 condition.

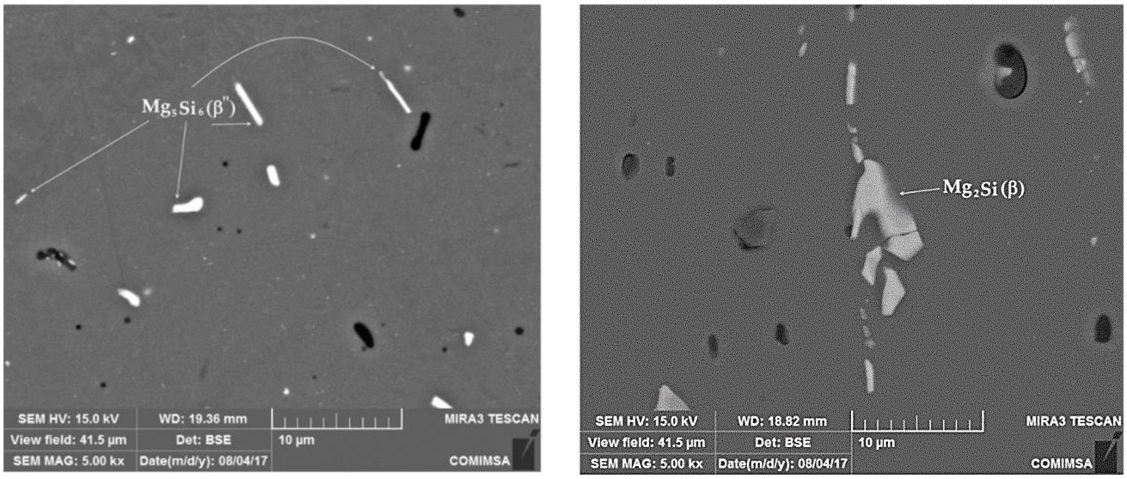

(a) (b)

Figure 19: Microstructure exhibiting grain size in AA6061 (a) T6 and (b) T4 [65].

Two groups of specimens were machined for experimental testing. The first group consisted of straight-sectioned extrusions, with consistent wall thickness along the extrusion length. The second group of extrusions represented passive adaptive energy dissipation structures, whose wall thickness varied along the axial length of the extrusions. The wall thickness profiles for the adaptive extrusions were determined through reverse engineering the force-displacement responses utilizing the analytical model and piecewise functions. The general schematics for the extrusions is presented withing Appendix A.

Table 4 contains the summary of the material properties for extrusions in the specified temper conditions. The flow stress; labelled σ_o, is defined as the average value in the plastic regime of the aluminum extrusions response. Equation (17) provides a mathematical definition for the equivalent flow stress, within the materials response, $\sigma_p(\varepsilon)$.

$$\sigma_o = \frac{1}{\varepsilon_f - \varepsilon_Y} \int_{\varepsilon_Y}^{\varepsilon_f} \sigma_p(\varepsilon) d\varepsilon \tag{17}$$

An alternate approximation for the flow stress was presented in [66]. This expression is presented within Equation (18), and is reliant on the ultimate tensile stress, σ_U. Equation (17) was the expression utilized within this thesis.

$$\sigma_o \approx 0.92\sigma_U \tag{18}$$

Table 4: Mechanical properties of 6061-T4 and 6061-T6 from tensile testing [46].

Properties	AA6061-T4	AA6061-T6
Elastic modulus, E [GPa]	68.1	65.3
Yield strength, σ_Y [MPa]	116.2	277.5
Bulk Modulus, K [GPa]	65.0	68.9
Shear Modulus, G [GPa]	24.5	25.4
Ultimate strength, σ_U [MPa]	258.3	320.2
Flow stress, σ_o [MPa]	187.3	298.7
Density, ρ [kg/m^3]	2730	2730

The extrusions were received in a thick and thin-walled configuration. The thick-walled extrusions possessed a wall thickness of 3.175 mm, whereas the thin-walled extrusions consisted of a wall thickness of 1.588 mm. Two diameters of extrusions were obtained in stock lengths, as specified. These outer diameters were 63.5 mm and 50.8 mm. Initially the materials were saw cut to approximately 300 mm in length, followed by a tempering process, to obtain extrusions of the T4 temper condition. Upon completion, the uneven ends of the extrusions (due to the saw cut) were milled such that they were square to the extrusion centerline, flat, and free of any burrs or imperfections. The remainder of the machining process was completed in two stages. A CNC lathe operated by a professional technician was utilized to turn down the thickness of the extrusions of both the straight-section and passively adaptive extrusions. A polyethene insert was machined for each extrusion wall thickness and diameter such that the insert could be friction fit into the extrusions during this turning process. This was done in order to prevent any deformation or damage to the extrusion during the machining process. This problem was more relevant with the thin-walled extrusions, which were prone to flex under heavy transverse load, potentially occurring during machining.

The second step in this machining process required the utilization of a milling machine. Once again, the polyethylene plugs were inserted into the extrusions to prevent any deformation or flex. A rotary indexing head was utilized to perfectly space holes which would be occupied by steel dowels during experimental testing. A ½-inch drill bit was utilized to create two sets of two holes, which would be utilized to anchor the extrusion during experiments. Each set of holes was spaced 180° apart. The first set of holes were machined at an axial length of were machined at an axial length of 20 mm from the base of the extrusion. The second set were machined at 36 mm along the axial length.

A 1/8-inch end mill bit was utilized to cut slits, each 110 mm long along the axis of the tube. Four identical slots were cut at equivalent 90° spacing circumferentially. Once again, the indexing rotary head was utilized for spacing. These slots were created after the holes to prevent as much flex as possible. The spacing of the slots was chosen such that a four bladed cutting tool could be fit here. The tolerances for all the critical dimensions were ±0.1 mm. The cutting tool utilized within this test configuration was identical to the tool utilized in prior testing [44]. The cutting tool was fabricated with a 4140-tool steel alloy, subject to a two-stage heat treatment process, to strengthen the material further. The outer diameter of the cutting tool was 101.6 mm, and the height of each individual cutter blade was 20 mm. The blades of the cutting tool consisted of a blunt tip with an initial thickness of 1.2 mm, which tapered up to 3 mm, further along the cutter blade. A schematic of the cutting tool and the extrusion can be found in Figure 20.

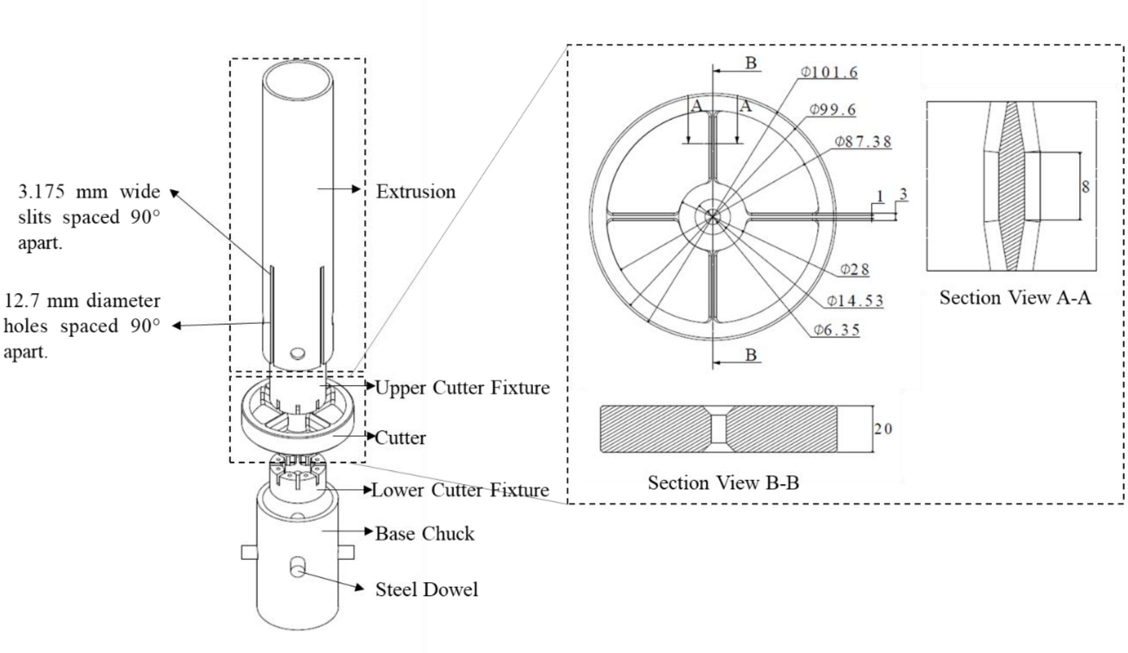

Figure 20: Critical components of the experimental energy absorbing apparatus (straight-sectioned geometry shown).

3.2: Tensile testing apparatus design

The design of the apparatus utilized for the tensile axial cutting tests was designed on CATIA V5. A set of fixtures were created to modify an existing hydraulically powered long stroke tension/compression machine for a tensile axial cutting mode of deformation. This sub-section will discuss the overall fixturing utilized to accommodate for a tensile axial cutting mode of deformation, the design of the cutter fixturing and extrusion/cutter set-up. The overall schematic of the tensile testing apparatus is presented in Figure 21.

As noted, prior, the cutting tool consisted of four cutter blades spaced 90° apart. Each cutter blade had a nominal thickness of 3 mm. The fixturing for the cutter was created as a set, consisting of an upper and lower fixture. These fixtures consisted of cavities which were designed to fit the center hub of the cutting tool and hold the four blades in place to prevent rotation. The cutter fixtures were fabricated from 4140 steel, which had undergone a two-stage heat treatment process. The cavities of the cutter fixtures were identical between the top and bottom fixtures. The cutter fixtures were machined to accommodate for either four or eight-bladed cutting tools. However, only a four bladed cutting tool was utilized within this study. Eight, #6-UNF threaded holes were tapped into the fixtures and a central ¼-UNC threaded hole was tapped into the center of the cutter fixtures. Fasteners were utilized to secure the two fixtures together around the cutter hub. A 1 ¼-inch-UNC threaded hole was tapped into the top of the upper cutter fixture.

A base chuck was utilized to anchor the end of the extrusion which was slotted. The annular base chuck was fabricated from the same material as the cutter fixtures. Four holes corresponding to the holes on the machined end of the extrusion were machined into the base chuck. Steel dowels with a breaking strength of 187 kN were implemented through the extrusion and the base chuck, securing the extrusion in place.

The fixturing utilized to accommodate for a tensile mode of cutting consisted of a combination of hoist rings and connecting links. Hoist rings were utilized within this set-up as they provided high flexibility with their ability to rotate 360° axially, and pivot 180°. This allowed for higher degree of freedom to account for any misalignment within the test set-up. The hoist rings and connecting links had proof loads of 100 kN. Two sets of two hoist rings were utilized to completely set this test fixturing. The first set of hoist rings was located near the top end of the set-up, connecting the upper cutter fixture to the load cell, which was fastened to the hydraulic arm at the very top of the set-up. The lower hoist ring in the upper set of hoist rings was fastened to the upper cutter fixturing through a 1 ¼-inch UNC bolt. The bottom set of hoist rings were fastened to the base chuck and the base plate, to securely anchor the extrusion, while the cutter was displaced upwards through the extrusion. The base plate of the set-up was anchored to the base of the testing machine through four, 1-inch UNC fasteners and nuts. Further schematics for the fixturing described within this section can be found within Appendix B, presented at the end of this document.

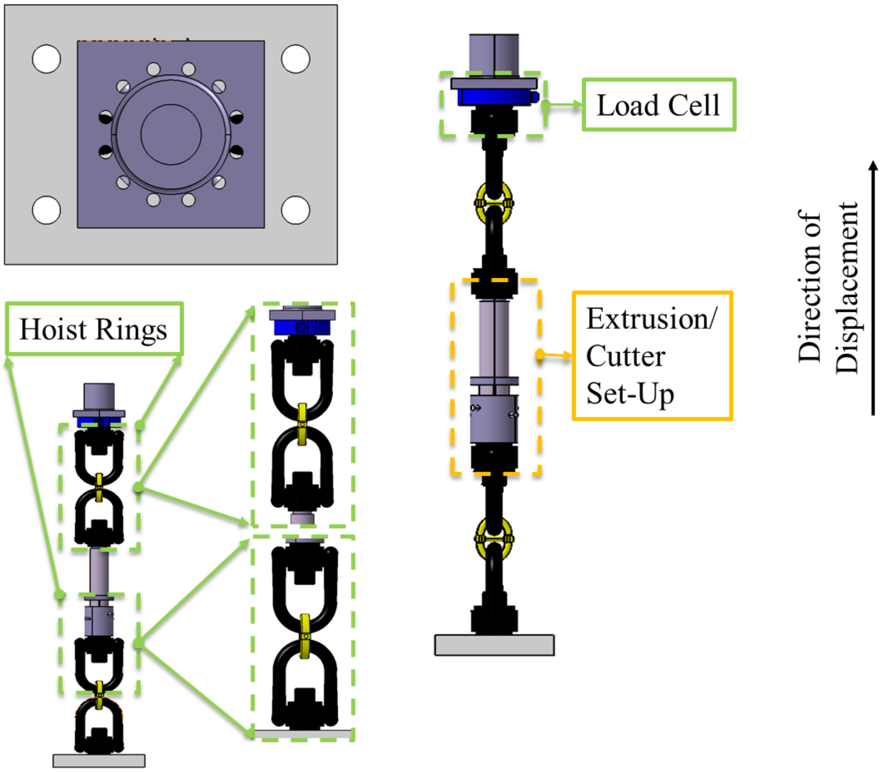

Figure 21: Tensile axial cutting apparatus set-up in the virtual CAD environment within CATIA.

3.3: Tensile testing apparatus

The experiments were completed utilizing a custom-built tension/compression hydraulically powered long stroke machine. Figure 22 illustrates a schematic of the tensile axial cutting process, followed by the full-scale testing apparatus set-up. As explained within the prior sub-section, one end of the extrusion, with the machined slots and holes, was anchored near the base of the machine as the cutting tool was displaced upwards through the extrusion. The maximum load capacity of the long stroke machine was 300 kN. The maximum expected loads which were predicted within these experiments was 50 kN, which were far below the threshold of the machine. The data collection set-up implemented to measure the force response will be explained within this sub-section.

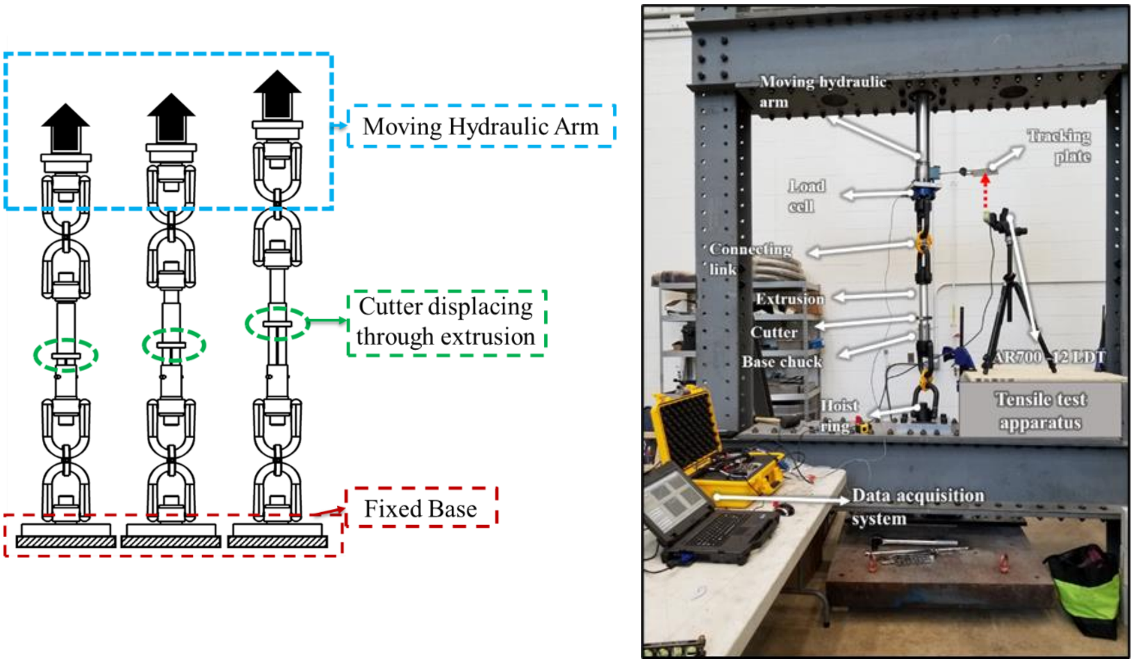

(a) (b)

Figure 22: Full test frame with tensile cutting apparatus shown (a) schematically, and (b) as tested.

The cutter was displaced through the extrusion between 150 mm to 180 mm, within 10 mm of the free end, varying between extrusion group categories. The displacement was conducted at a uniform pull rate of 275 mm/min. Displacement was recorded through the use of a AR700-12 non-contact laser displacement transducer with a range of 300 mm. The recording was initiated by the DAQ operator. A flat metal plate attached to the top of the hydraulic arm was utilized as a reference point to gauge displacement. The forces encountered within the experiments were measured with a PCB 1204-13A strain-gauge based load cell, with a maximum force capacity of 222 kN. The load cell was fastened to the hydraulic arm of the long stroke machine with twelve M10 fasteners, with a maximum total load capacity of 180 kN. A National Instruments NI 9215, 16-bit voltage input module was utilized to collect data from the laser displacement transducer and a NI 9237, 24-bit bridge module was utilized to collect voltage data from the load cell. Both these modules were connected to a NI CompactDAQ system (cDAQ-9178) with a sampling rate of 2kHz to synchronize the measurements. The CompactDAQ system was connected to a laptop running a custom LabVIEW® program to compile the data and compute the mechanical performance parameters and force responses.

3.4: Specimen grouping

The categorization of the extrusions utilized within this study followed the general labelling scheme: 'T-D-W', where 'T' refers to the temper condition of the extrusions (T6 or T4), 'D' refers to the outer diameter of the extrusions (63.5 mm or 50.8 mm) and 'W' refers to the wall thickness or the wall thickness profile of the extrusions (straight-sectioned; 3.175 mm, 1.588 mm and 1.25 mm or passively adaptive; PA1, PA2 and PA3). The schematics for the passively adaptive geometries are illustrated in **Error! Reference source not found.**. A total of three different tests were conducted within each test category. The repeatability of the experiments was examined in this way. A total of 72 tests were proposed in the parametric scope. The parametric scope is presented within Table 5.

Table 5: Parametric scope for AA6061 extrusions subjected to tensile cutting.

Material	Outer diameter [mm]	Wall thickness [mm]	Loading rate [mm/min]
6061-T6	50.8	1.250 (straight)	275
6061-T4	63.5	1.588 (straight)	275
		3.175 (straight)	275
		PA1 (adaptive)	275
		PA2 (adaptive)	275
		PA3 (adaptive)	275

3.5: Performance parameters

The performance parameters utilized within this investigation aid in identifying critical mechanical capabilities of each extrusion category. The parameters utilized will be explained in this sub-section. The total energy absorbed, *TEA*, is as the name implies the total amount of energy absorbed through the experiment. It is defined as the area under the force displacement response. It is numerically calculated as the integral of the tensile cutting force over the displacement domain, as shown in Equation (19). It was computed within this document utilizing the discrete formulation presented in Equation (20).

$$TEA = \int_{\delta_{total}} P(x)dx \tag{19}$$

$$TEA = \sum_{i=1}^{n-2} P_i \cdot \left(\frac{\delta_{i+1} - \delta_{i-1}}{2}\right) \tag{20}$$

The *TEA* was the crucial metric from which the mean cutting force, P_m and the specific energy absorbed, *SEA*, were computed. The P_m was computed by dividing the *TEA* by the maximum displacement. The expression utilized in this study is presented in Equation (21).

$$P_m = \frac{1}{\delta_{total}} \int_{\delta_{total}} P(x)dx = \frac{TEA}{\delta_{total}} \tag{21}$$

The *SEA* was computed to measure the effectiveness of the energy absorber in accordance with its mass, *m*. It was computed by normalizing the *TEA* with the total mass, *m*. The expression presented in Equation (22) was utilized to compute the *SEA*.

$$SEA = \frac{TEA}{m} \tag{22}$$

As one of the main benefits of axial cutting is that the force responses are highly stable, a performance parameter is required to quantify any fluctuations. The tensile force efficiency, *TFE,* is defined as the ratio between the mean cutting force, P_m, normalized with the maximum cutting force, P_{max}. This provides a ratio representing the amount of fluctuation which exists in the experimentally observed force response. A value closer to unity indicates that minimal fluctuations and highly stable loads were observed. The expression presented in Equation (23) was utilized to compute this value.

$$TFE = \frac{P_m}{P_{max}} \tag{23}$$

Chapter 4: Finite Element Modelling

Finite element (FE) models were created to better understand the tensile axial cutting process, in terms of mechanics of energy dissipation and deformation. The geometries which were modelled within this study included extrusion outer diameters of 63.5 mm and 50.8 mm, with wall thicknesses of 3.175 mm and 1.59 mm and adaptive geometries PA1 and PA2 in both the T6 and T4 temper conditions. Each of these test categories were simulated in quasi-static test conditions to reflect the nature of the experimental testing. In order to simplify the FE model both in terms of complexity and computational time, quarter symmetry models were created. They were determined to be sufficient due to the symmetric nature of this deformation mode observed experimentally. The explicit, non-linear FEA solver LS-DYNA® was utilized to run these simulations using a double precision, SMP solver platform at a displacement rate of 10 mm/ms.

In the modelling of extremely large deformation problems and especially cutting processes, Eulerian element formulations with a material-in-void approach are typically employed [54, 67, 68, 69]. It has been utilized to numerically model axial cutting in compression and has established to provide high accuracy prediction results, with validation metrics up to 90% and provides accurate replication of the observed deformation modes present in experiments [7, 44]. This approach is advantageous in modelling ductile materials which experience extremely large deformations, since the material and the mesh are decoupled. The need for failure algorithms is eliminated as the material is free to ‘flow’ through a fixed Eulerian mesh. An initial Lagrangian step is utilized to calculate the deformed state of the material and the mesh, subsequently followed by a remapping of the mesh (advection), while the material remains in its deformed state, within a partially void, airmesh. The airmesh is intentionally oversized in order to capture large amounts of deformation detail. Utilizing this rationale, an Eulerian element formulation with a material-in-void approach was employed to model axial cutting in tension. Eulerian models are time consuming and computationally expensive. In addition to the previously mentioned quarter symmetry, a coupled Eulerian-Lagrange model was developed.

4.1: Coupled Eulerian-Lagrangian Approach

Due to the design of the extrusions utilized in this study, the bottom end of the extrusion, secured to the base block through steel dowels, does not experience any deformation from cutting. As such, it was reasonable for this portion of the extrusions to be modelled using less expensive Lagrangian elements. However, the upper portion of the extrusion experienced massive deformation as the cutter blade plowed and split through it and employed an Eulerian element formulation. The two halves of the extrusions were confined to each other through a penalty based nodal coupling keyword with coincident node sets and the *ALE_COUPLING_NODAL_PENTALTY keyword command. The purpose of this keyword was to provide a coupling mechanism between Eulerian and non-Eulerian elements. Due to the nature of penalty-based coupling methods, the penalty stiffness was manipulated until the two parts remained seamlessly fixed throughout the simulation. This method led to a significant reduction in the total number of nodes and elements used within the model by about 33% and reduced the simulation times down by almost 40%.

Table 6 illustrates the key details and simulation times for the fully Eulerian and coupled models, respectively. Figure 23 illustrates the complete FE model for the fully Eulerian and Coupled Lagrangian-Eulerian simulations.

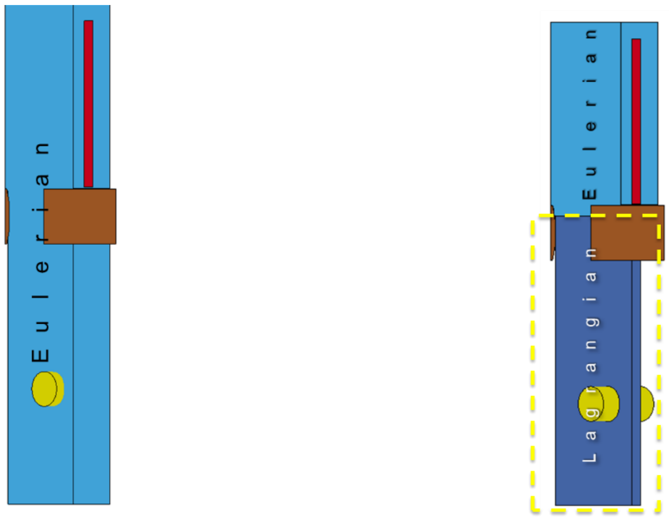

(a) (b)

Figure 23: Schematics of the (a) fully Eulerian extrusion, and (b) coupled Lagrangian-Eulerian extrusion.

Table 6: Key details for the Eulerian and Coupled tensile axial cutting numerical models.

	Eulerian Model	Coupled Model
Solver Name	LS-DYNA R11.0, double precision (explicit time integration)	LS-DYNA R11.0, double precision (explicit time integration)
Element Types (Extrusion)	Eulerian	Eulerian and Lagrangian
Element Types (Fixturing and Cutter)	Lagrangian	Lagrangian
# of elements and nodes	3 382 207 Elements, 3 502 026 Nodes	1 440 927 Eulerian Elements, 908 305 Lagrangian Elements, 2 498 224 Nodes
Element size	0.4 mm	0.4 mm
Contact/coupling algorithm	Constrained Lagrange in Solid	Constrained Lagrange in Solid, Surface to Surface, ALE Coupling Nodal Penalty
Symmetry	1/4th circumferential	1/4th circumferential
Run time	SMP double precision 4 CPU's **150 hours**	SMP double precision 4 CPU's **90 hours** (~37% time savings)

4.2: Mesh Discretization

The meshing for the parts required within the simulations was carried out using a combination of the 2D sketcher and element generation tools on LS-PrePost v.4.3. The FE model consisted of 6 different parts, listed as follows: Eulerian extrusion, Lagrangian extrusion, air mesh, cutter, steel dowel and base block. The complete simulation set-up can be seen in Figure 24. Numerical models were created for specific test conditions, to provide models for both straight-section and passive adaptive extrusions, to simulate the quasi-static nature of the experiment. The extrusion/cutter apparatus within the numerical model was identical to the experiment, the hoist rings and connecting rings were ignored as no noticeable deformation of these entities was observed.

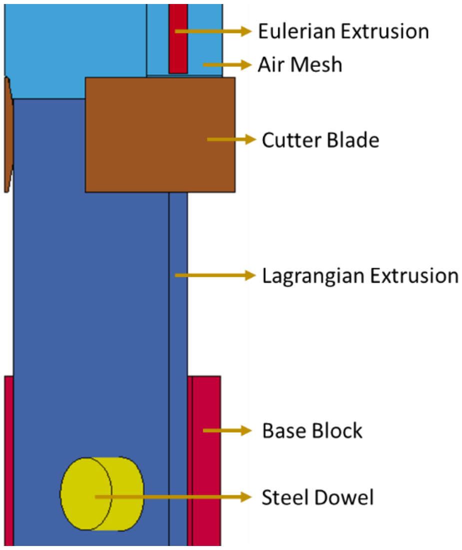

Figure 24: Extrusion-cutter set up within the FEA environment.

The Eulerian extrusion and the air mesh were modelled using eight-node solid elements. A single point integration scheme and a material and void formulation were utilized. The element generation tool was utilized to offset the curved solid faces of the extrusion outwards. A similar level of discretization was utilized for the airmesh and the Lagrangian extrusion, with eight solid elements through the extrusion’s thickness. This was done to ensure at least four integration points through the thickness of the extrusions in order to ensure that any nonlinearities in material or structural response. The aspect ratio of the elements in the extrusion and the air mesh was approximately unity. The 0.4 mm characteristic element length was justified by high quality results summarized in prior mesh sensitivity studies [44, 7];

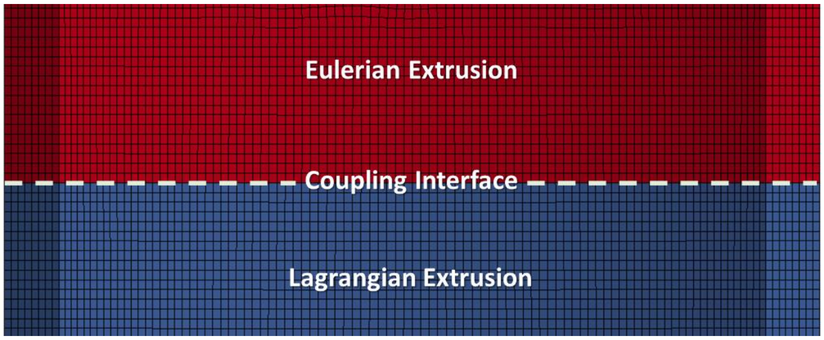

Figure 25: Coupling interface between the Eulerian and Lagrangian element interfaces.

The cutter blades, steel dowel and base block were meshed using eight-node solid elements. The mesh size utilized was consistent with the extrusion and air mesh in order to ensure proper coupling within contact algorithms. The parts mentioned above were all modelled using constant stress solid elements. Experimental evidence indicates that the cutter has survived hundreds of prior tests without degradation, the remainder of the fixturing mechanisms were comprised of 4140 heat-treated steel and the test samples were comprised of AA6061, these facts coupled together led to the conclusion that deformation in the steel cutter and fixturing mechanisms would be miniscule as such, a rigid material model was deemed sufficient. Since the dowels were positioned inside the base block, to ensure better element alignment between the two parts for the contact algorithm, solid mesh elements of the same size were utilized.

4.3: Contact and Coupling

Several different contact algorithms were implemented within the numerical model. A penalty-based coupling scheme was implemented to initiate contact between the Lagrangian cutter and the Eulerian extrusion material. Coupling was implemented in the normal direction and a coefficient of friction of 0.125 was utilized which was consistent with the value used in previously completed simulations for compressive axial cutting [44, 68]. This value is lower than values measured in dry sliding experiments between steel and aluminum. The rationale behind this variance in values is that the contact algorithm modelling on LS-DYNA® is different when compared to the real-life phenomenon of contact and does not completely replicate the nonlinear properties of real contact. Reid and Hiser [70] provide guidelines for accurately modelling friction between solid elements, including: the use of fully integrated elements, avoidance of sharp corners, fine meshes and the utilization of a lower frictional coefficient value. Wang et. al [71] conducted a study similarly exploring the effects of friction in a rough surface contact problem, they concluded that lower coefficients of friction were required for accurate modelling of contact problems. Values as low as 0.1-0.2 were utilized to provide accurate predictions. A part-based, surface to surface contact algorithm was utilized to provide contact between the steel dowels, Lagrangian extrusion and the base block. Static and dynamic coefficients of friction of 0.3 and 0.25 were used, respectively. Finally, the coupling between the Lagrangian and Eulerian nodes of the extrusion was accomplished with the implementation of a penalty-based ALE nodal coupling algorithm. A mass-based penalty stiffness formulation was utilized in tandem with a coincident node-set between the two halves of the extrusion. A penalty stiffness factor of 0.005 was implemented to provide strong coupling between the two parts. A large array of penalty stiffness values was explored to determine an accurate value until good coupling was achieved.

4.4: Boundary Conditions

Symmetry planes were established in the xz and yz planes, using node sets, as illustrated in Figure 26. The symmetry planes were defined along the corresponding edges of the Lagrangian and Eulerian extrusions, the cutter blades and the base block. The base block was constrained in all degrees of freedom, to imitate the anchored base similar to the experimental test set-up. The steel dowel was constrained to motion only in the axial direction. However, the contact algorithm implemented between the base block and the dowel ensured that the remaining degrees of freedom of the dowel were constrained. A prescribed motion in the axial direction was defined and a displacement amount of 150 mm was implemented for the cutter. The total kinetic energy of the system was significantly below 10% of the total internal energy associated with the cutting process and the reaction force at the pin was near identical to the reaction force at the cutter blades, as such those simulations were deemed to be quasi-static.

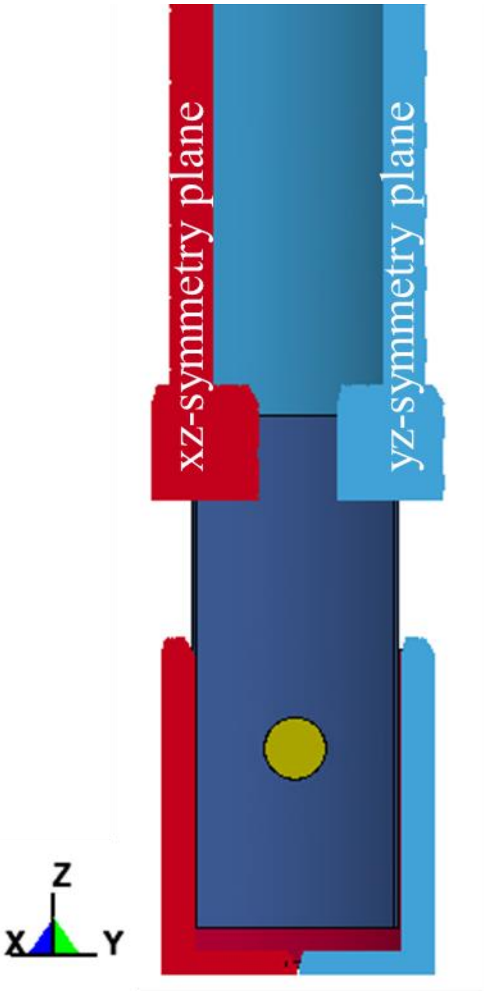

Figure 26: Symmetry planes selected for quarter symmetry numerical model.

4.5: Material Modelling

The extrusions explored in this study were comprised of AA6061 of a T6 and T4 temper. An elastic plastic hydrodynamic material model was utilized to simulate the mechanical behaviour of the material. The stress/strain behavior of the two temper conditions during plasticity was expressed in the material model through sixteen discrete data points which were determined through the stress/strain responses shown in Figure 18. The elastic plastic hydrodynamic material model required an input for an equation of state to estimate the bulk modulus. A linear polynomial equation of state was utilized for this purpose and all other inputs for the polynomial coefficients of this equation were set to zero. The remainder of the properties for the material model are presented in Table 4, which can be found in Section 3.1. A rigid material model was applied to the cutting tool, the dowel, and the base block. Additionally, the base block was fabricated from 4140 heat treated steel with a much higher hardness than the AA6061. The dowels were composed of 4140 steel with a breaking strength far exceeding any forces encountered during the tests. Since each of these parts were much stronger than the AA6061 structures, and experimental observations indicated minor or no deformation for these parts, a rigid material model was deemed sufficient for modelling purposes.

Chapter 5: Validation Parameters

The analytical and numerical models were compared to the experimental results and the quality of these models. Two approaches were considered in this quantitative assessment. The first was the capacity of the models to predict key performance parameters, mentioned within the prior sub-section. The overall accuracy of the prediction of the complete force-displacement response over the total domain of displacement was computed through the utilization of a validation metric, V_M, and cumulative error, C.

The predictability of the key performance parameters was assessed through computation of the relative error, R_Q, shown in Equation (24). The Q_{exp} term represents the experimentally observed value, while Q_{th} represents the theoretical value computed through either the analytical or numerical model.

$$R_Q = \left|\frac{Q_{exp} - Q_{th}}{Q_{th}}\right| \tag{24}$$

The overall accuracy throughout the force-displacement response was computed through parameters presented by Oberkampf and Trucano [72]. These parameters, as previously mentioned, were the validation metric and cumulative metric. The validation metric is computed as a value between zero and one, with zero representing low accuracy and one representing high accuracy. The expression utilized to compute the validation metric is highlighted in Equation (25) as an integral over the total displacement domain. The numerical approach of computing this parameter was utilized within this study as discrete data points were recorded during the experiments. This numerical approach is shown in Equation (25) and (26). The letter N within this expression represents the total number of data points, to encapsulate the entirety of the test. $y(x)$ and $Y(x)$ represent the estimated/predicted and experimental instantaneous force-displacement responses, respectively.

$$V_M = 1 - \frac{1}{\delta_{total}} \int_0^{\delta_{total}} \tanh \left| \frac{y(x) - Y(x)}{Y(x)} \right| dx \tag{25}$$

$$V_M = 1 - \frac{1}{N} \sum_{i=1}^{N} \tanh \left| \frac{y(x_i) - Y(x_i)}{Y(x_i)} \right| \tag{26}$$

The cumulative error was computed through the domain of displacement. This metric is a measure of the error which exists throughout the domain of displacement. The degree of cumulative error within an experiment is computed as a value from zero to values higher than one. Since this is a measure of error, a value of zero represents a low degree of error, whereas a value closer to one or higher presents a high degree of error. The mathematical expression is presented in Equation (27) and is computed over the domain of displacement. Since discrete data points were collected within this study, the numerical approximation was utilized to compute the cumulative error. The expression for this numerical approximation is presented in Equation (29).

$$C = \frac{1}{\delta_{total}} \int_0^{\delta_{total}} \left| \frac{y(x) - Y(x)}{Y(x)} \right| dx \tag{28}$$

$$C = \frac{1}{N} \sum_{i=1}^{N} \left| \frac{y(x) - Y(x)}{Y(x)} \right| \tag{29}$$

Chapter 6: Observations and Discussions

6.1: Overview

The following section is divided into two sub-sections. The first will explore the mechanical performance of the straight sectioned/unmodified extrusions, with consistent wall thickness profiles along their axial length. The second section highlights the experimental findings of the passive adaptive extrusions, labelled as PA1, PA2 and PA3. Generally, within all these experimental results, a transient loading regime which lasts for approximately 12 mm of displacement is evident. This transient loading regime leads into the steady state force region.

The parametric scope of this research was selected to illustrate the stability and repeatability within experimentally tested extrusions. As such, out of the each of the 24 mentioned test categories, through variations in material and geometries, three tests were completed to illustrate the high degree of repeatability within each category. A representative experimentally tested extrusion is shown in Figure 27 to provide a visual demonstration of the tensile cutting deformation mode.

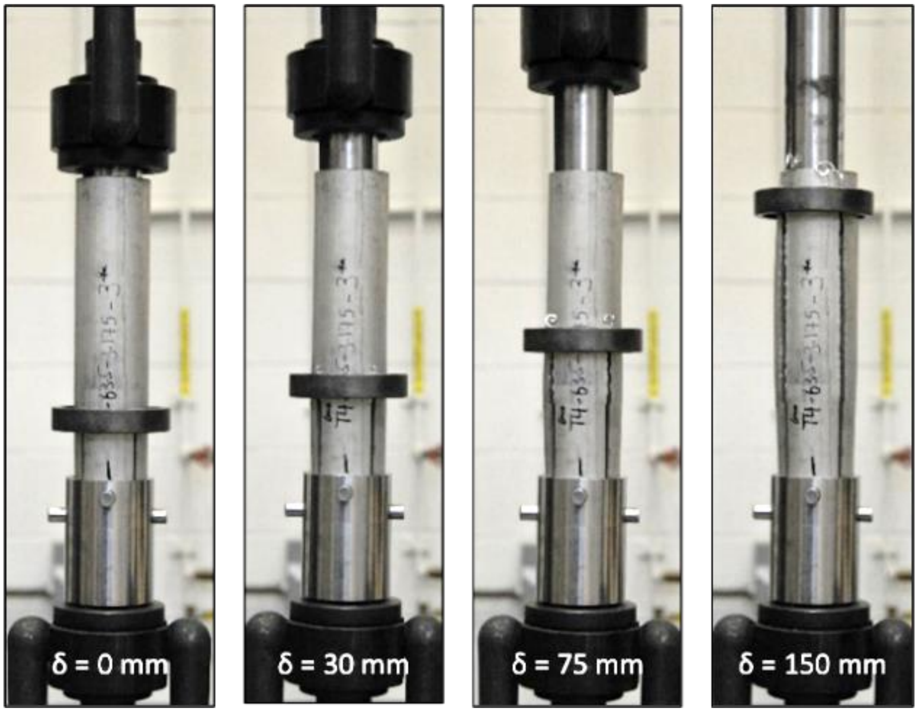

Figure 27: Deformation of the extrusion through the displacement domain.

An analysis was completed on the repeatability, utilizing the mean force within each test category. Mean forces were plotted for each test category, with error bars to indicate the amount of deviation from these values. The deviation is very low for the majority of the test categories, with the highest deviation occurring within the PA1 and PA2 T4 categories. The underlying rationale behind the higher deviation within this test will be explored further in this section, when discussing the corresponding test category. This error plot is presented within Figure 28. Discussion of the experimental results is provided within the following subsections, with Figure 29 to Figure 54 illustrating the force-displacement responses of the experiments. A complete list of experimental results is provided in Appendix C.

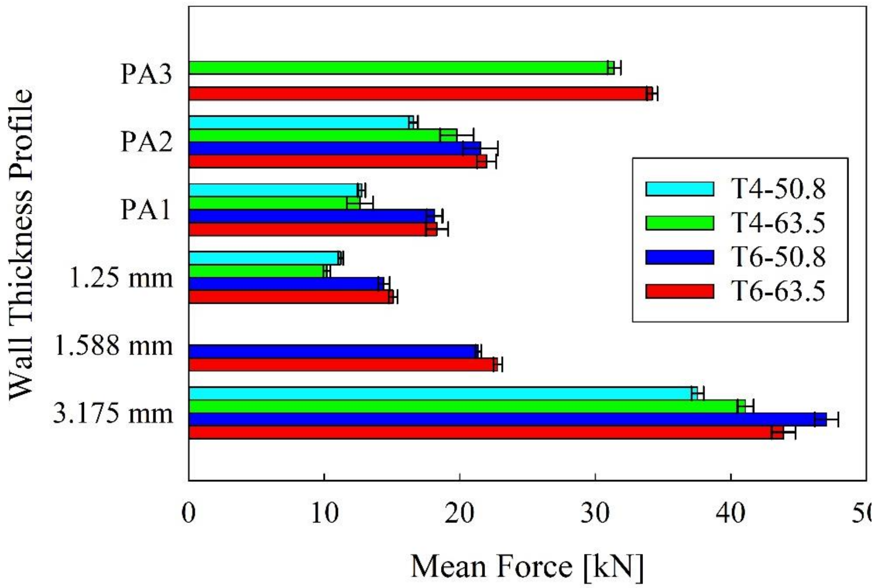

Figure 28: Repeatability observed during experimental testing for the average mean tensile cutting forces.

6.2: Straight-Sectioned Geometries

6.2.1: 3.175 mm Wall Thickness Extrusions

The 63.5-T6-3.175 test category presented some of the highest values in terms of mean forces, *TEA*, *SEA* and *TFE*. They presented less deviation from ideal axial cutting conditions due to their higher wall thickness. The tests presented *TFE* values averaging 92.23%. The mean force within this test category was 43.34 kN. The *TEA* and *SEA* values were 7.59 kJ and 16.29 kJ/kg, respectively. There is a slight visible deviation in between tests, and this is attributed to slight differences in the wall thicknesses of the extrusions which varied, both axially and circumferentially. Measurements were obtained prior to testing and this slight variation was expected, as the steady state force is highly sensitive to small changes in extrusion thickness. The measurements for all of the extrusions experimentally tested can be found within Appendix D Figure 29 presents the force responses for this test category.

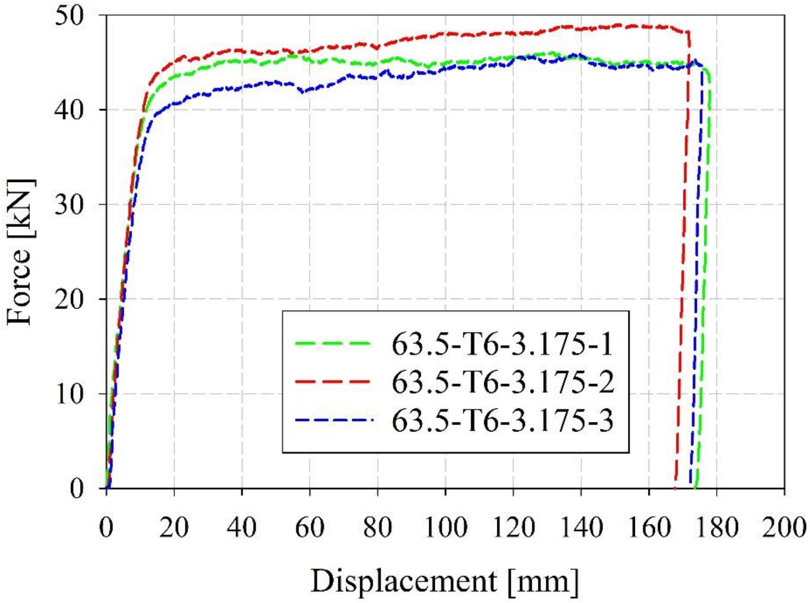

Figure 29: Force-displacement responses for the 63.5-T6-3.175 extrusions.

The 63.5-T4-3.175 test category extrusions provided far higher stability in terms of force response and repeatability in between tests. This is attributed to the more consistent wall thickness present within extrusions in this grouping. The temper condition of these extrusions presented a slightly lower force response and energy absorption capability than its T6 counterparts. The T4 extrusions also presented slightly more ductile behaviour, which will be further explored and elaborated upon further within this subsection. The mean force within this test category was 41.08 kN. The average *TFE* value was extremely high at approximately 94.27%, indicating high stability, with minimal force fluctuations. The average *TEA* and *SEA* values were 7.19 kJ and 14.84 kJ/kg, respectively. The corresponding force-responses are presented in Figure 30.

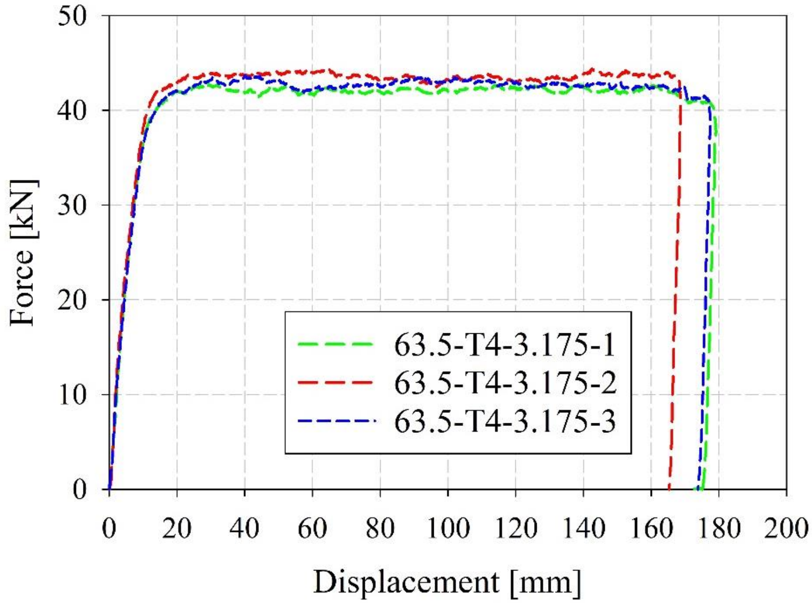

Figure 30: Force-displacement responses for the 63.5-T4-3.175 extrusions.

Figure 31 presents the test results for the 50.8-T6-3.175 extrusions. The first and most obvious difference which can be observed between these two test categories is that the force response is more or less similar to that of the 63.5-T6-3.175 extrusions. This illustrates that slight changes within diameter are not as influential on the force response. The second key difference is that the force response for this category presents more stability and repeatability in comparison to the 63.5-T6-3.175 extrusions. Once again, this is attributed to slightly more consistent wall thickness profiles, both axially and circumferentially. The mean force within this category was 47.07 kN. The average *TFE* value was 93.08%. The average *TEA* and *SEA* values were 8.46 kJ and 17.74 kJ/kg, respectively.

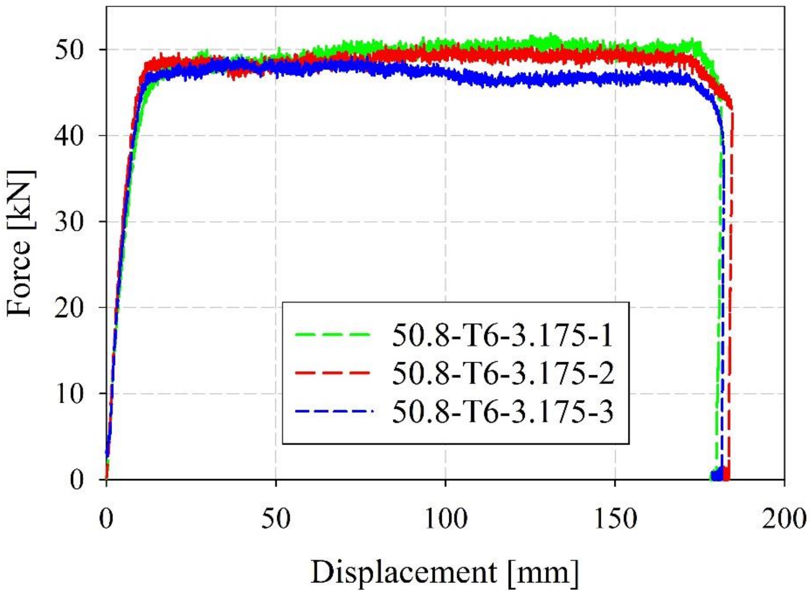

Figure 31: Force-displacement responses for the 50.8-T6-3.175 extrusions.

The results for the 50.8-T4-3.175 extrusions is presented within Figure 32. As with the prior tests within this category, high stability and repeatability were observed. Similar force responses are presented in comparison to the T4-63.5-3.175 category, once again indicating the low influence of extrusion diameter. The average value for the mean force was 37.55 kN. The average *TFE* value was 91.76%, exhibiting high stability. The *TEA* and *SEA* values were 6.42 kJ and 17.75 kJ/kg, respectively.

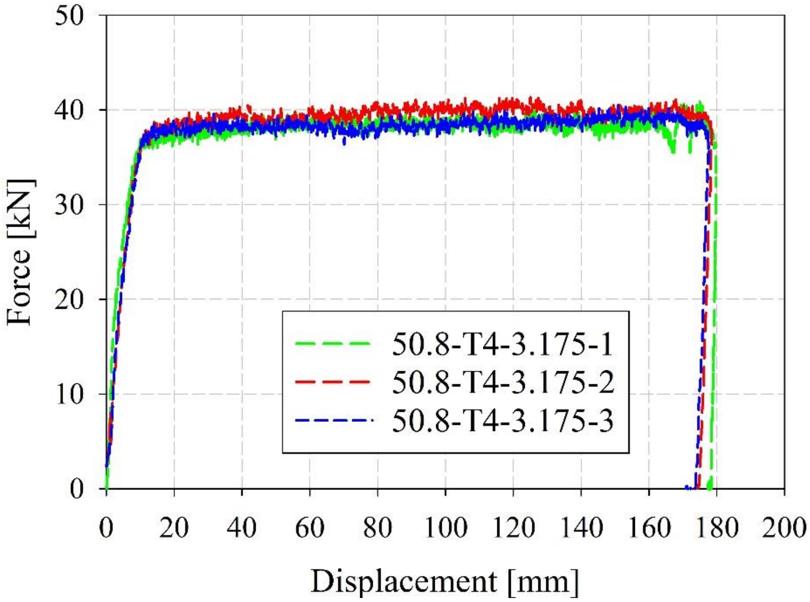

Figure 32: Force-displacement responses for the 50.8-T4-3.175 extrusions.

6.2.2: 1.59 mm Wall Thickness

The test extrusions for the 1.59 mm wall thickness specimen grouping presented a few more observations in comparison to the 3.18 mm wall thickness extrusions. They presented high stability and repeatability, however, these extrusions presented the first signs of limitations in terms of the energy absorbers, in terms of pin pull out failure at the steel dowels. The 50.8-T6-1.59 extrusions exhibited lower force responses in comparison to their 3.18 mm counterparts, due to their lower wall thickness. The reduced thickness led to a lower energy absorber mass and as a result, the *SEA* values remained comparable to the 3.175 mm extrusions, the total energy absorption capability, which relies on the mean force however, was lower. The average *TFE* value observed was 92.37%, indicating high stability. The mean cutting force was 22.79 kN. The average *TEA* and *SEA* values were 3.44 kJ and 15.55 kJ/kg, respectively. The corresponding force responses for the three extrusions in this category are exhibited in Figure 33.

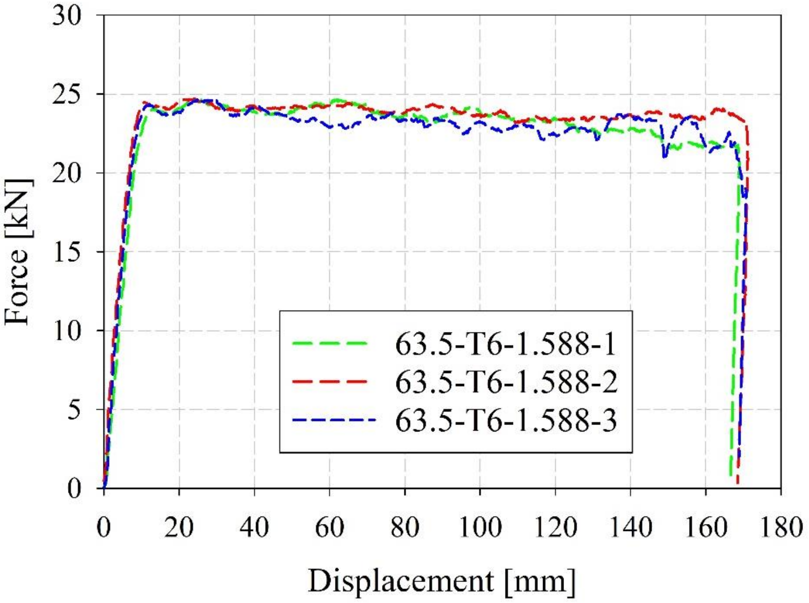

Figure 33: Force-displacement responses for the 63.5-T6-1.588 extrusions.

The results for the 50.8-T6-1.59 category of extrusions are presented in Figure 34. The force responses of this category in comparison to the 63.5-T6-1.59 category were nearly identical. The mean force was approximately 2 kN lower, however this was attributed to inconsistent thickness rather than the change in diameter. The average force was 20.88 kN. The average *TFE* was 91.53%. The *TEA* and *SEA* were 3.47 kJ and 17.58 kJ/kg, respectively.

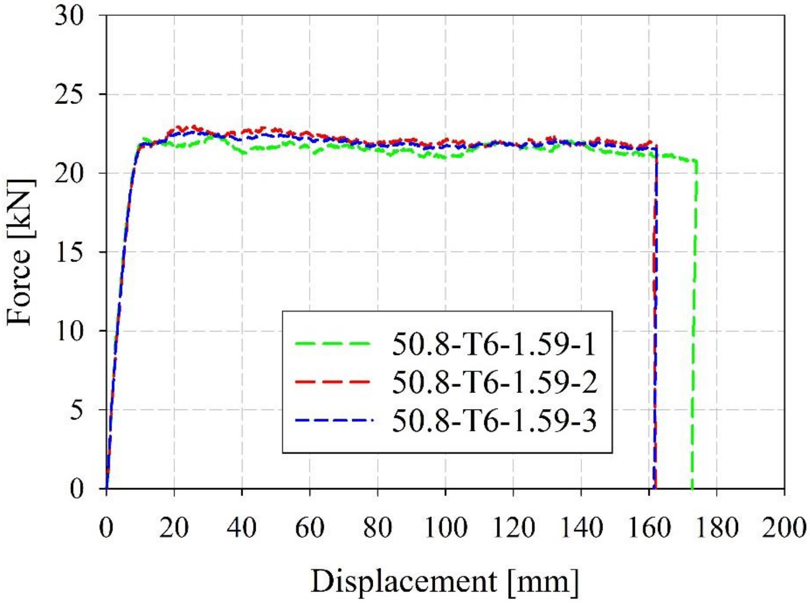

Figure 34: Force-displacement responses for the 50.8-T6-1.588 extrusions.

The 63.5/50.8-T4-1.59 categories of extrusions presented the first instances of failure in the tensile axial cutting deformation mode. As indicated within Chapter 3, the anchoring mechanism involved the utilization of steel dowels through holes machined into the extrusion surface. Due to the increased ductility of the T4 tempered material and the reaction force at the dowel holes, a large amount of localized stretching occurred at the anchoring interface. A pull-out failure mode at the pins occurred as illustrated in Figure 35.

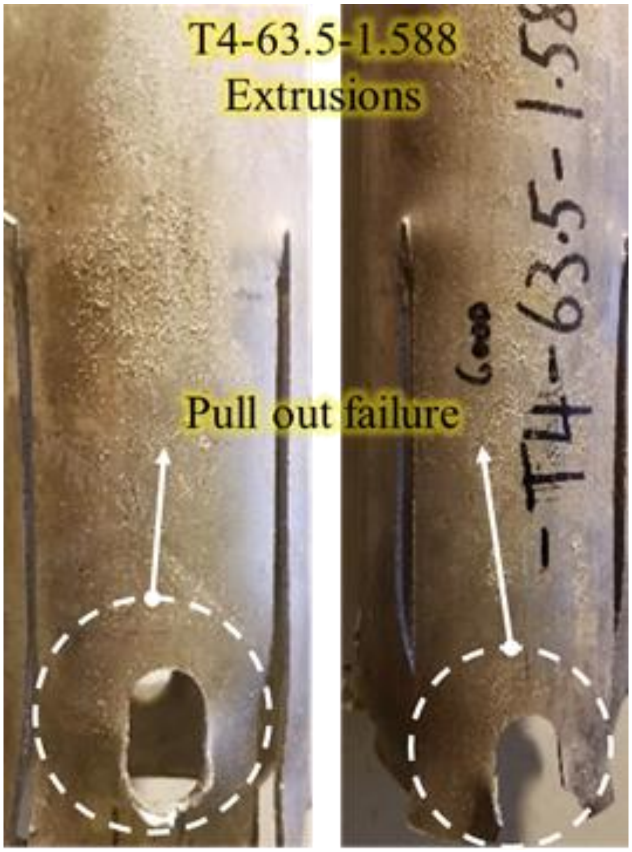

Figure 35: Pin pull-out failure deformation mode present within the 63.5/50.8-T4-1.588 category of extrusions.

This problem was only present in the T4 tempered extrusions of this wall thickness and this presents a physical limitation to this anchorage mechanism. Figure 36 presents the force/displacement responses for both of the T4 extrusions in this category, it is readily observable that the force response was terminated prematurely. The 63.5 mm OD extrusions failed slightly later than the 50.8 mm OD extrusions, indicated by slightly higher force responses. As a result, the performance parameters were not computed for this test category.

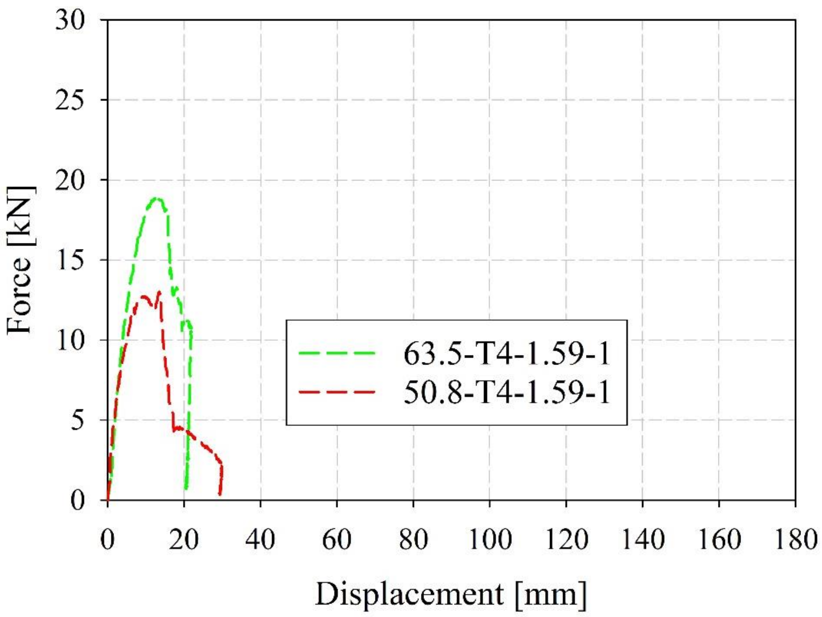

Figure 36: Force-displacement responses for the 63.5/50.8-T4-1.588 extrusions.

6.2.3: 1.25 mm Wall Thickness

The extrusions within the 1.25 mm wall thickness category presented far more instability than the other categories. This category presented the highest amount of instability out of all the tested categories. These extrusions were machined from the 1.59 mm wall thickness extrusions, the wall thickness of these extrusions was turned down utilizing a lathe. High stability was observed within the 1.59 mm wall thickness extrusions, and this was directly related to the higher wall thickness. The instability observed was attributed to a culmination of several factors. The main issue was related to the extremely low wall thickness. As a result, the cutter displaced in the transverse directions in addition to the axial direction. This caused a twisting phenomenon within the extrusion, which is visible along the extrusion cut path. The secondary issue was the length of the extrusion along which this 1.25 mm wall thickness was implemented. The extrusion was approximately 190 mm long, and this whole region contained a 1.25 mm wall thickness, as a result, the further along the extrusion the cutter was displaced, the less resistance the extrusion was able to put up against any twisting or transverse displacement. This led to a reduction in the force response over time. The combination of these two factors led to the higher amount of instability. This twisting phenomenon is presented in Figure 37 (a). Additionally, the motion of the cutter and the fixture within the extrusion resulted in a transfer of the cross-section shape of the extrusion from circular to ovoid. This deformation is illustrated in Figure 37(b)

(a) (b)

Figure 37: (a) Twisting phenomenon caused by low wall thickness and instability, (b) ‘ovalization’ of extrusion cross section due to lateral motion of cutter and cutter fixture.

The 63.5-T6-1.25 category of the extrusions exhibited high repeatability. This provides evidence to support the idea that the low wall thickness was the reason that the force responses were unsteady, as this occurred consistently in all the extrusions of this category. High repeatability was observed, and similar performance parameters were measured within all of the tests. The mean load was quantified as 16.09 kN. The *TFE* was significantly lower than the previous 3.18 mm and 1.59 mm wall thickness extrusions. The average *TFE* was 83.56%. This is still an extremely high value in comparison to other energy absorbers within the tensile energy absorption field. The average *TEA* and *SEA* were 2.88 kJ and 15.07 kJ/kg, respectively. Figure 38 illustrates the force responses for this test category.

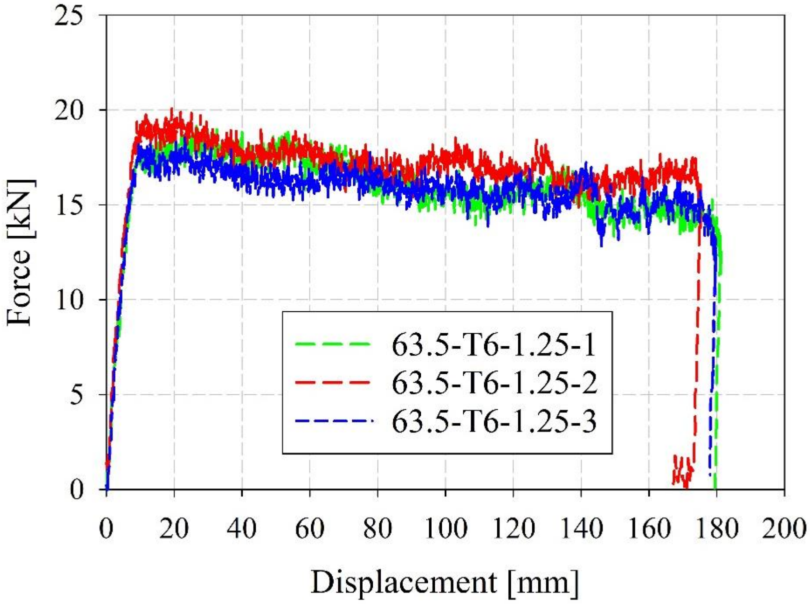

Figure 38: Force-displacement responses for the 63.5-T6-1.25 extrusions.

Extrusions within the 63.5-T4-1.25 category presented slightly more unstable and unpredictable responses. There was also a slightly high amount of deviation in terms of the mean load in between the force responses. The rationale behind this occurrence was that the ductility of the T4 material allowed the cutter to twist in a more free and uncontrolled fashion. The average force within these experiments was 11.28 kN. The average *TFE* value dropped even further within this category, with an average value of 79.25% through the three tests. The average *TEA* and *SEA* were 2.00 kJ and 10.17 kJ/kg, respectively. The force responses for this category are presented in Figure 39.

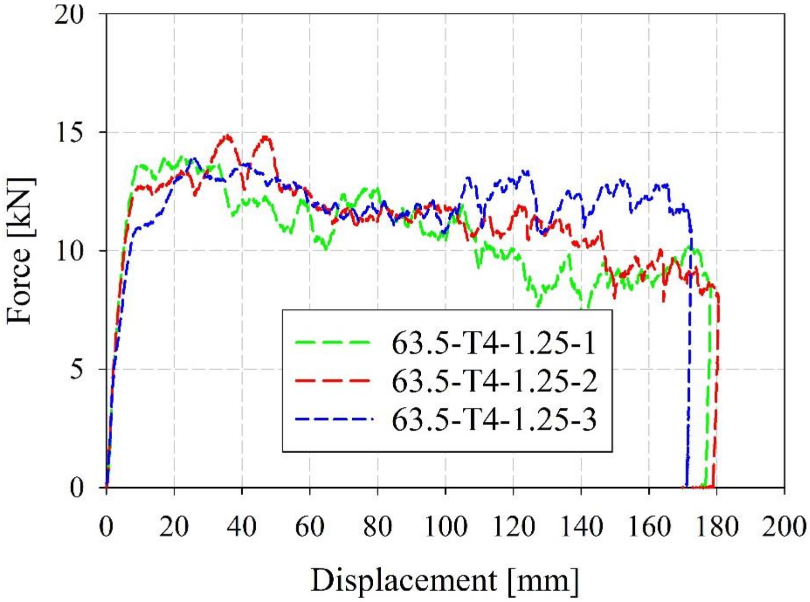

Figure 39: Force-displacement responses for the 63.5-T4-1.25 extrusions.

Figure 40 presents the experimental force responses for the 50.8-T6-1.25 category of extrusions. The repeatability within tests is very high and all the force responses start at a high force value of approximately 17 kN and reduced steadily to 13 kN. This is once again attributed to twisting which occurs due to extremely low resistance to out of plane motion of the cutter, as a result of low wall thickness. The average force for these tests was 14.39 kN. The average *TFE* was 82.47%. The average *TEA* and *SEA* values were 2.55 kJ and 25.72 kJ/kg, respectively.

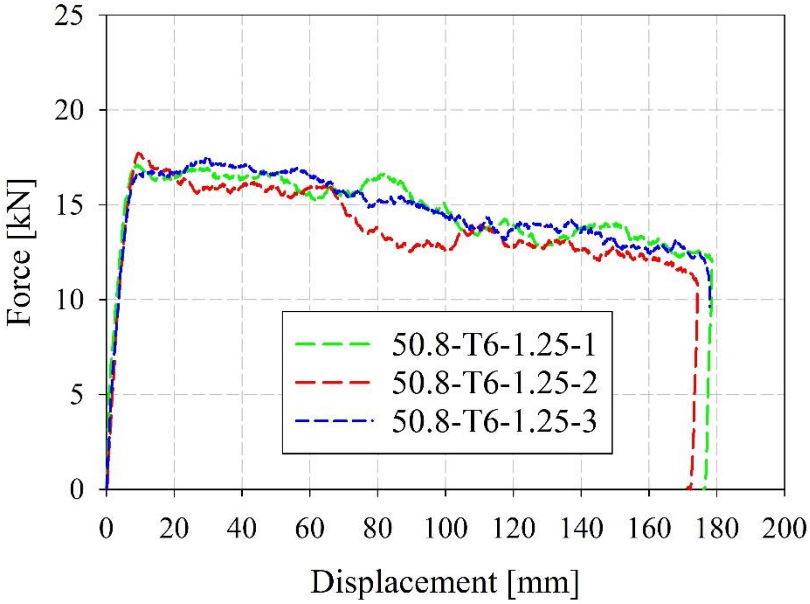

Figure 40: Force-displacement responses for the 50.8-T6-1.25 extrusions.

The force responses for the 50.8-T4-1.25 category of extrusions are presented in Figure 41. This test category introduced another set of physical limitations within extrusion geometry. The combination of the increased ductility within the extrusion and the reduced amount of material around the extrusion dowel holes in comparison to the 63.5-T4-1.25 category extrusions, led to a pin pull out failure at the dowel holes. This failure mode is illustrated in Figure 42. This failure was only encountered in one of the extrusions out of the three which were tested. This was attributed to slight discrepancies in wall thickness around the vicinity of the dowel holes and slight increased thickness near the cutting blades. The performance parameters for the extrusion which failed were not computed. The average mean force for the remainder of the extrusions was 11.14 kN. The average *TFE* was 75.78%. The average *TEA* and *SEA* were 2.01 kJ and 13.55 kJ/kg, respectively.

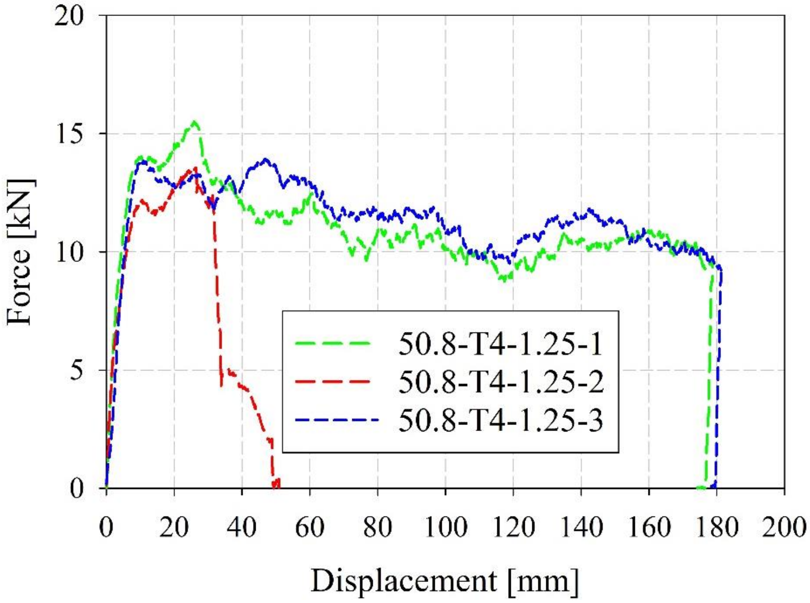

Figure 41: Force-displacement responses for the 50.8-T4-1.25 extrusions.

Figure 42: Pin pull-out failure mode in 50.8-T4-1.25 mm extrusion.

6.3: Passive Adaptive Geometries

This section is dedicated to the discussion of the experimental results for the extrusions exploiting passive adaptivity. There are three different geometries of passive adaptive extrusions, spanning across two temper conditions and two different diameters. Each of these will be discussed and a summary of the performance parameters are provided in the following sections.

6.3.1: Passive Adaptivity 1

This passive adaptivity geometry was created to provide three different force regions. Three different thickness regimes were machined into the extrusion to accommodate for the force regions. The first force region consisted of a wall thickness of 3.175 mm for approximately 40 mm, this was the thickest area of the extrusion, corresponding to the highest force region. The next part of the extrusion consisted of a 1.588 mm for a displacement of 75 mm, this corresponded to the medium force region of the extrusion. The final thickness regime of the extrusion consisted of a wall thickness of 0.794 mm for the remainder of the extrusion's length. This corresponded to the low force region of the extrusion.

The force-displacement responses for the 63.5-T6-PA1 category are presented in Figure 43. A high amount of repeatability and consistency in experimental observations is evident. The distinct load regions can be observed. One other observation which can be noted in this category and the remainder of the passive adaptive extrusion geometries is that they present steady force responses even with extremely low wall thicknesses of 0.794 mm in comparison to the 1.25 mm wall thickness extrusions. In comparison to the 1.25 mm wall thickness extrusions, the PA1 extrusions had higher wall thicknesses in the vicinity of the dowel holes, this led to higher stability and resistance to twisting. This higher wall thickness around the dowel holes led to higher stability which prevented the twisting which was noticed in the 1.25 mm wall thickness extrusions. The predicted behavior of the extrusions was highly consistent to the experimental results. The *TFE* was not computed for these extrusions as the force was designed to vary along the axial length of the extrusions. The average *TEA* and *SEA* were 3.88 kJ and 14.04 kJ/kg, respectively. The mean force was 22.67 kN.

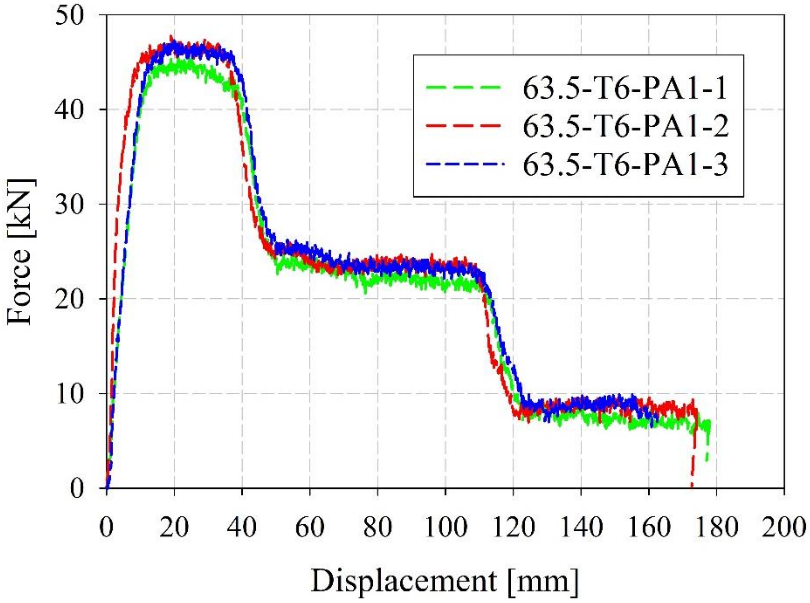

Figure 43: Force-displacement responses for the 63.5-T6-PA1 extrusions.

The force-displacement responses for specimens within the 63.5-T4-PA1 grouping are presented in Figure 44. These extrusions presented similar repeatability and consistency. The immediately visible difference is that one of the extrusions produces a force response that is approximately 3 kN lower than its counterparts, consistently through the experiment. This discrepancy was noticed in previous cutting experiments between T4 extrusions and could be caused by slight variations in the temper conditions between these extrusions. This could be caused by the extrusion being exposed to irregularities during the heat treatment process. This variation was present in prior experimental testing [46]. Additionally, measurements taken prior to testing presented variations in extrusion thickness in some regions. The mean force within this category was 18.69 kN. The average *TEA* and *SEA* were 3.31 kJ and 11.78 kJ.kg, respectively.

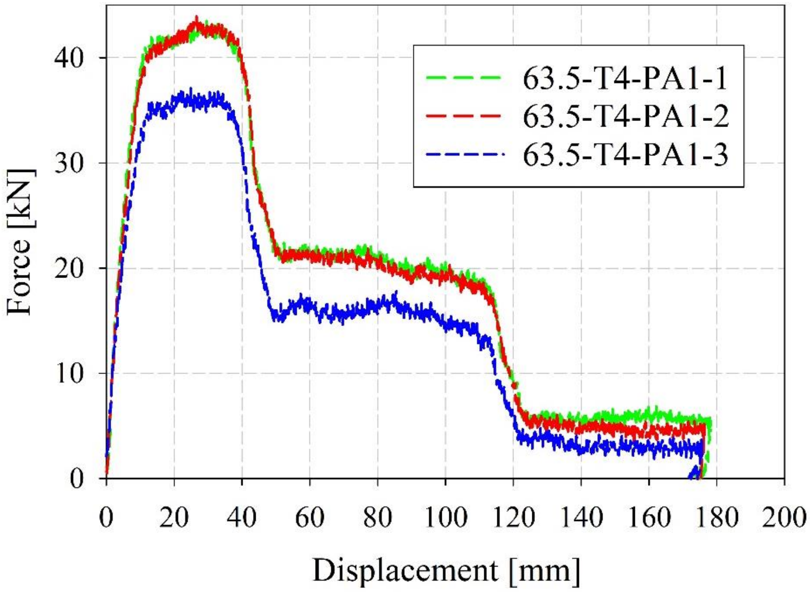

Figure 44: Force-displacement responses for the 63.5-T4-PA1 extrusions.

The force responses for the 50.8-T6-PA1 extrusions are presented in Figure 45. The stability of the force responses was highly consistent. However, one of the extrusions presented transition between the force regimes slightly quicker than the remainder of the extrusions. This is attributed directly to premature initiation of the test. A slight amount of the extrusion in the vicinity of 5 mm was cut prior to the collection of data. This is the reason for the discrepancy. It should be noted that the forces encountered in the three different regimes and the length of the transition between the regimes are almost identical between the experiments. The average force was 21.93 kN. The average *TEA* and *SEA* were 3.62 kJ and 16.90 kJ/kg, respectively.

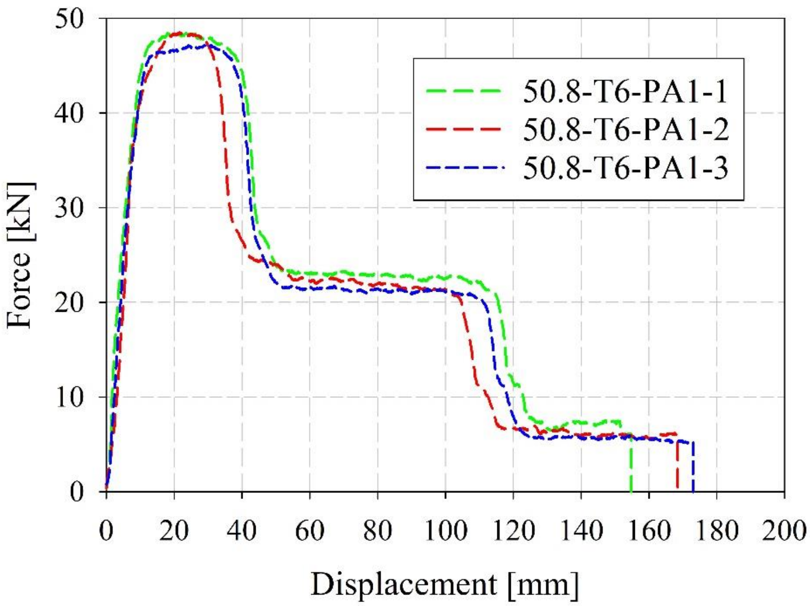

Figure 45: Force-displacement responses for the 50.8-T6-PA1 extrusions.

The force displacement responses for the 50.8-T4-PA1 extrusions are presented in Figure 46. It should be noted that the stability and repeatability of these force responses in comparison to the 63.5-T4-PA1 extrusions are much higher. The force responses are nearly identical and the fluctuations occur identically to each other. The only inconsistency was that the force during the high force regime of the extrusion labelled '50.8-T4-PA1-2' was slightly lower than the remainder of the extrusions. This is attributed to slight variation with the extrusions wall thickness in that regime. This is further indication that the discrepancies which occurred in the 63.5-T4-PA1 extrusions is due to the temper condition varying between the T4 extrusions. The average force between the three tests was 16.57 kN. The average *TEA* and *SEA* were 3.04 kJ and 14.08 kJ/kg, respectively.

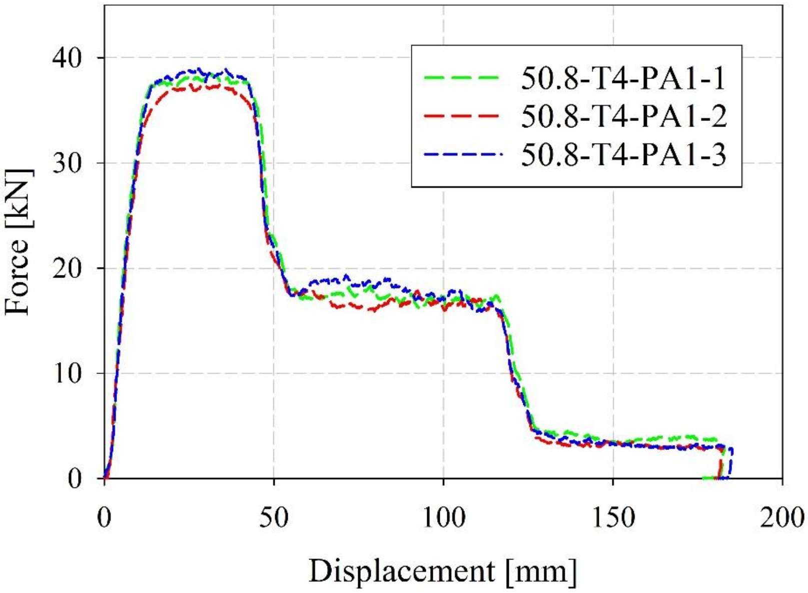

Figure 46: Force-displacement responses for the 50.8-T4-PA1 extrusions.

6.3.2: Passive Adaptivity 2

The second passive adaptive extrusion geometry selected for experimentation followed a similar trend as the PA1 extrusion grouping. There are four distinct force regimes within this category, instead of three. The high force regime consists of a wall thickness of 3.175 mm, which persisted for 40 mm. This was followed by a step decrease in thickness to 1.588 mm, indicating the medium force region, which persisted for 60 mm. A linearly varying wall thickness profile with wall thickness varying from 1.588 mm to 0.799 mm was machined into the extrusion, this region lasted for a domain of 30 mm. Finally, a low force regime with a wall thickness of 0.799 mm was present for the remainder of the displacement domain.

The 63.5-T6-PA2 extrusions exhibited the force responses presented in Figure 47. Two out of the three extrusions presented high repeatability and stability. The extrusion labelled ‘63.5-T6-PA2-2’ presented a slight deviation from the other two extrusions in this category. This deviation occurs during the medium force regime, where the force within this extrusion is higher than the remainder of the extrusions of this category. This is largely attributed to slight variations in thickness in this regime. This was confirmed by comparison to the measurements of the extrusions taken prior to experimentations. A second slight inconsistency is present at high force regime of the extrusion labelled ’63.5-T6-PA2-1’. This is once again attributed to slight variations in extrusion thickness in this regime. The average mean force for this category was 17.70 kN. The average *TEA* and *SEA* were 3.16 kJ and 11.70 kJ/kg, respectively.

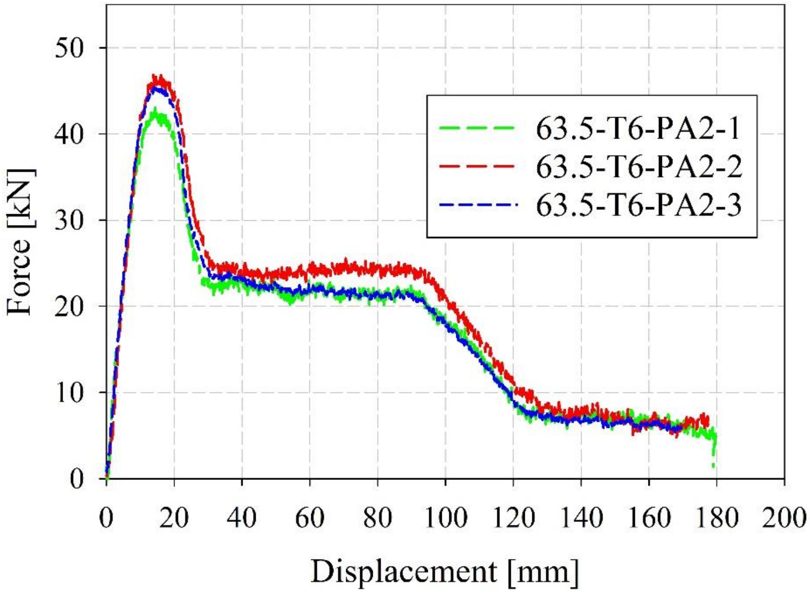

Figure 47: Force-displacement responses for the 63.5-T6-PA2 extrusions.

The force-displacement responses for the 63.5-T4-PA2 category of extrusions are presented in Figure 48. A similar discrepancy observed in the 63.5-T4-PA1 extrusions was encountered in this category. Once again, this discrepancy was attributed to slight inconsistencies in the temper condition of the material. This is suspected to be the reason as the discrepancy in the force response spans the whole displacement domain.

Additionally, as it will be shown later, the extrusions within the 50.8-T4-PA2 grouping did not experience the same issue. The measurements of wall thickness for the extrusion were double-checked post-test and wall thickness values were identical between the three extrusions in this category. This is further evidence that the material properties were not consistent with each other. The average force for this category was 13.32 kN. The average *TEA* and *SEA* were 2.41 kJ and 8.77 kJ/kg, respectively.

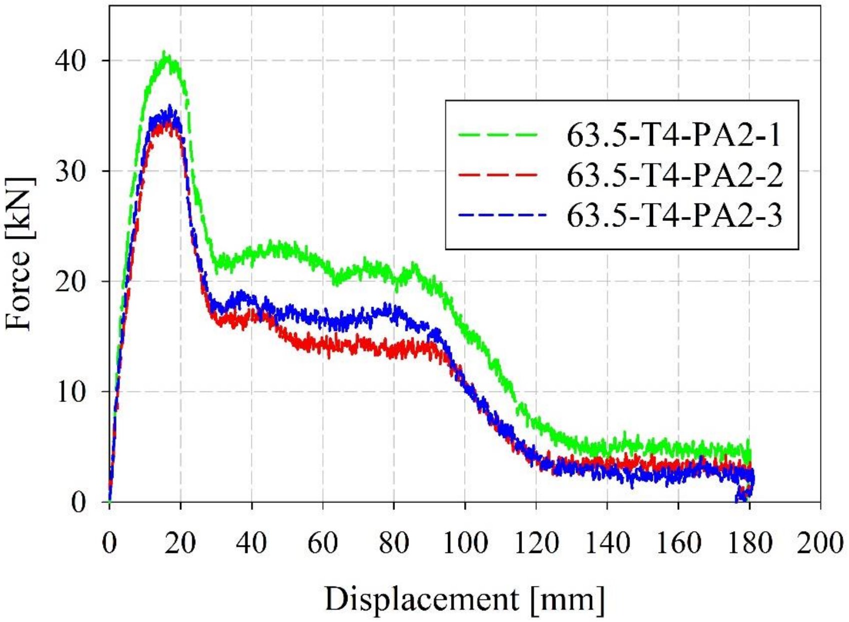

Figure 48: Force-displacement responses for the 63.5-T4-PA2 extrusions.

Force-displacement responses from specimens in the 50.8-T6-PA2 category are illustrated in Figure 49. The responses presented a high degree of accuracy and repeatability. The forces achieved and the locations of the dips and the peaks were identical between all these extrusions. More stability was observed in these extrusions compared to those in the 63.5-T6-PA1 category. This is attributed to higher consistency between measurements of wall thickness and accuracy in machining of the 50.8 mm OD extrusions. The average performance parameters for these extrusions slightly varied from their 63.5 mm OD counterparts. The average mean force was 18.13 kN. The average *TEA* was 3.05 kJ, the average *SEA* was slightly higher than the 63.5 mm OD extrusions with a value of 14.14 kJ/kg.

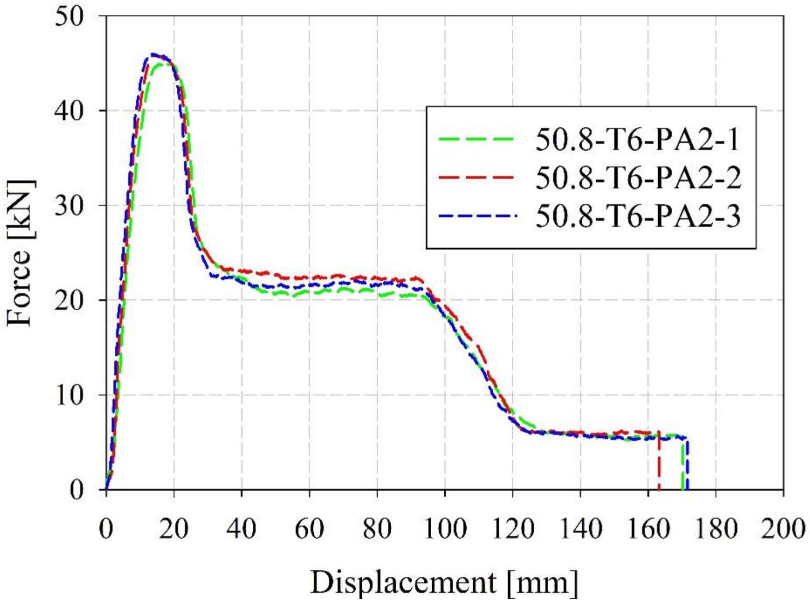

Figure 49: Force-displacement responses for the 50.8-T6-PA2 extrusions.

The 50.8-T4-PA2 category of extrusions exhibited force responses presented in Figure 50. As noted within PA1, a similar trend existed between the 63.5-T4-PA2 and 50.8-T4-PA2 extrusions, where the 63.5 mm OD extrusions present slightly more variation in force responses between tests due to variation of material properties. The stability and repeatability of the 50.8 mm OD extrusions is extremely high between tests, and this further supports the hypothesis that the material variation is the underlying cause of this prior discrepancy. The average force between the three tests was 12.75 kN. The average *TEA* and *SEA* were 2.34 kJ and 10.95 kJ/kg, respectively. These values were similar to the average performance parameters of the 63.5-T4-PA2 extrusions.

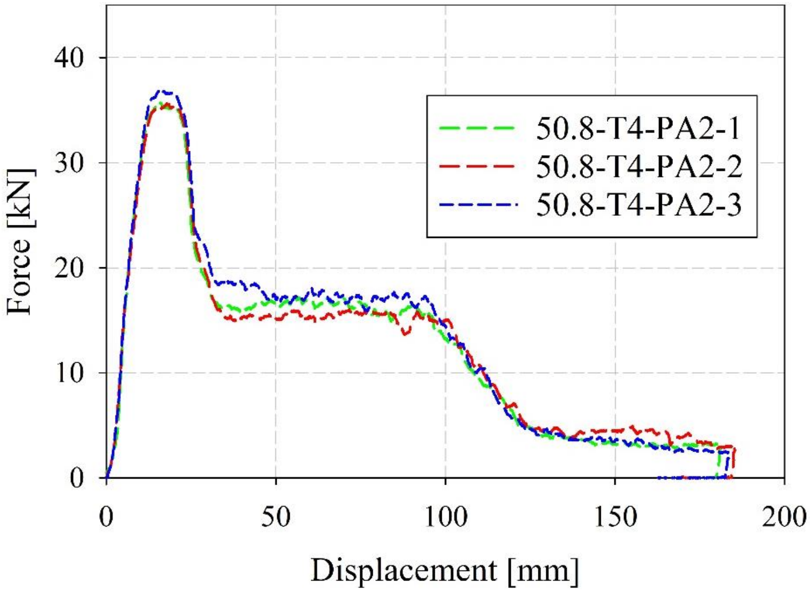

Figure 50: Force-displacement responses for the 50.8-T4-PA2 extrusions.

6.3.3: Passive Adaptivity 3

The third passive adaptive extrusion geometry selected for experimentation followed a trend which was opposite to previous two extrusions. There are three distinct force regimes within this category. The first regime consisted of a high force region, where the wall thickness was 3.175 mm, which persisted for 40 mm. This was followed by a stepped decrease in wall thickness of 1.588 mm, for approximately 80 mm. The final loading regime consisted of a step back up in thickness to a wall thickness of 3.175 mm, for the remainder of the displacement domain.

The 63.5-T6-PA3 extrusions exhibited force responses presented in Figure 51. All of the extrusions in this test category presented high repeatability and stability. The only discrepancy which exists within this category was with extrusion #3 of this category. The transition to the last, high force regime was slightly prolonged. This was due to slight variations in the machining of this extrusion. It should be noted that unlike the desired design of this extrusion, the machining process for the transitional regions of this extrusion cannot be a perfect step increase or decrease. The tool utilized for this purpose has a slight chamfer and as a result, the force response in the stepped increase regions is more of a steep, linear increase. The slight discrepancy in the machining of this extrusion provided a slightly more chamfered transition to the last regime. The average force was 34.20 kN. The average *TEA* and *SEA* were 5.82 kJ and 14.36 kJ/kg, respectively.

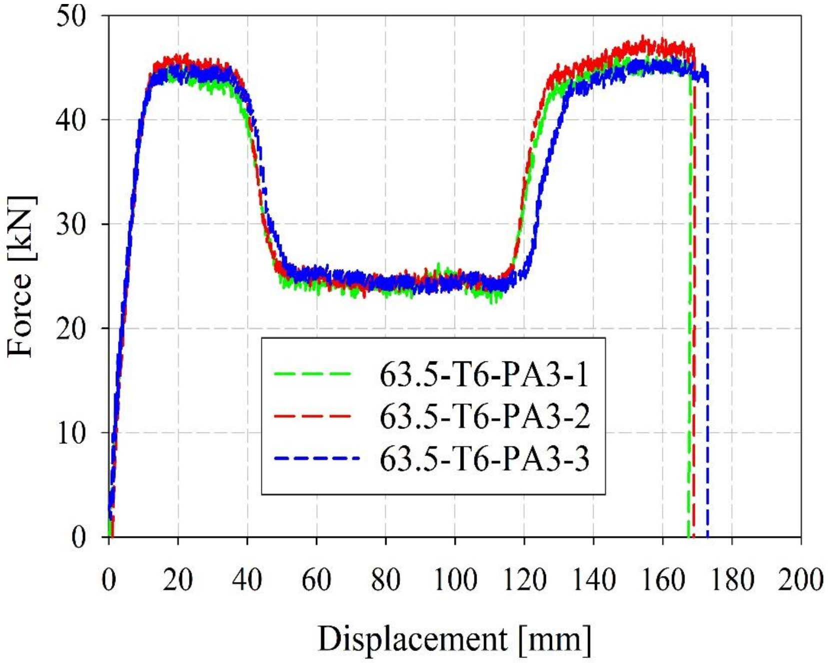

Figure 51: Force-displacement responses for the 63.5-T6-PA3 extrusions.

The force responses for specimens within the 63.5-T4-PA3 category are presented in Figure 52. Most of the force response is highly steady, however the medium force region, located near the middle of the force response varied slightly. This is similar to the force response of the 1.25 mm wall thickness extrusions. This is once again associated to the lower wall thickness, which allowed for slight twisting, which caused a slightly unsteady force in this region. This problem corrects itself when the step increase to the high force region was initiated. High repeatability and consistency were present within the force responses between the three experiments. The average force for this category was 31.40 kN. The average *TEA* and *SEA* were 5.66 kJ and 13.93, respectively.

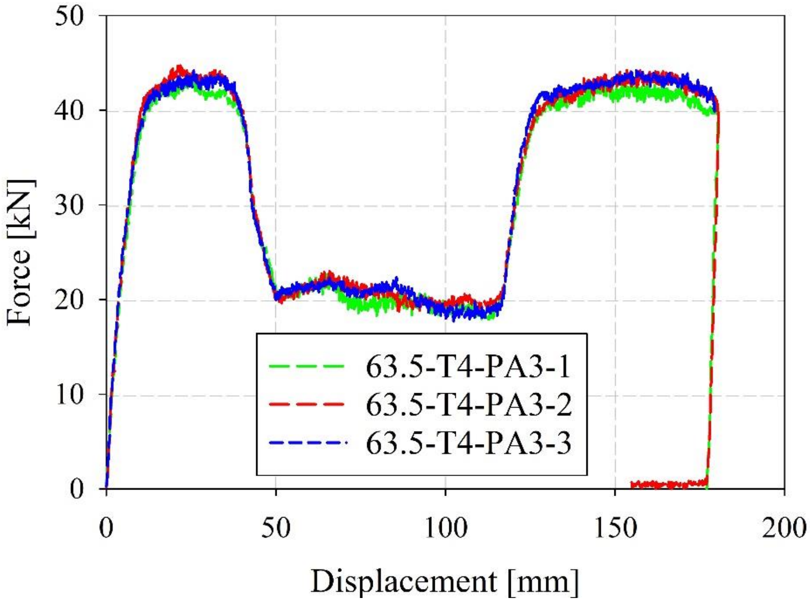

Figure 52: Force-displacement responses for the 63.5-T4-PA3 extrusions.

The 50.8-T6/T4-PA3 extrusions failed under tensile loading. The underlying reason for this was that the extrusions were machined inaccurately. The medium force region, instead of being machined to a thickness of 1.588 mm was machined down to 0.799 mm. As a result, the extrusions failed once the step increase to the higher force region was initiated. The extremely low wall thickness of the petals was unable to support the load imposed by the step increase. This led to the extrusions breaking at the low thickness cut petals. This issue was replicated within both the T6 and T4 extrusions. As a result of this failure mode, the performance parameters were not computed. An illustration of this failure is presented in Figure 53.

Figure 53: Failure at petals due to extremely thin (0.799 mm) wall thickness.

Force-displacement responses for these extrusions are presented in Figure 54. It should be noted that prior to this failure, the force responses appeared to be stable. This presents a physical limitation to this mode of deformation. Designs for application of this mode of deformation requires further analysis of the strength of the petalled sidewalls. These tests were intended to be redone, with properly machined extrusions with accurate wall thicknesses. However, due to the COVID-19 pandemic, access to the test facilities has been revoked with no indication of when it will be returned. As a result, these results were selected for presentation within this thesis.

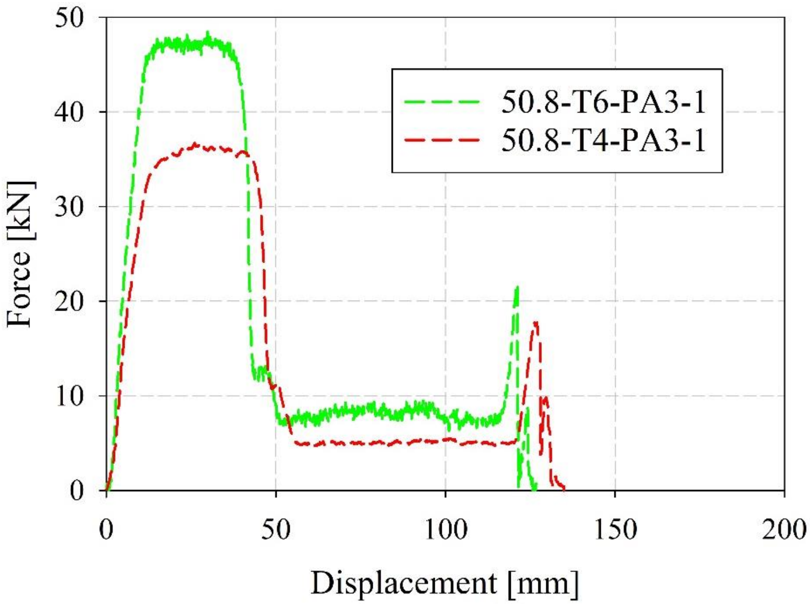

Figure 54: Force-displacement responses for the 50.8-T6/T4-PA3 extrusions.

6.4: Tensile energy absorber comparison

Energy absorbers are not usually multipurpose and are generally tailored with a specific application in mind. As a result, they are not suitable for energy absorption in other scenarios outside their scope. A good example of this can be illustrated with personal fall arrest systems (P.F.A.S.). They are designed for fall events where loads are expected to be relatively low. Because of this specific design constraint, they cannot accommodate for high force situations, or even forces which deviate slightly from their intended scope, as indicated within the literature review. Figure 55 provides a comparison of the mean forces encountered within energy absorbers in the literature and those that are considered in this study. The energy absorbers include perforated metal meshes [73], spiral reinforced concrete [74], P.F.A.S. [75], composites [76], progressive tearing [29] and bearing failure-based energy absorbers [30, 31]. The mean force was utilized as a parameter for comparison as it provided a normalized measure of energy absorption. In comparison to the remainder of the energy absorbers on this list, tensile axial cutting provides a higher range of mean forces and energy absorption.

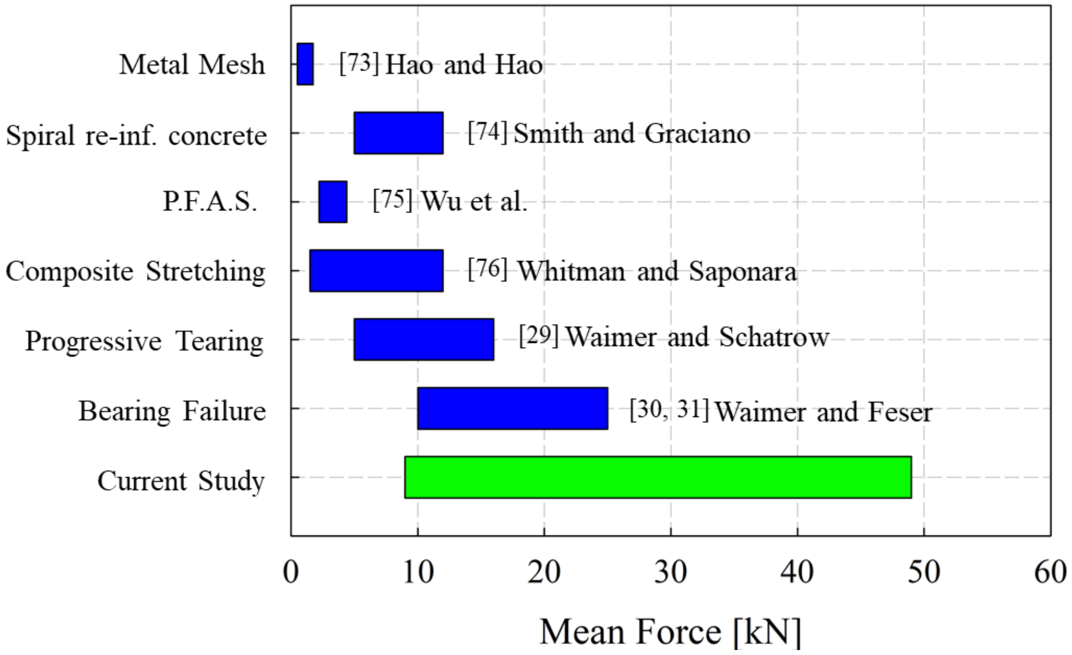

Figure 55: Comparison of tensile energy absorbers by mean force.

Chapter 7: Validation and Verification

Validation of the analytical model and the numerical model will be presented within this chapter. Additionally, the numerical model will be verified within this chapter to ensure that it follows fundamental physical laws. It has been broken into three sub-sections to address the results from the analytical model and the numerical model separately. This was done to avoid as much confusion and present the results as clearly as possible. Parameters utilized for validation of these models were the relative errors between *TEA*, *SEA*, *Pm*, *TFE* and validation metrics and cumulative errors, whose equations were presented in Chapter 5.

7.1: Analytical Model Validation

The validation of the analytical model is presented within this sub-section. As mentioned in Chapter 2, the passive adaptive geometries were designed through exploitation of the presented analytical model. Full validation of this model against experimental results is presented in Table 7 for both the 63.5 mm and 50.5 mm OD extrusions in the T6 and T4 temper. Relative errors were computed for the *TEA*, *SEA* and *Pm*. The error for the *TFE* was not computed as the validation was only completed for the passive adaptive extrusions, to verify the accuracy of the design approach outlined within Section 2.4. The average relative errors for the *SEA*, *TEA* and P_m were 2.01%, 2.01% and 3.70%, respectively. The average validation metrics and cumulative errors were 0.867 and 0.135, respectively.

Table 7: Average validation metric V_M, cumulative error, C, and relative error, R_i, between analytical predictions and experimental results.

Extrusion geometry	63.5 mm OD					50.8 mm OD				
	V_M	C	R_{TEA} [%]	R_{SEA} [%]	R_{Pm} [%]	V_M	C	R_{TEA} [%]	R_{SEA} [%]	R_{Pm} [%]
T6-PA1	0.92	0.09	0.43	0.43	1.64	0.91	0.09	2.80	2.80	0.75
T4-PA1	0.83	0.18	2.66	2.66	2.23	0.83	0.17	1.22	1.22	1.65
T6-PA2	0.87	0.12	1.25	1.25	4.15	0.87	0.13	0.23	0.23	3.17
T4-PA2	0.82	0.18	1.04	1.04	7.36	0.83	0.17	2.07	2.07	0.93
T6-PA3*	0.90	0.11	0.88	0.88	5.84	N/A	N/A	N/A	N/A	N/A
T4-PA3*	0.89	0.11	7.51	7.51	9.36	N/A	N/A	N/A	N/A	N/A

*Validation was not completed for the 50.8 mm OD extrusions in this category for the T6 and T4 tempers, the material was machined incorrectly and extrusions failed mid test.

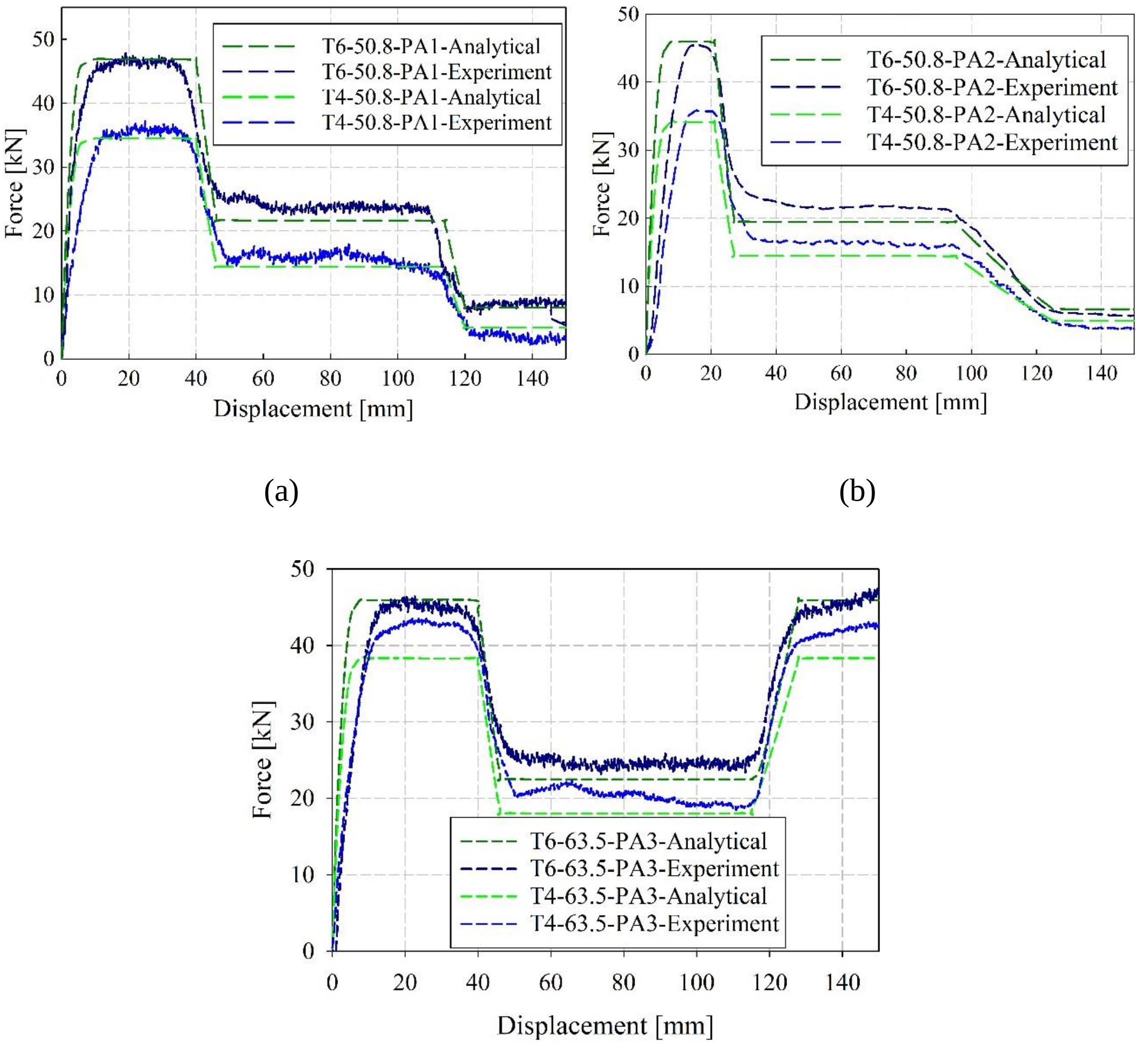

(a)

(b)

(c)

Figure 56: Conceptual, passively adaptive force-displacement responses for (a) T6/T4-50.8-PA1, (b) T6/T4-63.5-PA2, (c) T6/T4-63.5-PA3.

Figure 56 (a), (b) and (c) present the overlaid force responses for the passive adaptive extrusions PA1, PA2 and PA3, respectively. The relative errors, validation metrics and cumulative errors present high accuracy. The immediately evident observation from these force responses is that the transient region, where the force ramps up from zero to the steady state force, is slightly mis-predicted. The rationale behind this variance was that slight localized stretching occurs in the vicinity of the dowel holes, where the extrusion is anchored to the base of the test set-up. This stretching prolonged the transient regime in the experimental observations. An illustration of this stretching is shown in Figure 57.

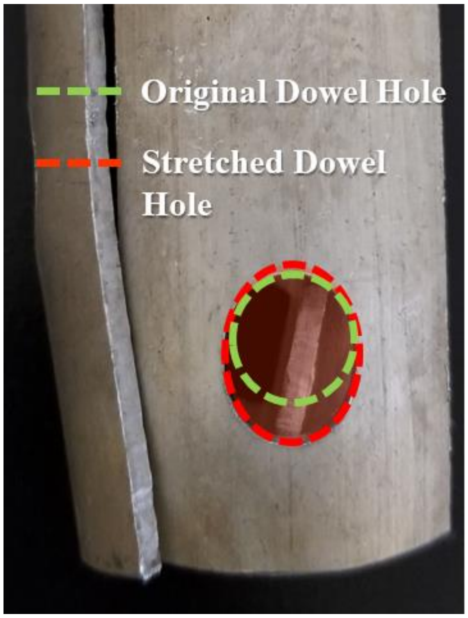

Figure 57: Stretching at the interface between the extrusion and the dowel.

The analytical model does not consider this elongation at the dowel holes, and as a result, this variation is consistent throughout the extrusions in all the categories. This explains the disparity which exists between the validation metrics, cumulative errors, and the relative error values. Generally, the overall force response is predicted with high accuracy. The steady state forces, the force transition in the stepped regions and the linearly varying regions are captured with high accuracy.

The force-displacement response for the T4-63.5-PA3 extrusions is predicted with slightly lower accuracy. These responses are presented in Figure 56 (c). All of the extrusions in the PA3 extrusion category presented forces higher than analytically predicted. The rationale behind this was covered in Section 6.3. This variation exists through the whole displacement domain and is an indication of variation in material properties as opposed to variations in wall thicknesses.

7.2: Numerical Model Validation

Numerical models were developed and simulated for the 3.175 mm and 1.588 mm wall thickness extrusions and for the PA1 passive adaptive extrusion geometries. Additionally, the force responses for the 1.25 mm extrusion category presented far too much instability in terms of lateral motion and twisting of the cutter blades along the axial length which could not be replicated within the numerical model. This provided a varied range of thick and thin-walled and passive adaptive extrusion geometries. The validation was conducted in a similar manner to the analytical model.

Before the results can be discussed, some observations need to be pointed out. The first is that the numerical modelling was only completed for the T6 counter part of the 1.588 mm wall thickness extrusions. This was done as the T4 counter parts failed at the dowel holes. Validation of these results does not add value to the prediction capabilities of the numerical model and hence were excluded. In terms of general accuracy with the experimental force-displacement responses, the numerical model presented a similar deviation within the initial transient regime, due to elongation and stretching at the dowel holes. The remainder of the displacement regime was predicted with high accuracy. Table 8 provides a summary of the relative errors between the performance parameters and validation metrics and the cumulative errors.

Table 8: Average validation metric V, cumulative errors C and relative errors R between numerical predictions and experimental results.

Extrusion profile	63.5 mm OD						50.8 mm OD					
	V_M	C	R_{TEA} [%]	R_{SEA} [%]	R_{Pm} [%]	R_{TFE} [%]	V_M	C	R_{TEA} [%]	R_{SEA} [%]	R_{Pm} [%]	R_{TFE} [%]
T6-3.175	0.95	0.05	4.69	3.01	0.69	2.63	0.92	0.10	3.41	1.24	2.19	0.41
T4-3.175	0.96	0.04	1.85	1.90	1.52	1.08	0.93	0.08	2.85	1.90	2.60	4.37
T6-1.588	0.94	0.06	2.94	4.19	4.46	0.88	0.93	0.09	1.28	0.30	1.20	2.23
T6-PA1*	0.86	0.15	2.71	3.74	1.71	N/A	0.87	0.12	4.61	3.87	4.30	N/A
T4-PA1*	0.82	0.17	3.56	2.56	1.56	N/A	0.86	0.14	3.63	4.24	5.78	N/A

* The relative error for the *TFE* values were not computed as the force response was designed to vary along the extrusion length and domain of displacement.

Figure 58 (a) and (b) present the overlaid force responses for the 3.175 mm wall thickness 63.5 mm and 50.8 mm OD extrusions, respectively. Figure 59 (a) and (b) presents the overlaid force responses for the 1.588 mm wall thickness, 63.5 mm and 50.8 mm OD extrusions, respectively. Within these extrusions, the steady state force region is predicted with high accuracy and yield average validation metrics and cumulative errors of 0.91 and

0.09, respectively. The average relative errors between the performance parameters, *TEA*, *SEA*, P_m and *TFE* were 2.91%, 2.35%, 1.99% and 1.93%, respectively.

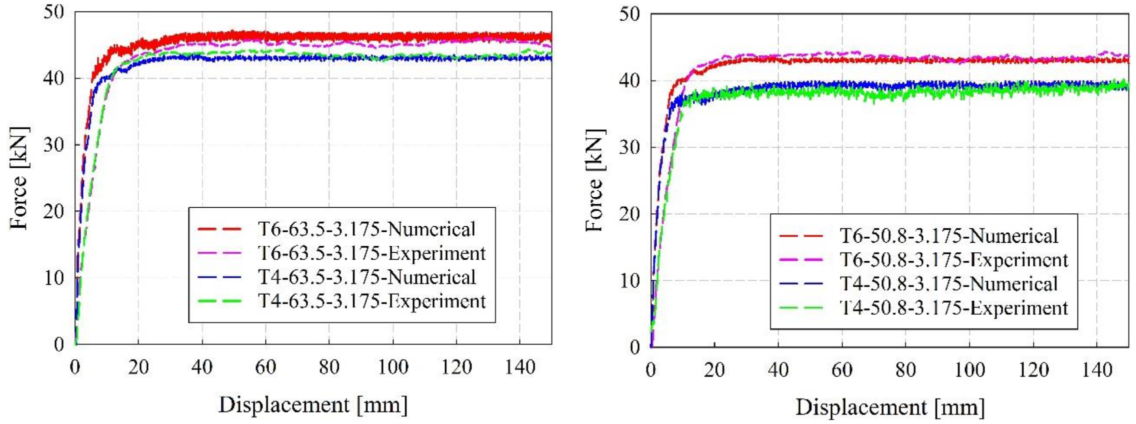

(a) (b)

Figure 58: Numerical predictions versus experimental results for a) 63.5-T6/T4-3.175, and b) 50.8-T6/T4-3.175 extrusions.

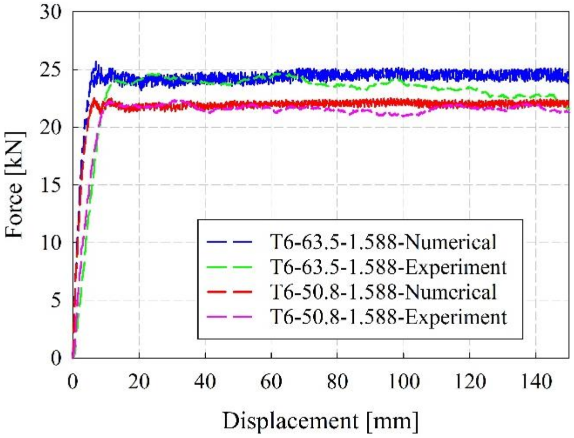

Figure 59: Numerical predictions versus experimental results for 63.5/50.8-T6-1.588 extrusions.

Figure 60 (a) and (b) presents the force responses for the PA1 extrusions of both the 63.5 mm and 50.8 mm OD extrusions, respectively. Validation was conducted on this category of extrusions to analyze the accuracy of the numerical model to the experimental observations. Additionally, comparisons can be drawn between the accuracy of the numerical and analytical predictions. Once again, as stated in the prior sub-section, the transient region is mis-predicted. However, in Figure 60 (a), the numerical prediction for the T6-63.5-PA1 extrusion predicted the transient region almost perfectly. This extrusion was verified to have minimal stretching at the dowel holes post-test. Apart from this initial discrepancy, the steady state forces and the transition loads between the stepped regions is predicted with high accuracy. For these extrusion geometries the average validation metrics and cumulative errors of 0.91 and 0.09, respectively. The average relative errors between the performance parameters, *TEA*, *SEA* and P_m were 4.12%, 4.06% and 5.04%, respectively. The relative errors were higher than the straight-sectioned extrusions as more inaccuracies were introduced as a result of the stepped thickness transitional regimes. It should be noted that the average error for the *TFE* was not calculated, the rationale behind this was that the extrusions were designed such that the forces varied through the displacement domain, so consistency through the whole displacement domain was not crucial.

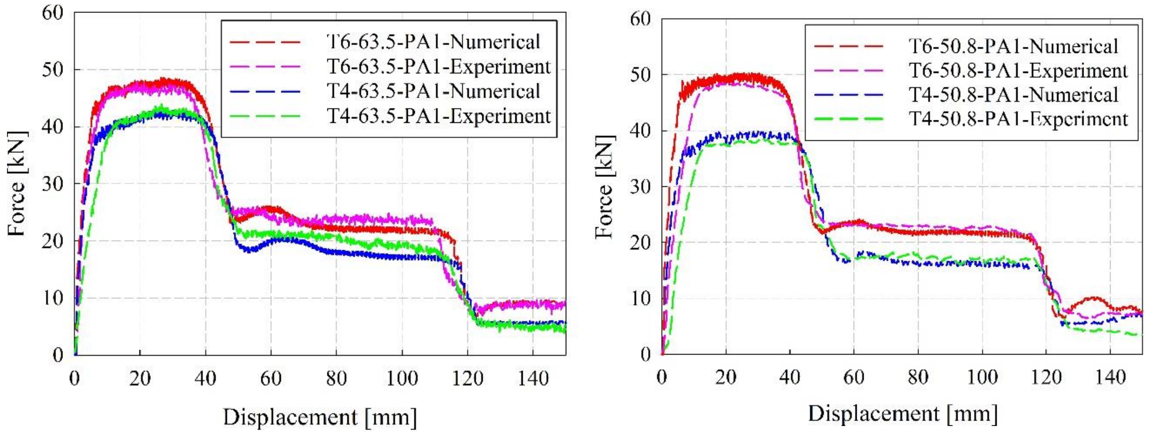

(a) (b)

Figure 60: Numerical predictions versus experimental results for a) 63.5-T6/T4-PA1 and b) 50.8-T6/T4-PA1 extrusions.

Additionally, the numerical models of the extrusion post-test were compared to the experimental extrusion post-test. The macroscopic observations between the model and the experiment were compared with each other. Primarily, the thick-walled extrusions experience a large amount of circumferential bulging. As illustrated by the prior studies and the analytical modelling, in compressive tests, the extrusions free petals tend to curl outwards. Since the petals were constrained at the dowel holes, this curling was constricted and as a result, the bulging phenomenon occurred. This problem was far more prevalent in the thick-walled 3.175 mm wall thickness extrusions and was far less evident in the lower thickness extrusions. Due to this, only the 3.175 mm wall thickness T6 and T4 extrusions were compared with the numerical models for relative error calculations. Average radius changes of 3.66 mm and 5.41 mm were measured on the experimental extrusions post-test, for the T6 and T4 extrusions, respectively. The numerical model predicted radius changes of 3.95 mm and 4.90 mm for the T6 and T4 extrusions, respectively. This resulted in relative errors of 7.92% and 9.71% for the T6 and T4 tempered extrusions, respectively. This bulging phenomenon is illustrated in Figure 61.

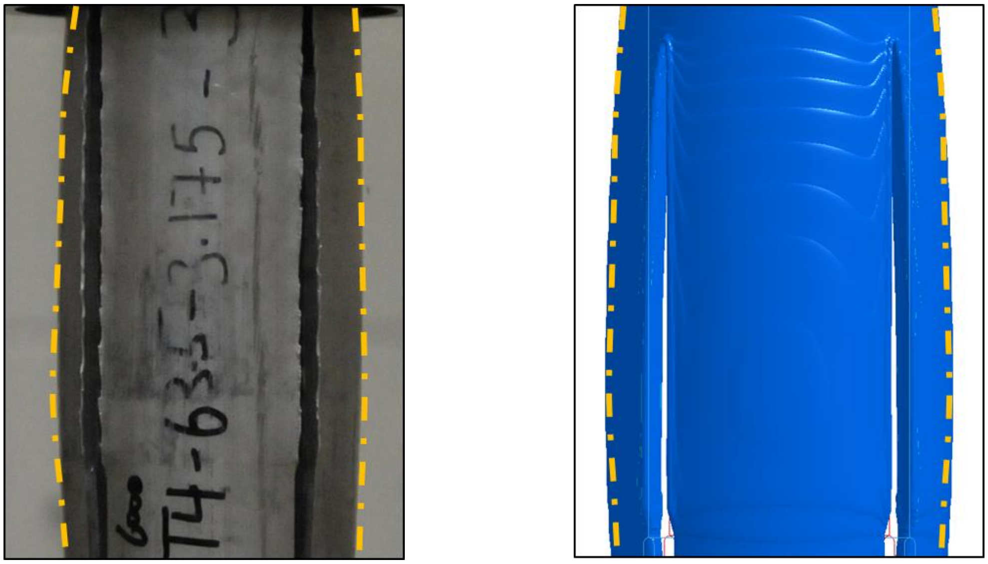

(a) (b)

Figure 61: Visualization of the deformation and radial bulging at δ = 80 mm for T4-63.5-3.175 extrusions subjected to tensile axial cutting, observed a) experimentally and b) numerically.

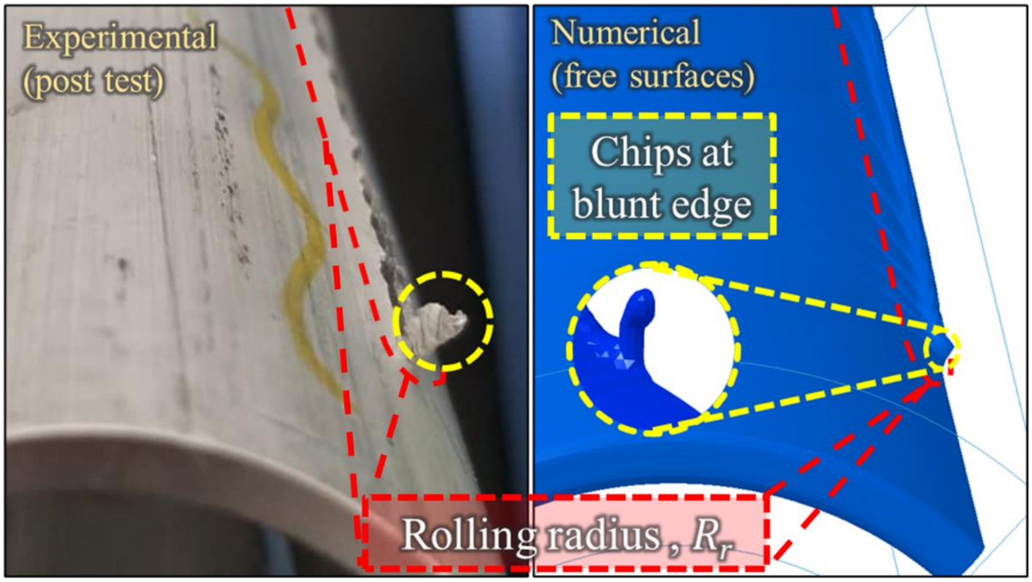

Figure 62: Visualization of the deformation of the extrusion petal for T6-63.5-3.175 extrusion ahead of the cutter blade.

The rolling radius was the second immediately visible deformation characteristic which was compared between the experimental test and numerical model. The comparison between the experimental and numerical extrusions is presented in Figure 62. The chip formation ahead of the blunt edge of the cutter blade was also captured, further illustrating the accuracy of the numerical model.

7.3: Numerical Model Verification

Verification exercises were conducted to obtain confidence in the technical merit of the finite element modeling approach. The verification was primarily achieved through quantitative examination of the energy balance of each simulation. Firstly, the principle of the conservation of energy checked within each simulation, such that the individual contributions to the overall energy within the system were equal to the external work introduced by the motion of the cutter blades. It was noted that the main contributors to the energy within the system were internal energy, due to deformation of the aluminum extrusion, and sliding energy due to contact at the extrusion/cutter interface. The kinetic energy was a minor contributor towards the internal energy balance which represented a negligible (i.e., < 2 %) amount of energy. The ratio of the force measured at the steel dowels was approximately unity in comparison to the force measured at the cutter blades, further supporting the minimal kinetic energy within the system and indicating a quasi-static simulation. In addition, Jones observed that for circular tubes, impacts at low velocities up to tens of meters of second can be considered quasi-static, therefore inertial effects can be ignored [77]. The sum of these contributors equaled the total external work over the domain of displacement with high consistency, with an average deviation of <1%. The energy balance within a representative simulation is shown in Figure 63 (a).

Additionally, the ratio of the external work with respect to the summation of the internal and sliding energy was calculated for the simulation domain with an average value of unity, indicating that energy is conserved at a high level. Furthermore, there was no significant variation through the simulation, as shown in Figure 63 (b). Another aspect of the simulation which was utilized within this verification process was the sliding energy. A decrease in the total sliding energy (referred to as negative sliding) at any point in a numerical simulation involving contact indicates inconsistencies within the model such as mesh penetrations and/or issues with the contact algorithm(s) utilized. An increasing or plateau in the sliding energy indicates stable contact with no significant penetrations between contacting surfaces. The sliding energy in the tensile axial cutting simulations presented with an increasing trend throughout the cutter's displacement, previously shown in Figure

63 (a) as the light green dashed line, further demonstrating that fundamental physical laws were adhered to and followed by the coupled Lagrangian/Eulerian approach.

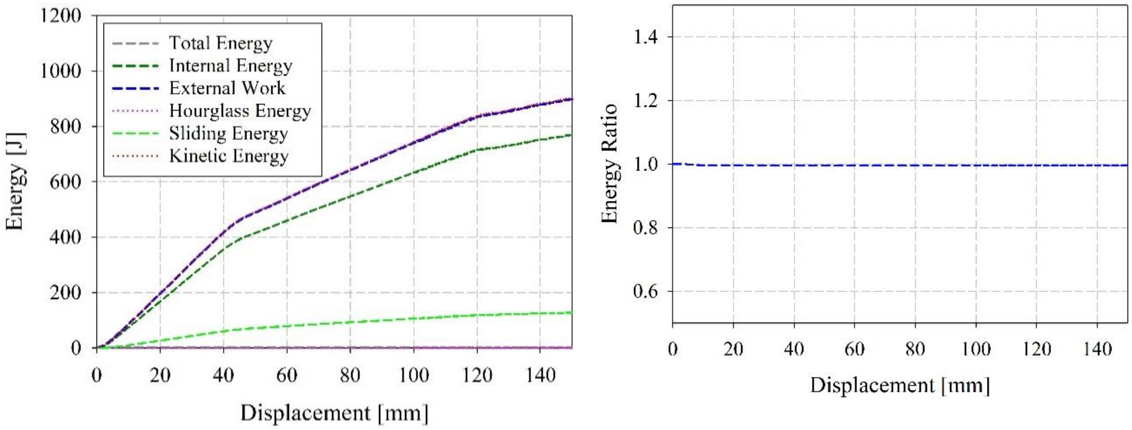

(a) (b)

Figure 63: Representative (a) energy balance within a numerical model simulating tensile axial cutting, (b) energy ratio for simulation through domain of displacement.

Chapter 8: Conclusions

The documented field of research surrounding tensile energy absorbers literature is far less concentrated than compressive energy absorbers. There are far fewer, readily available tensile energy absorbers for engineers with dependable modelling techniques. Since axial cutting was established to provide a steady and repeatable force response under compressive testing conditions, its capabilities under tensile loading conditions were tested. A parametric scope of extrusions including straight-sectioned and passively adaptive extrusions was selected. Two outer diameters and multiple wall thicknesses and thickness profiles were selected with the assistance of analytical modelling. The experimental force responses were validated against the predictions of analytical and numerical models. The main findings of the study include:

1. A total six different thickness profiles were selected across two outer diameters and material temper conditions. A total of three tests were completed in each category to test for repeatability between tests. High repeatability was observed with low variance between tests.
2. Average *TFE* values ranged from 79.25% to as high as 94.81%. The lower *TFE* was observed in the 1.25 mm wall thickness. The low extrusion thickness was determined to provide reduced stability, such that the cutter twisted about the centerline of the extrusion, during testing. This caused a consistently decreasing force response from initiation through to the end of the displacement measurements. The thicker walled extrusions generally provided much higher *TFE* and stability.

3. Average *TEA* values between 1.98 kJ to 8.46 kJ and *SEA* values ranging from 8.65kJ/kg to 17.74kJ/kg were observed between all the tested extrusions, in both temper conditions.
4. A number of physical limitations with the energy absorber structures considered in this research were observed:
    a. Primarily, the higher ductility of the 63.5/50.8-T4-1.588 category of extrusions experienced severe elongation and pin pull out failure in the vicinity of the dowel holes.
    b. The 50.8-T4-1.25 category of extrusions consisted of one experimental test which experienced pin pull out failure at the dowel holes. The remainder of the tests in this category did not experience this failure. This was attributed to slightly higher wall thicknesses in this extrusion which led to higher forces, which the dowel holes were incapable of supporting.
    c. Finally, failure was observed in the 50.8-T6/T4-PA3 extrusions. The medium force region was machined down to 0.799 mm wall thickness, as opposed to the designed specification of 1.588 mm and as a result, when the force ramped up at the last stepped thickness transitional region, the petals within the 0.799 mm thickness region were incapable of supporting this force increase. The failure occurred due to the petals breaking.
5. The axial cutting deformation mode was augmented to accommodate tensile loading conditions. Experiments were conducted with a broad parametric scope considering AA6061 extrusions with multiple temper conditions, diameters and wall thickness profiles.

6. The analytical modelling approach previously utilized for full force-displacement response prediction was exploited as a design tool to develop three passive adaptive geometries prior to experimentation. Regions of steeped thickness changes and linearly varying thickness regimes were identified to illustrate the ability to reverse engineer extrusions geometry based on analytical force responses.
7. The average validation metrics and cumulative errors for the PA1, PA2 and PA3 extrusions were 0.87 and 0.13, 0.85 and 0.15 and 0.90 and 0.11, respectively. The average relative errors between *TEA*, *SEA* and P_m for the PA1, PA2 and PA3 extrusions were 1.71%, 2.07% and 5.33%, respectively.
8. Numerical modelling was completed on LS-DYNA® for two straight-sectioned extrusions and one passively adaptive extrusion to provide prediction capabilities for both sub-sets of categories. Average validation metrics and cumulative errors between all these numerical models and experimental observations were 0.91 and 0.09, respectively, indicating high accuracy in the model's prediction capabilities. The average relative errors between all the tested extrusions were approximately 3.02%. Additionally, macroscopically visible deformation characteristics such as the rolling radius and bulging of the extrusion circumferentially were captured with high accuracy, within 10%.

Chapter 9: Future Works

The current study provides design concepts for a tensile energy absorber utilizing the axial mode of deformation. The current test set-up enables 4-bladed, quasi-static cutting. The current design requires that dowel holes be utilized and that slots be machined so that the cutter blades can be fit into the extrusion. The slots are machined from one end of the extrusion inwards until the appropriate axial length. The cutter design which includes an inner hub and outer ring, and the inclusion of the current anchoring set-up requires that the slots be machined to lengths of approximately 110 mm. This length of the extrusion cannot be utilized for the cutting deformation. Future research opportunities to explore tensile cutting in further detail can be pursued by any of the following steps:

1. Higher bladed cutting with the current test set-up is not possible as the approach of creating slots and holes on the extremity of the extrusion. This leads to a minimal amount of material on the periphery of the dowel holes and these holes are incapable of withstanding the high stresses which will be experienced in these regions. Some possible solutions to this require the redesign of the cutting tool and support device.
2. The redesign of the cutter blade can include a number of changes:
    a. A centrally expanding inner hub which contains the cutter blades. As the inner hub radially expands, the blades also move out radially. The cutter blades will eventually reach the inside wall of the extrusion and require piercing through the extrusion wall. The cutter blades will require a redesign and need a sharp edge which can pierce through the extrusions wall.

    b. Alternatively, instead of a radially expanding inner hub, an external ring that radially contracts can be implemented, and the contraction of this external ring will cause the cutter blades to move inwards and pierce through the extrusion wall. Similarly, the cutter blade profile will require a sharp edge which can pierce through the extrusion wall.
    c. An alternative to piercing can include the machining of slots in the vicinity of the penetration region of the cutter blades. The blades can radially expand or contract through the cut slots and would not be required to pierce through.
3. The solutions proposed above all rely solely on a cutter redesign if a redesign of the entire extrusion anchoring mechanism can be modified in addition to just changing the cutter blade design.
    a. The idea proposed in 2c. of the previous suggestion can be utilized to provide both an axial cutting mode of deformation and an anchoring mechanism. This requires the use of two cutting tools. One cutting tool would be attached to the moving hydraulic arm, while the other cutter would be constricted to the base of the tensile cutter set-up.
    b. The blades of the cutting tool can be positioned within slots machined around the midspan of the extrusion. The two cutters will be placed on opposite ends of each other, facing away from each other. The cutter facing towards the top of the set-up will be attached to the hydraulic arm and initiate cutting, whereas the bottom cutter will act as the anchoring mechanism.

c. The motion of the hydraulic arm, and subsequently the cutter attached to this arm triggers a cutting deformation mode. The reaction force caused by the initiation of the cutting, combined with the second set of cutters anchoring the extrusion to the base initiates cutting at this bottom set of cutters.

d. This leads to a two-way cutting process to occur in a truly tensile mode of deformation, where the cutting process initiates from the middle of the extrusion. Additionally, the limiting factor for the number maximum number of blades which can be utilized in this process will be the strength of the cut petals. An schematic of this process is shown in Figure 64.

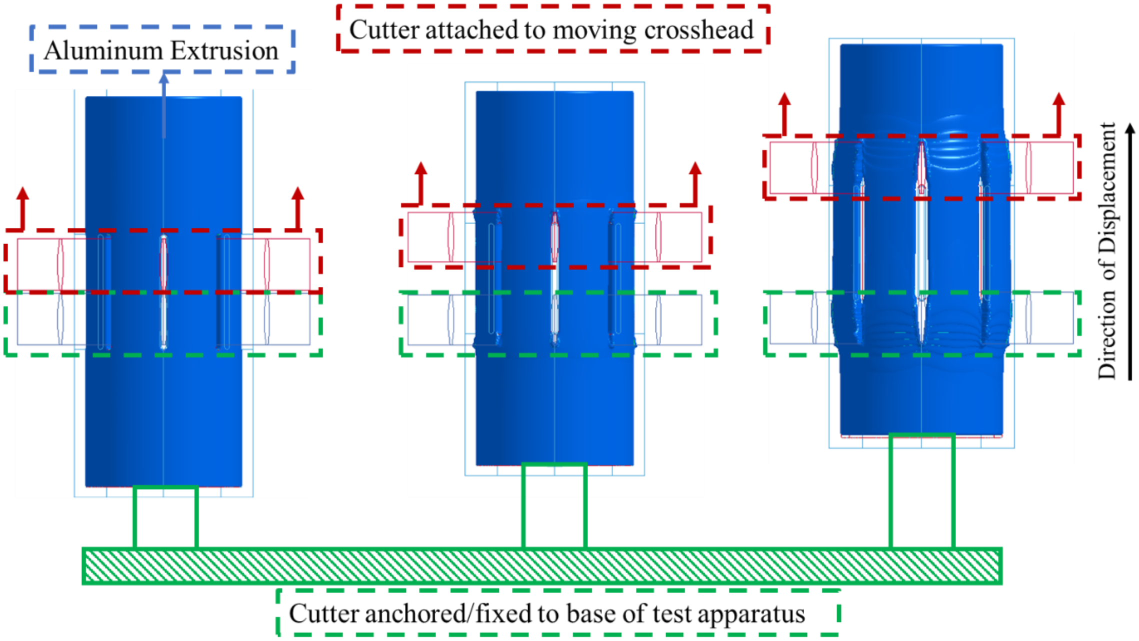

Figure 64: Concept for two-direction cutting process.

4. Finally, an alternative to cutting can be surface gouging, where either a tight fitting outer or inner ring with short blades will gouge the surface of the extrusion, rather than fully cut through the petals.
5. All of these proposed ideas will require new analytical modelling which can be developed from the currently existing analytical models.

References

[1] W. H. O. "Global status report on road safety 2018," WHO, Geneva, 2018.

[2] N. Jones, "Dynamic progressive buckling in structural impact," in *Structural Impact,* Cambridge, Cambridge University Press, 2003, pp. 385-388.

[3] S. Chung Kim Yuen and G. Nurick, "The energy-absorbing characteristics of tubular structures with geometric and material modifications: An overview," *Applied Mechanics Reviews*, vol. 61, no. 1-6, pp. 0208021-02080215, 2008.

[4] A. Baroutaji, M. Sajjia and A. Olabi, "On the crashworthiness performance of thin-walled energy absorbers: Recent advances and future developments," *Thin-Walled Structures,* vol. 118, pp. 137 - 163, 2017.

[5] J. Magliaro, W. Altenhof and A. Gudisey, "Analytical and experimental investigations of the enhanced mechanical response of cutting deformation compared to progressive folding in AA6061 energy dissipation devices," *International Journal of Mechanical Sciences,* vol. 158, pp. 808-827, 2019.

[6] J. Magliaro, A. Shakib, A. Gudisey and W. Altenhof , "Evolution of energy dissipation mechanisms over a comprehensive range of cutting modes and enchanced capabilties under hybrid cutting/clamping in AA6061 extrusions," *Thin-Walled Structures*, 2020.

[7] A. Majumder, W. Altenhof, S. Jin, T. Kapoor and D. Green, "Simulation of the Axial Cutting Deformation of AA6061-T6 Round Tubes Utilizing Eulerian and Mesh Free Finite Element Formulations," *SAE International Journal of Materials and Manufacturing*, vol. 1, no. 1, pp. 525-536, 2009.

[8] J. Magliaro and W. Altenhof, "A Comparison of the Mechanical Performance of AA6061-T6 Extrusions Subjected to Axial Crushing and Axial Cutting," in *Society of Automotive Engineers*, Detroit, 2019.

[9] S. Jin, W. Altenhof and Z. Li, "A Parametric Study on Extrusion Geometry and Blade Quanitity During Axial Cutting deformation of Circular AA6061-T6 Extrusions under Impact and Quasi-Static Loading," *International Journal of Impact Engineering*, vol. 49, pp. 165-178, 2012.

[10] M. Lohman, A. Sonnega, E. Nicklett, L. Estenson and A. Leggett, "Comparing estimates of fall-related mortality incidence among older adults in the United States," *The Journals of Gerontology: Series A*, vol. 74, no. 9, pp. 1468- 1474, 2019.

[11] H. Crawford, Survivable Impact Forces on Human Body, Glasgow: Crown, 2003.

[12] H. Cecen and B. Sertyesilisik, "A Fall Protection System for High-Rise Construction," *Journal of Engineering*, vol. 2013, 2013.

[13] H. Hsiao, "Evaluation of Fall Arrest Harness Sizing Schemes," *Human Factors*, pp. 447-464, 2007.

[14] S. Choi, L. Guo, J. Kim and S. Xiong, "Comparison of fatal occupational injuries in construction industry in the United States, South Korea, and China," *International Journal of Industrial Ergonomics,* vol. 71, pp. 64- 74, 2019.

[15] H. Hsai, N. Turner, R. Whisler and J. Zweiner, "Impact of harness fit on suspension tolerance," *Human Factors,* vol. 54, no. 3, pp. 346-357, 2013.

[16] Y. Goh and P. Love, "Adequacy of personal fall arrest energy absorbers in relation to heacy workers," *Safety Science,* vol. 48, pp. 747-754, 2010.

[17] M. Bambach, R. Mitchell and R. Grzbiela, "Evaluation of Fall Arrest Harness Sizing Schemes," *Traffic Injury Prevention* , vol. 14, pp. 756-765, 2013.

[18] L. Robinson, "Factors affecting the strength of safety harness and lanyard materials - combination of effects, Buxton," *UK Health and Safety Laboratory,* 2007.

[19] T.-L. Teng, P. Chang, C.-C. Liang and D.-A. Fung, "Application of crash pulse on the carcrashworthiness design," *Advances in Material Engineering,* vol. 9, no. 9, pp. 1-8, 2017.

[20] M. A. Basith, C. N. Reddy, S. Uppalapati and S. Jani, "Crash analysis of a passenger car bumper assembly to improve design for impact test," *Materials Today: Proceedings,* 2020.

[21] M. Fernandez, L. Garcia-Escudero and A. Molinero, "Analysis of real crashes against metal roadside barriers," *Plos One*, 2019.

[22] R. Retting, S. Ferguson and A. McCartt, "A review of evidence-based traffic engineering measures designed to reduce pedestrian-motor vehicle crashes," *AM J Public Health,* vol. 93, no. 9, pp. 1456-1463, 2003.

[23] S. Lai, "Roadside and Median Barrier Systems," Alberta Infrasctructure and Transportation, 2009.

[24] A. Linder, "Acceleration Pulses And Crash Severity In Low Velocity Rear Impacts – Real World Data and Barrier Tests," Chalmers University of Technology, Goteborg, 2001.

[25] T. Jiang, R. Grzebieta and X. Zhao, "Predicting impact loads of a car crashing into a concrete roadside safety barrier," *Internation Journal of Crashworthiness,* vol. 9, pp. 45-63, 2004.

[26] N. Li, B. Park and J. Lambert, "Effect of guardrail on reducing fatal and severe injuries on freeways: Real-world crash data analysis and performance assessment," *Journal of Transportation Safety and Security,* vol. 10, no. 5, pp. 455-470, 2018.

[27] A. Molan, M. Rezapur and K. Khaled, "Modeling traffic barriers crash severity by considering the effect," *Journal of Modern Transportation,* vol. 27, no. 2, pp. 141-151, 2019.

[28] S. Heimbs and T. Bergmann, "Bearing Mode Absorber-On the absorption capability of pulling a bolt through a composite or sandwich plate," *International Symposium*

on Dynamic Response and Failure of Composite Materials, vol. 88, pp. 146-156, 2014.

[29] M. Waimer, P. Schatrow, T. Feser, H. Kraft and D. Kohlgruber, "Development of a Tension Energy Absorber - Progressive Bearing Failure Mechanisms of Composite Bolted Joints," German Aerospace Center (DLR), Cologne, 2016.

[30] M. Waimer, T. Feser, P. Schatrow and D. Schueler, "Crash Concepts for CFRP Transport Aircraft-Comparsion of the Tranditional Bend Frame Concept versus the Developments ina Tension Absorber Concept," *International Journal of Crashworthiness,* vol. 23, no. 2, pp. 193-218, 2017.

[31] M. Waimer, T. Feser and J. Hassan, "Effects of transient dynamic loading on the energy absorption capability of composite bolted joints undergoing extended bearing failure," *Composite Structures,* vol. 247, 2020.

[32] S. Heimbs, S. Schmeer, J. Blaurock and S. Steeger, "Static and dynamic failure behaviour of bolted joints in carbon fibre composites," *Composites: Part A,* vol. 47, pp. 91-101, 2013.

[33] C. Stocchi, P. Robinson and S. Pinho, "A detailed finite element investigation of composite bolted joints with countersunk fasteners," *Composites: Part A,* vol. 52, pp. 143-150, 2013.

[34] G. Di Franco and B. Zuccarello, "Analysis and optimization of hybrid double lap aluminum-GFRP joints," *Composite Structures,* vol. 116, pp. 682-693, 2014.

[35] T. Reddy and S. Reid, "Axial Splitting of Circular Metal Tubes," *International Journal of Mechanical Sciences,* vol. 28, no. 2, pp. 111-131, 1986.

[36] X. Huang, G. Lu and T. Yu, "On the axial splitting an dcurling of circular metal tubes," *International Journal of Mechanical Sciences,* vol. 44, pp. 2369-2391, 2002.

[37] L. Dai, Y. Pan and A. Wang, "Study of the energy absorption performance of an axial splitting componentfor anchor bolts under static loading," *Tunnelling and Underground Space Technology,* vol. 81, pp. 176-186, 2018.

[38] L. Dai, Y. Xiao, Y. Pan, A. Wang, C. Fan and J. Guo, "Mechanical behavior and factors influencing axial splitting energy absorbers and optimized application for rock bolts," *Tunnelling and Underground Space Technology,* vol. 102, 2020.

[39] S. Hassani, in *Proceedings of the Fifteenth International Machine Tool Design and Research Conference,* 1975.

[40] E. Chirwa, "Theoretical analysis of tapered thin-walled metal inverbucktube," *International Journal of Mechanical Sciences,* vol. 35, no. 3-4, pp. 325-351, 1993.

[41] A. Kinkead, "Analysis for inversion load and energy absorption of a circular tube," *The Journal of Strain Analysis for Engineering Design,* vol. 18, no. 3, 1983.

[42] S. Y. Jin and W. Altenhof, "An analytical model on the steady-state deformation of circular tubes under an axial cutting deformation mode," *International Journal of Solids and Structures,* vol. 48, pp. 269-279, 2011.

[43] S. Jin and W. Altenhof, "Mechanical Performance of Circular AA6061-T6 Extrusions Under Axial Cutting Deformation," in *SAE*, Detroit, 2011.

[44] S. Jin, A. Majumder, W. Altenhof and D. Green, "Axial cutting of AA6061-T6 circular extrusions under impact using single and dual-cutter configurations," *International Journal of Impact Engineering*, vol. 37, pp. 735-753, 2010.

[45] A. Majumder, W. Altenhof, V. Vijayan and S. Jin, "Quasi-static axial cutting of AA6061-T4 and T6 round extrusions," *Proceedings of the Institution of Mechanical Engineering Part L: Journal of Materials: Design and Applications*, vol. 222, pp. 183-195, 2008.

[46] S. Jin and W. Altenhof , "Control of Load/Displacement Responses of AA6061 T6 and T4 Circular Extrusions under Axial Compressive Loads," *International Journal of Impact Engineering*, vol. 38, pp. 1-15, 2011.

[47] G. Lu and C. Calladine, "On the cutting of a plate by a wedge," *International Journal of Mechanical Sciences,* vol. 32, no. 4, pp. 293-313, 1990.

[48] J. Paik, "Cutting of a Longitudinally Stiffened Plate by a Wedge," *The Society of Naval Architects and Marine Engineers,* vol. 38, no. 04, 1994.

[49] H. Vaughan, "Bending and tearing of plate and application to ship botton damage," *Nav. Architect*, vol. 3, pp. 97-99, 1978.

[50] T. Simonsen and Wierzbicki, "Plasticity, fracture and friction in steady-state plate cutting," *International Journal of Impact Engineering,* vol. 21, no. 5, pp. 387-411, 1998.

[51] B. C. Simonsen, R. Tornqvist and M. Lutzen, "A simplified grounding damage prediction method and its application in modern damage stability requirements," *Marine Structures,* vol. 22, no. 1, pp. 62-83, 2009.

[52] T. Wierzbicki and P. Thomas, "Closed-form solution for wedge cutting force through thin metal sheets," *International Journal of Mechanical Sciences,* vol. 35, no. 3/4, pp. 209 - 229, 1993.

[53] T. Wierzbicki, "Concertina tearing of metal plates," *International Journal of Solids and Structures,* vol. 32, no. 19, pp. 2923-2943, 1995.

[54] J. Magliaro and W. Altenhof, "Mechanical performance and crashworthiness of plates and extrusions subjected to cutting: An overview," *Thin-Walled Structures,* vol. 148, p. 106612, 2020.

[55] J. Magliaro and W. Altenhof, "Energy absorption mechanisms and capabilities for magnesium extrusions under impact," *International Journal of Mechanical Sciences,* vol. 179, no. 1, p. 105667, 2020.

[56] I. Boldyrev, "EFG-simulation of the free orthogonal cutting and cutting forces prediction," *Procedia Engineering,* vol. 206, pp. 1201-1204, 2017.

[57] J. Magliaro and W. Altenhof, "A Comparison of the Mechanical Performance of AA6061-T6 Extrusions Subjected to Axial Crushing and Axial Cutting," in *SAE*, Detroit, 2020.

[58] J. Magliaro and W. Altenhof, "Analytical predictions of the complete mechanical response of AA6061 energy absorbers subjected to axial cutting," *Thin Walled Structures,* vol. 139, pp. 151-168, 2019.

[59] J. Zhang and T. Alpas, "Transition between mild and severe wear in aluminum alloys," *Acta Materialia,* vol. 45, no. 2, pp. 513-528, 1997.

[60] "ASTM B918 / B918M-17a, Standard practice for heat treatment of wrought aluminium alloys," in *Annual Book of ASTM Standards*, West Conshohocken, ASTM International, 2017.

[61] E. J. Hatch, "Microstructure of Alloys," in *Aluminum Properties and Physical Metallurgy*, ASM International, 1984, pp. 58-104.

[62] M. G. Nowotnik, "Influence of chemical composition variation and heat treatment on microstructure and mechanical properties of 6xxx alloys," *Archives of Materials Science and Engineering,* vol. 46, no. 2, pp. 98-107, 2010.

[63] J. Ridhwan, J. A. Noor, M. S. Zakaria, Z. Zulfuttah and M. H. Hafidzal, "Effect of Heat Treatment on Microstructure and Mechanical Properties of 6061 Aluminum Alloys," *Journal of Engineering and Technology,* vol. 5, no. 1, 2014.

[64] R. Nunes, "Volume 2 Properties and Selection: Nonferrous Alloys and Special-Purpose Materials," in *ASM Handbook*, ASM International, 1190, p. 115.

[65] M. Glogovsky, M. Fujda, M. Vojtko and P. Zubko, "Effect of Heat Treatment on Microstructure and Mechanical Properties of Extruded SiC/6061 Composite," *Acta Metallurgica Slovaca*, vol. 21, no. 1, pp. 35-43, 2015.

[66] W. Abramowicz and T. Wierzbicki , "Axial crushing of foam filled columns," *International Journal of Mechanical Sciences*, vol. 30, no. 3 - 4, pp. 263 - 271, 1988.

[67] J. Strenkowski and S. Athavale, "A partially constrained Eulerian orthogonal cutting model for chip control tools," *Journal of Manufacturing Science and Engineering*, vol. 119, pp. 681- 688, 1997.

[68] K. Amini, W. Altenhof, S. Yuen, C. Opperman and G. Nurick, "Experimental and numerical investigation on the deformation and energy dissipation of AA6061-T6 circular extrusion subjected to blast loading," *International Journal of Impact Engineering*, vol. 110, pp. 228 - 241, 2017.

[69] A. Raczy, M. Elmadagli, W. Altenhof and A. Alpas, "An Eulerian Finite-Element Model for Determinationof Deformation State of a Copper Subjected to Orthogonal Cutting," *Metallurgical and Materials Transactions A*, vol. 35, pp. 2393-2400, 2004.

[70] J. Reid and N. Hiser, "Friction modelling between solid elements," *International Journal of Crashworthiness*, vol. 9, no. 1, pp. 65-72, 2010.

[71] X. Wang, Y. Xu and R. L. Jackson, "Theoretical and finite element analysis of static friction between multi-scale rough surfaces," *Tribology Letters,* vol. 66, no. 148, 2018.

[72] W. Oberkampf and T. Trucano, "Verification and validation in computational fluid dynamics," *Progress in Aerospace Sciences,* vol. 38, no. 3, pp. 209-272, 2002.

[73] Y. Hao and H. Hao, "Mechanical properties and behaviour of concrete reinforced with spiral-shaped steel fibres under dynamic splitting tension," *Magazine of Concrete Research,* vol. 68, no. 21, pp. 1110-1121, 2016.

[74] D. Smith, C. Graciano and G. Aparicio, "Energy absorption capacity of expanded metal meshes subjected to tensile loading," *Redin,* no. 77, 2015.

[75] J. Wu, J. Power, J. Harris and C. Pan , "Estimation of the kinetic energy dissipation in fall arrest system and manikin during fall impact," *Ergonomics,* vol. 54, no. 4, pp. 367-379, 2010.

[76] Z. Whitman and V. Saponara, "Bistable structures for energy absorption, II: Composite structures under tension," *Journal of Mechanics of Materials and Structures,* vol. 2, no. 2, pp. 359-375, 2007.

[77] N. Jones, Structural Impact, Cambridge: Cambridge University Press, 1989.

[78] W. Abramowicz and N. Jones , "Dynamic progressive buckling of circular and square tubes," *International Journal of Impact Engineering,* vol. 4, no. 4, pp. 243-270, 1986.

Appendix

Appendix A: Extrusion Geometries

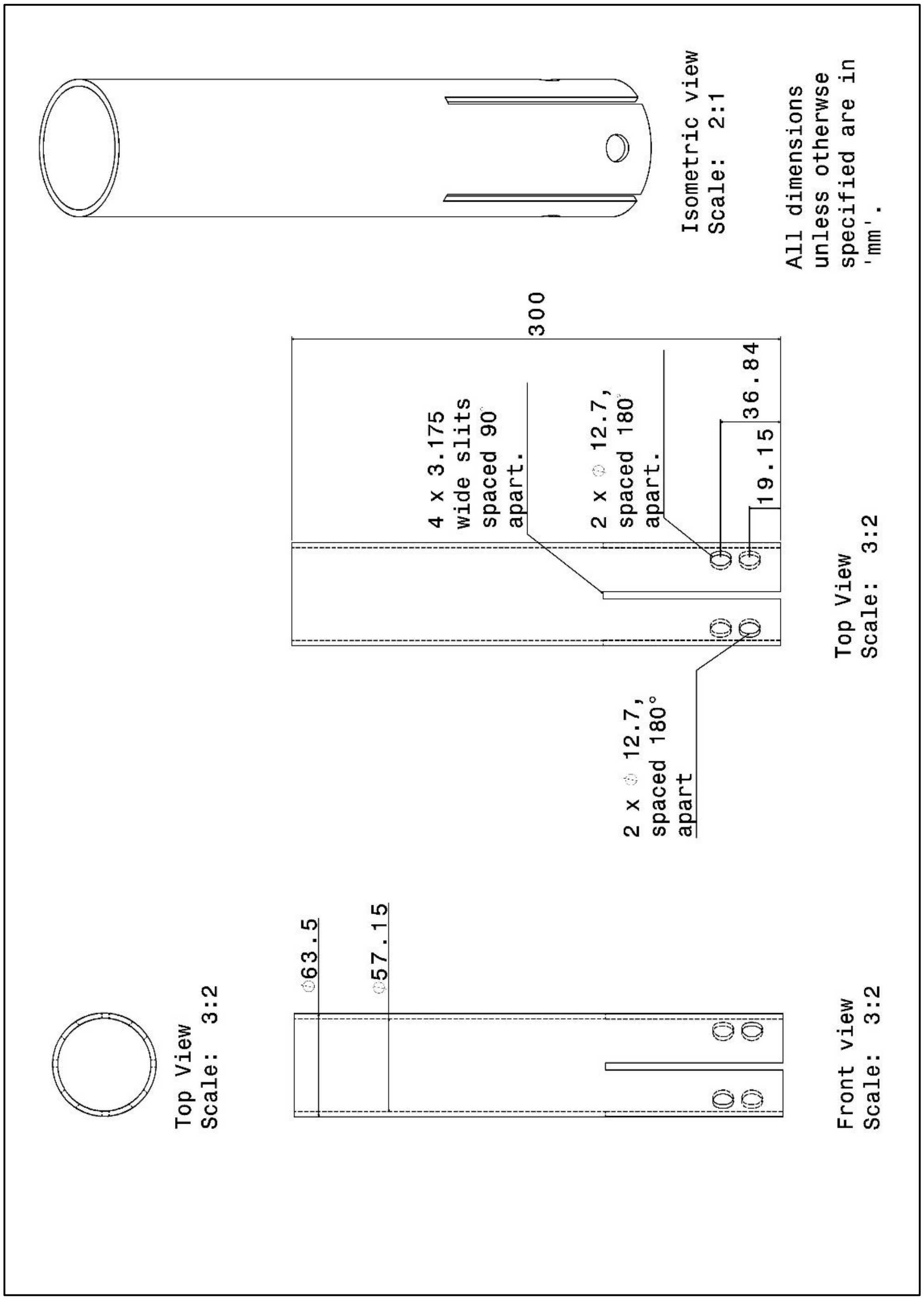

Figure 65: CAD schematic of 3.175 mm extrusion.

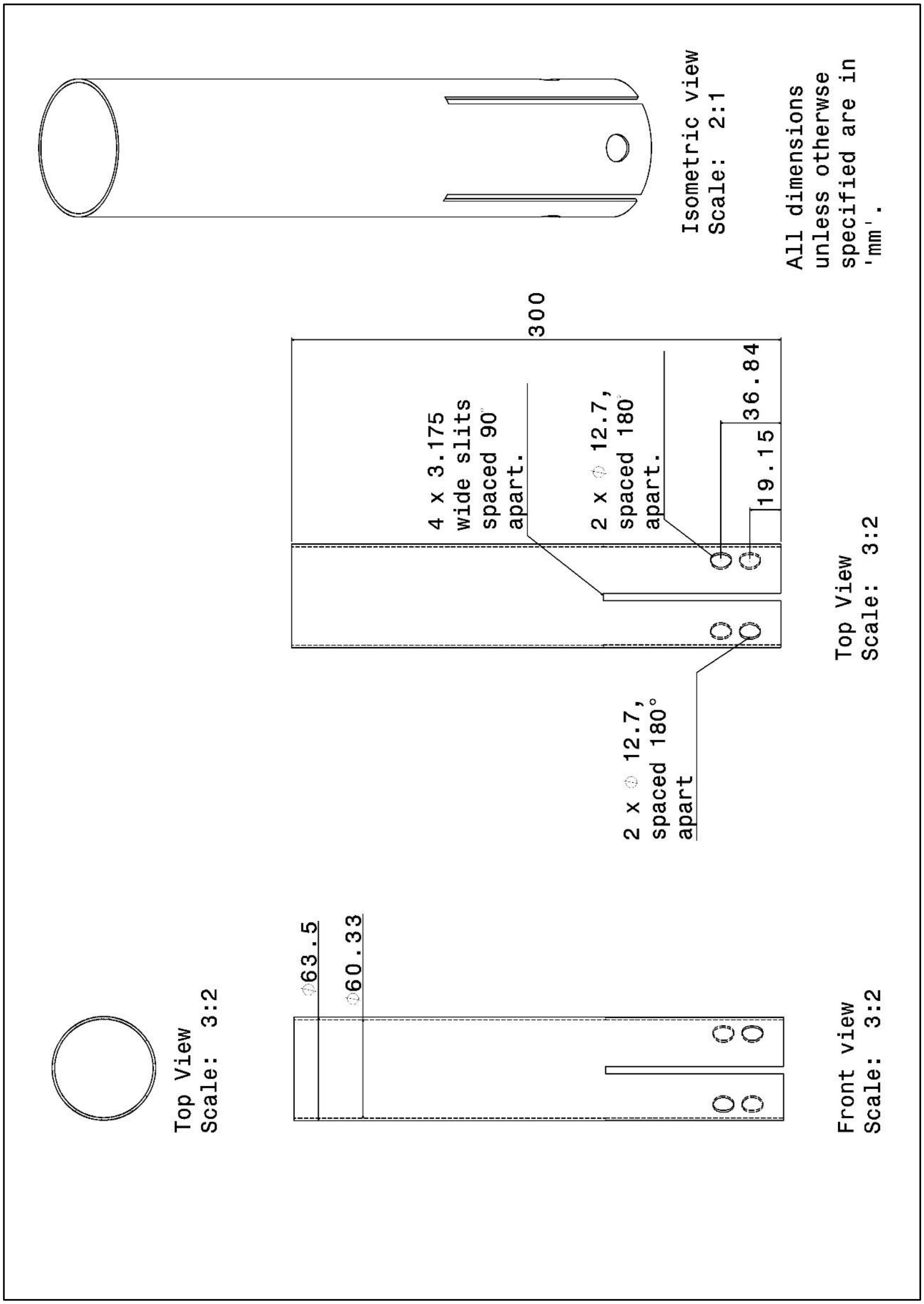

Figure 66: CAD schematic of 1.588 mm extrusion.

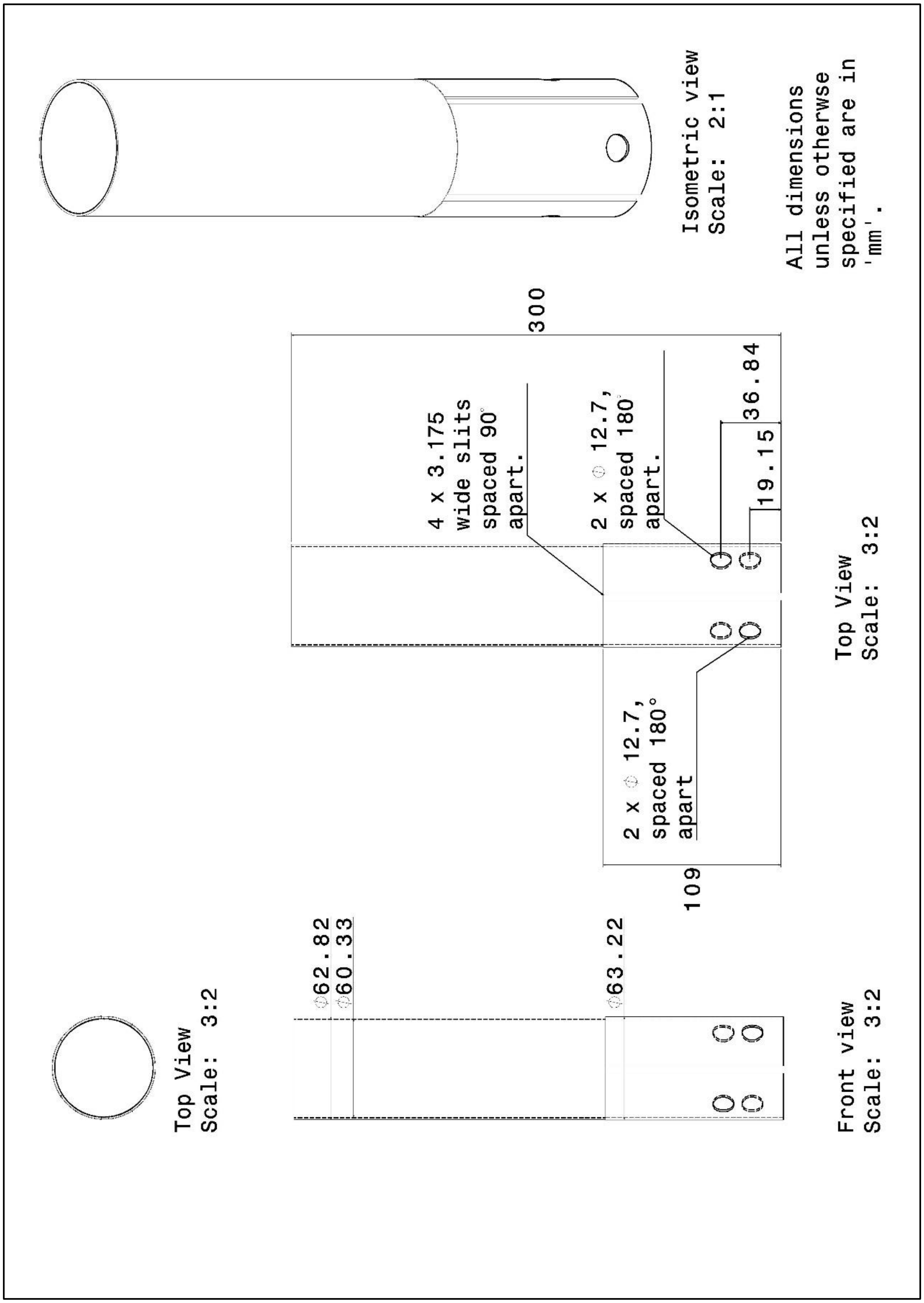

Figure 67: CAD schematic of 1.25 mm extrusion.

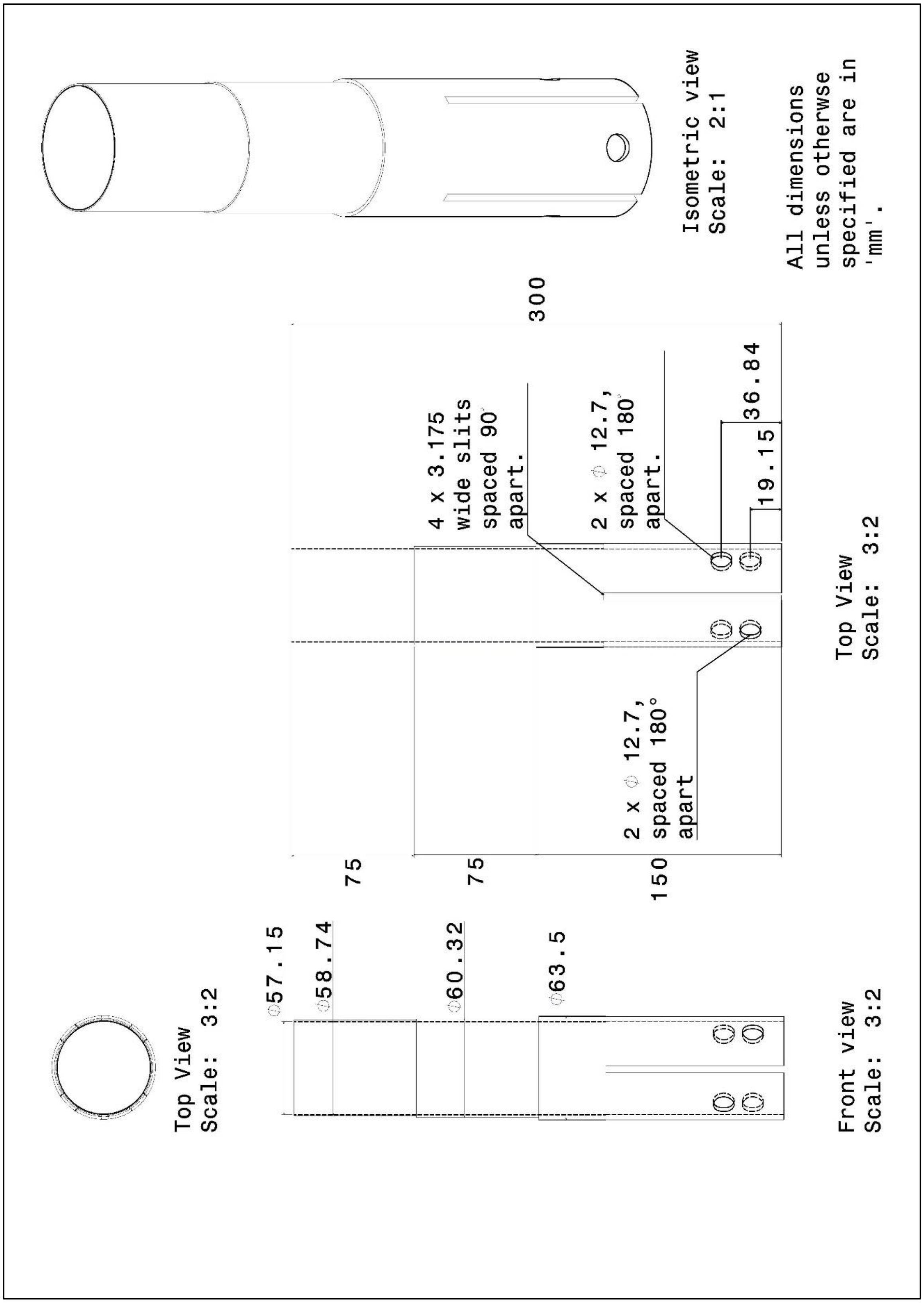

Figure 68: CAD schematic of PA1 extrusion.

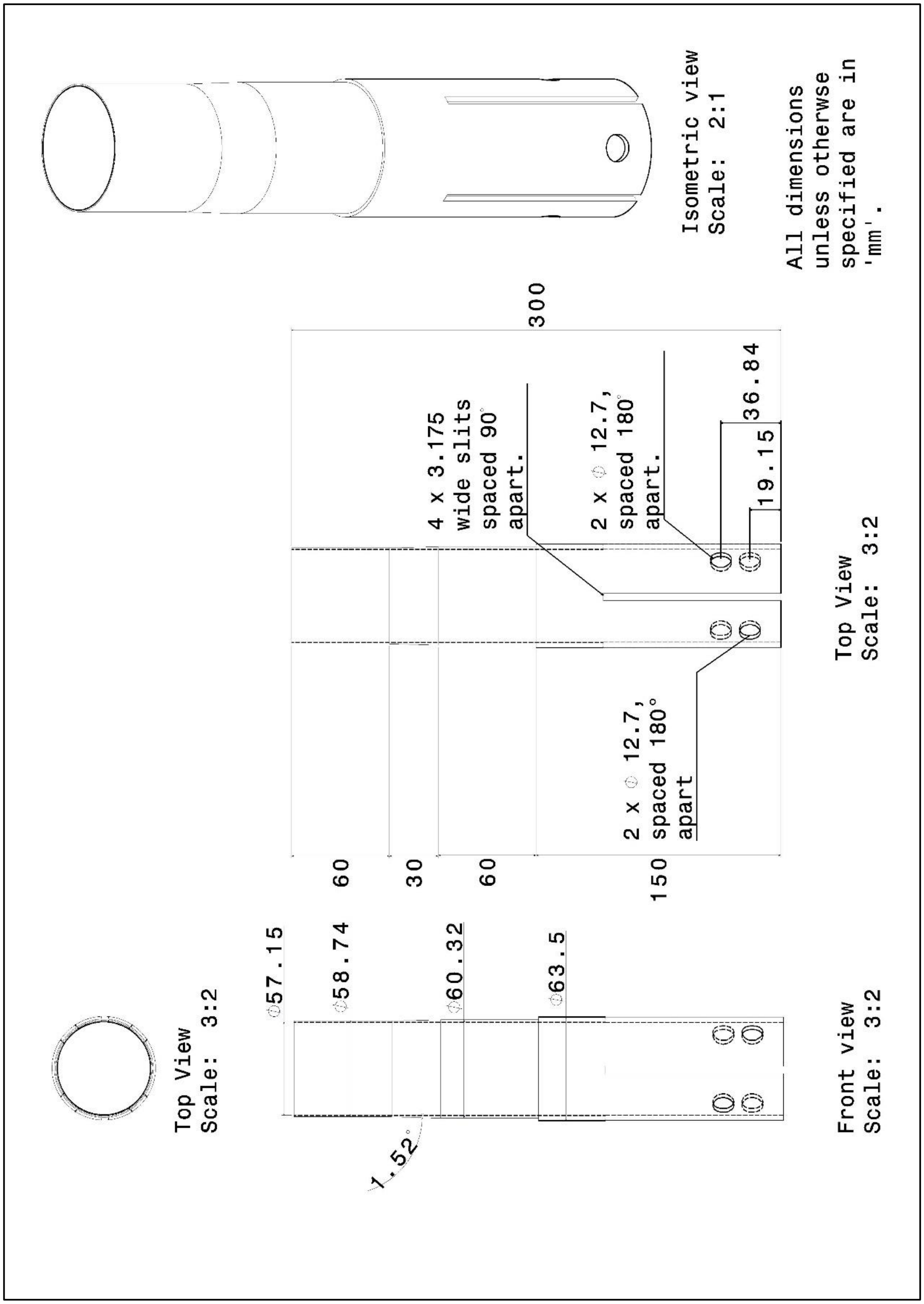

Figure 69: CAD schematic of PA2 extrusion.

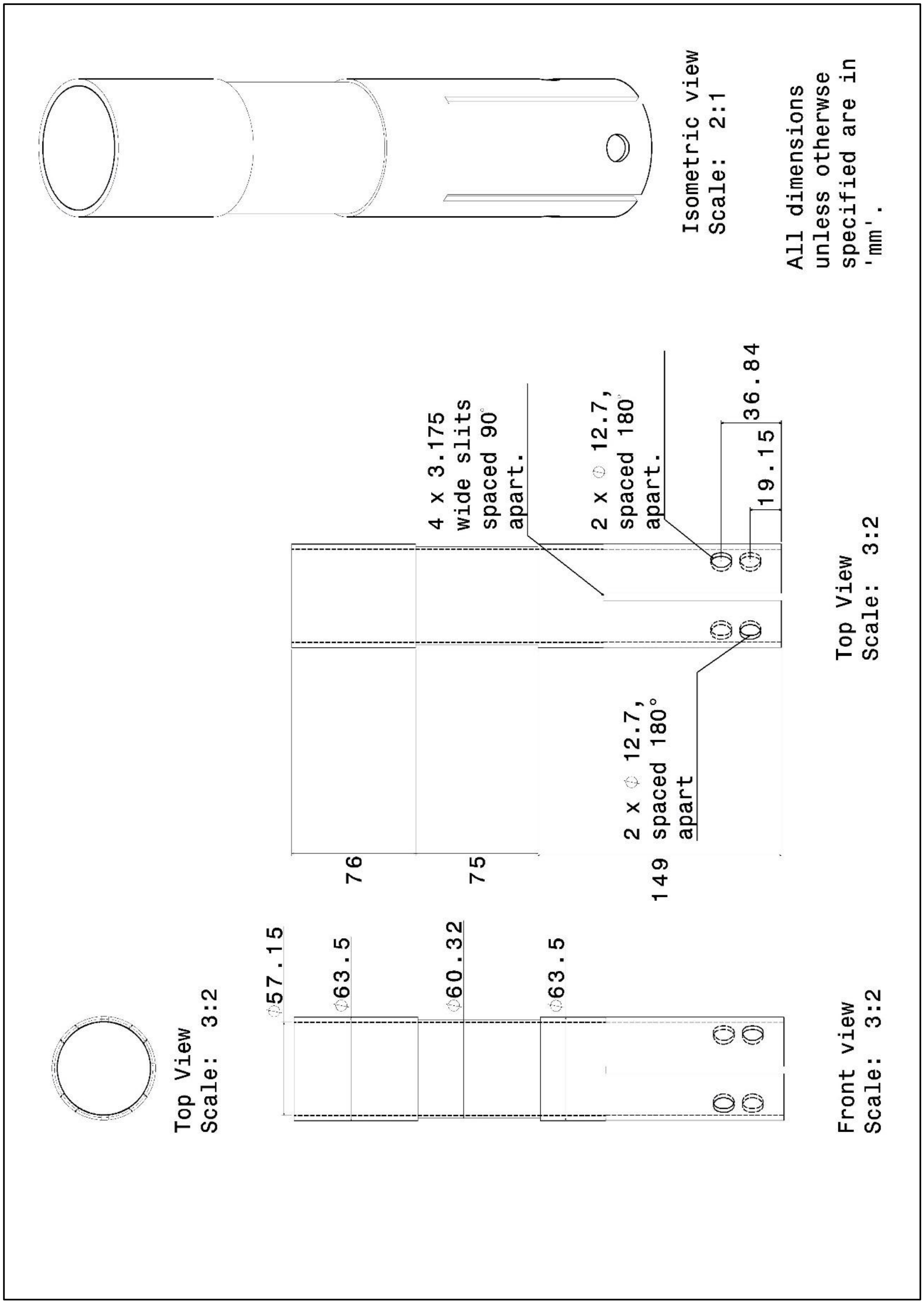

Figure 70: CAD schematic of PA3 extrusion.

Appendix B: Fixturing for Experimental Set-Up

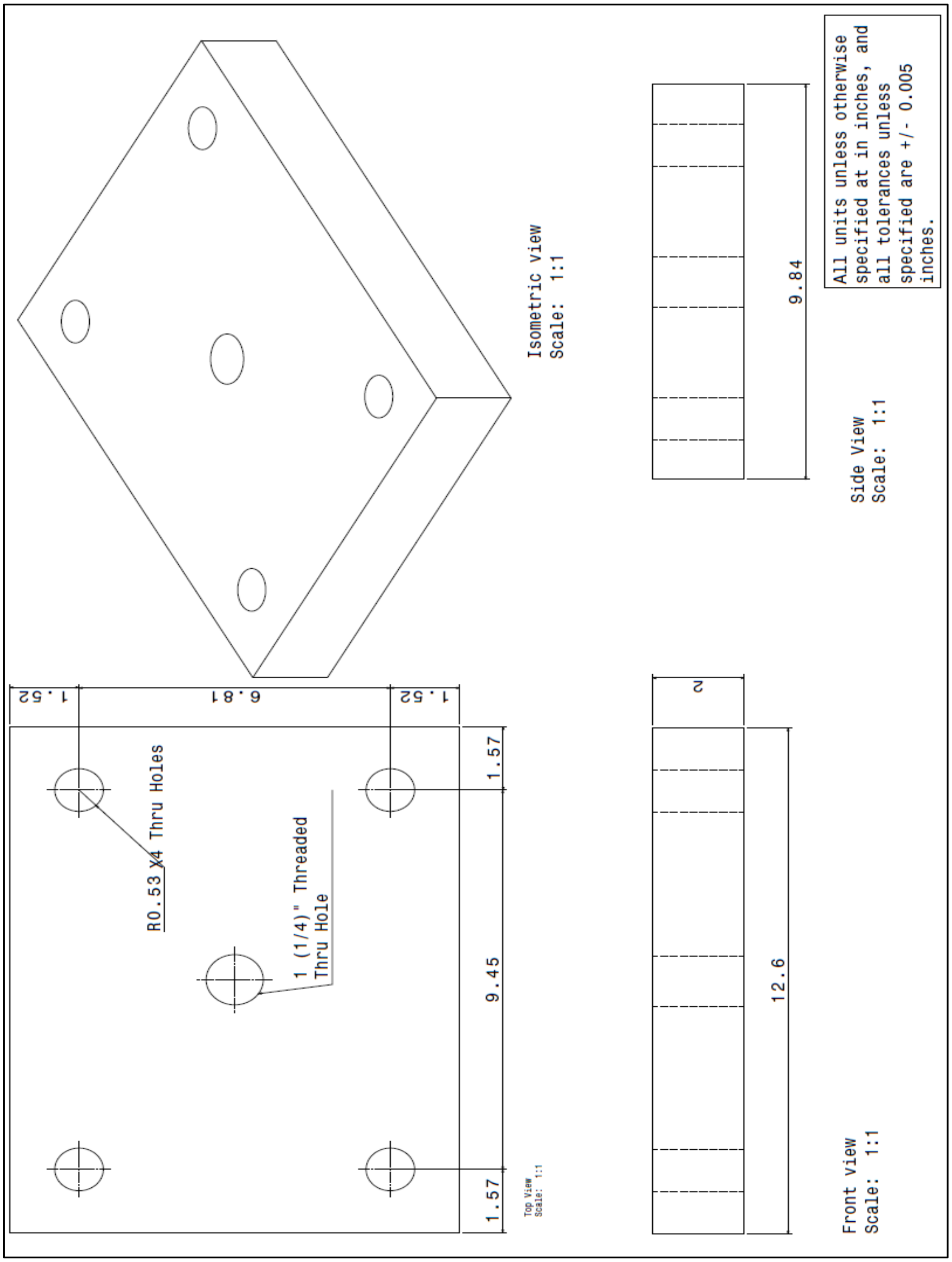

Figure 71: CAD schematic of base plate.

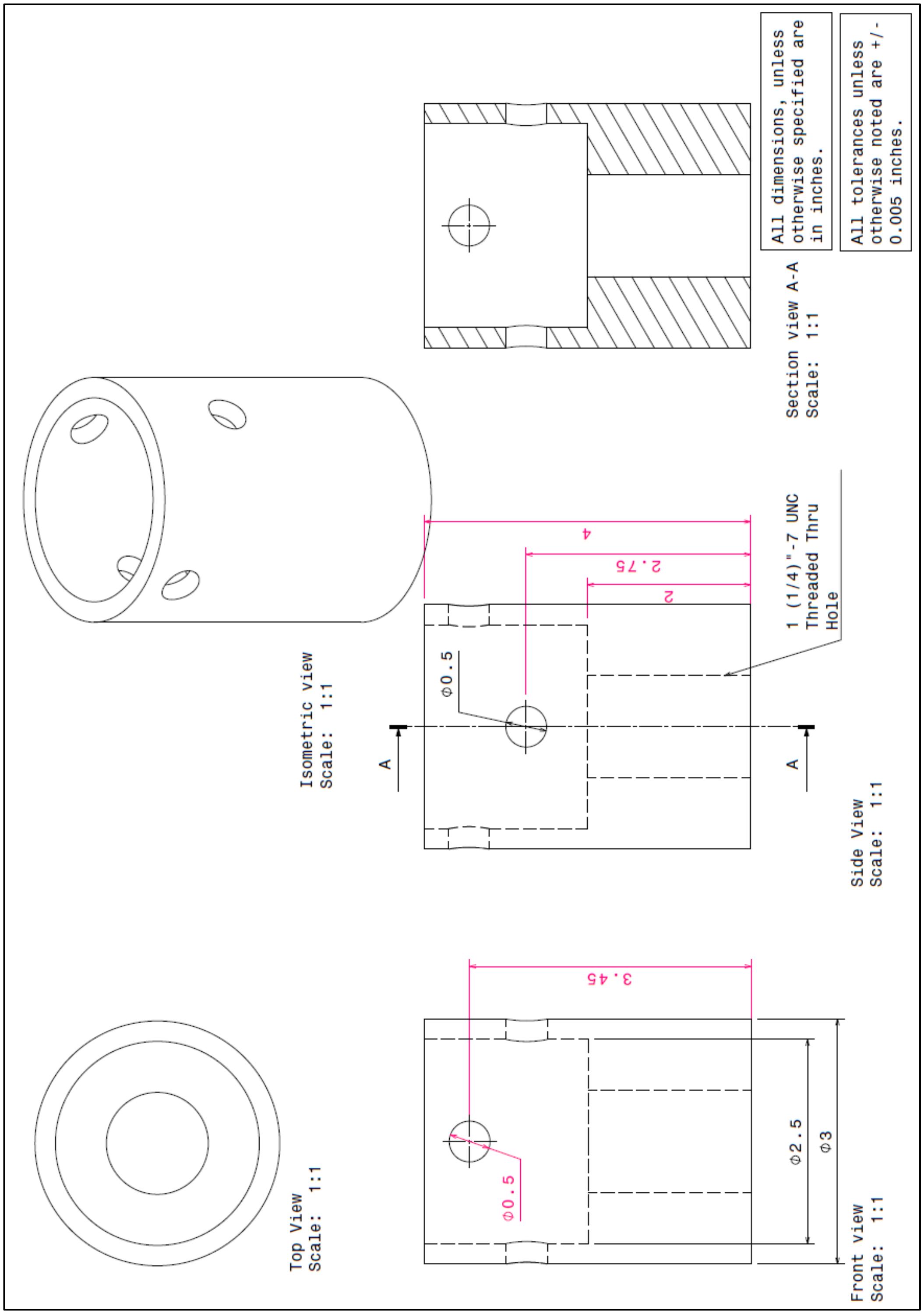

Figure 72: CAD schematic of base chuck.

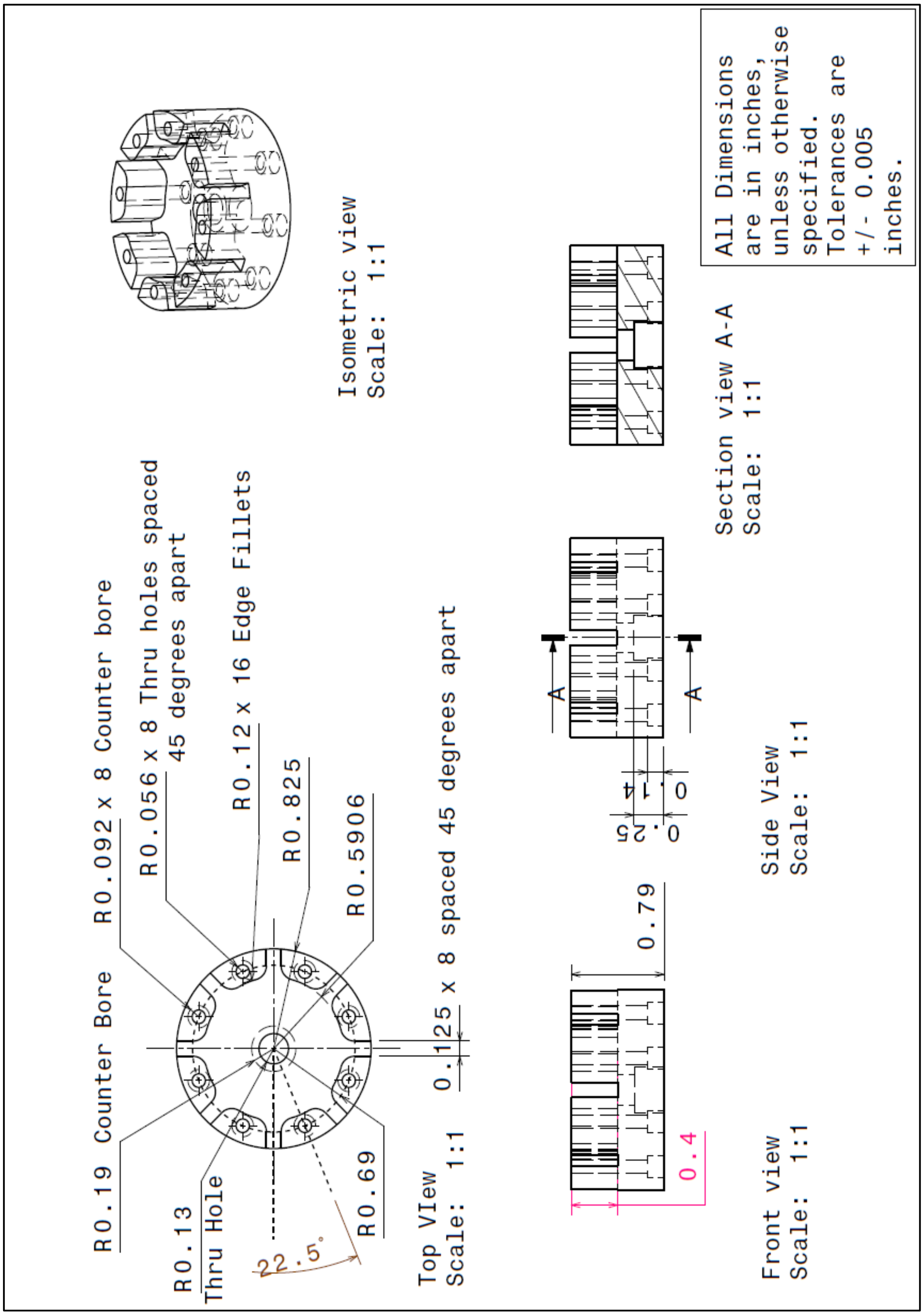

Figure 73: CAD schematic of lower cutter fixture.

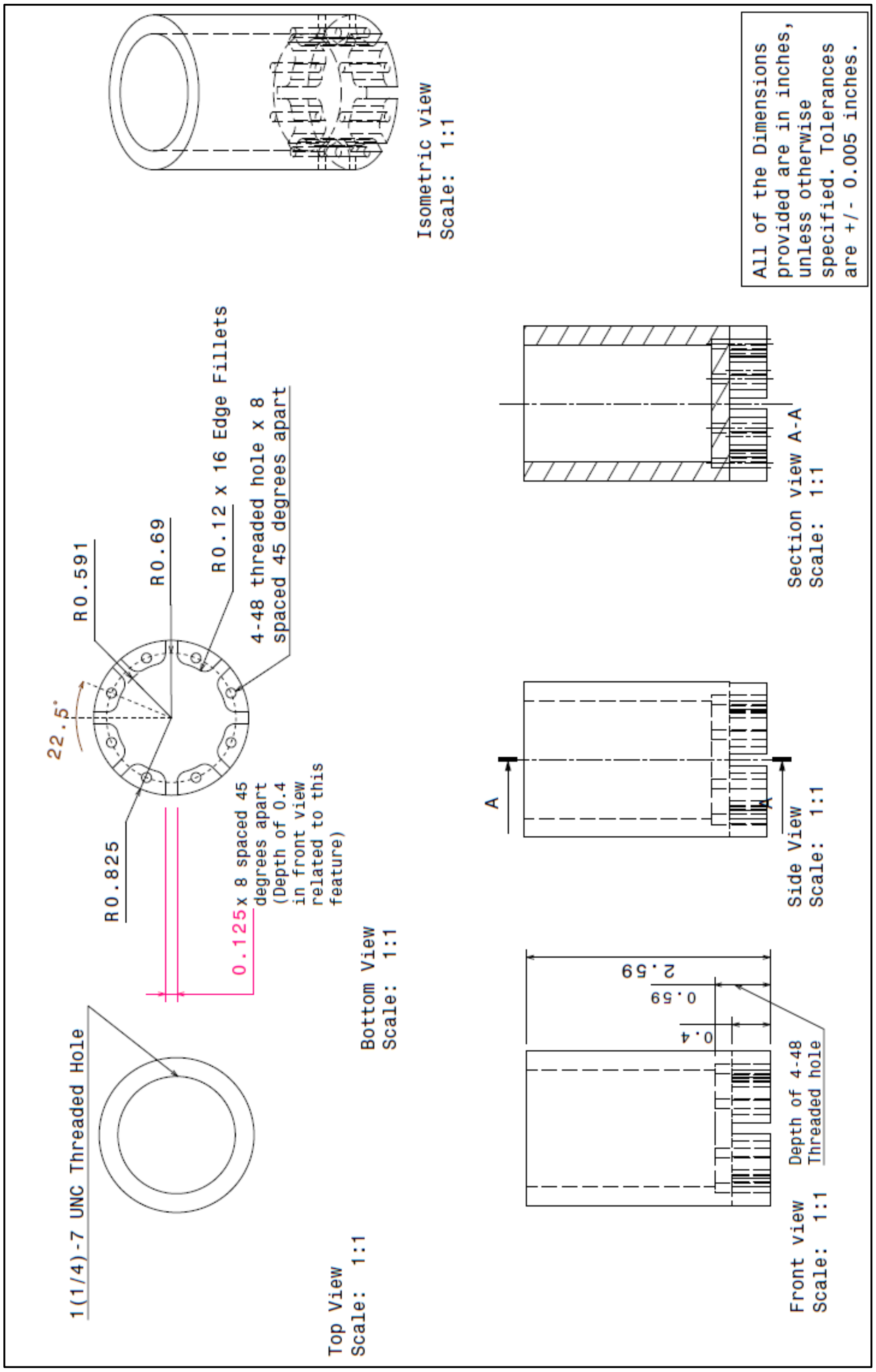

Figure 74: CAD schematic of upper cutter fixture.

Appendix C: Experimental Observations

Table 9: Summary of results for 63.5-3.175 mm extrusions in T6 and T4 temper conditions.

Extrusion thickness [mm]	6061-T6 (as-received)				6061-T4 (annealed)			
	TEA [kJ]	*SEA* [kJ/kg]	P_m [kN]	*TFE* [%]	*TEA* [kJ]	*SEA* [kJ/kg]	P_m [kN]	*TFE* [%]
3.175	7.43	16.61	43.321	93.58	7.19	14.95	40.42	94.60
	7.76	16.67	45.13	93.06	7.06	14.65	41.84	94.30
	7.33	15.59	41.68	87.07	7.28	14.92	40.98	93.90
Average	7.59	16.29	43.34	92.23	7.19	14.84	41.08	94.27

Table 10: Summary of results for 63.5-1.588 mm extrusions in T6 and T4 temper conditions.

Extrusion thickness [mm]	6061-T6 (as-received)				6061-T4 (annealed)			
	TEA [kJ]	*SEA* [kJ/kg]	P_m [kN]	*TFE* [%]	*TEA* [kJ]	*SEA* [kJ/kg]	P_m [kN]	*TFE* [%]
1.588*	3.82	15.40	22.62	91.72	N/A	N/A	N/A	N/A
	3.98	15.88	23.24	94.17	N/A	N/A	N/A	N/A
	3.85	15.35	22.50	91.22	N/A	N/A	N/A	N/A
Average	3.88	15.55	22.79	92.37	N/A	N/A	N/A	N/A

*The T4 counterpart of this extrusion category failed prematurely at the dowel holes as such, performance parameters were not calculated.

Table 11: Summary of results for 63.5-1.25 mm extrusions in T6 and T4 temper conditions.

Extrusion thickness [mm]	6061-T6 (as-received)				6061-T4 (annealed)			
	TEA [kJ]	*SEA* [kJ/kg]	P_m [kN]	*TFE* [%]	*TEA* [kJ]	*SEA* [kJ/kg]	P_m [kN]	*TFE* [%]
1.25	2.87	14.84	15.84	82.73	1.90	10.33	10.66	76.25
	2.95	15.52	16.85	83.96	2.03	10.11	11.24	75.52
	2.80	14.86	15.58	84.00	2.06	10.08	11.94	86.00
Average	2.88	15.07	16.09	83.56	2.00	10.17	11.28	79.25

Table 12: Summary of results for 63.5-PA1 extrusions in T6 and T4 temper conditions.

Extrusion profile	6061-T6 (as-received)				6061-T4 (annealed)			
	TEA [kJ]	*SEA* [kJ/kg]	P_m [kN]	*TFE* [%]	*TEA* [kJ]	*SEA* [kJ/kg]	P_m [kN]	*TFE* [%]
PA1	3.88	13.58	21.20	N/A	3.49	12.44	19.55	N/A
	3.99	14.47	22.90	N/A	3.39	11.99	19.23	N/A
	3.89	14.05	28.92	N/A	2.69	9.70	15.33	N/A
Average	3.88	14.04	22.67	N/A	3.19	11.37	18.04	N/A

**TFE* was not computed as the force response was designed to vary through the domain of displacement.

Table 13: Summary of results for 63.5-PA2 extrusions in T6 and T4 temper conditions.

Extrusion profile	6061-T6 (as-received)				6061-T4 (annealed)			
	TEA [kJ]	*SEA* [kJ/kg]	P_m [kN]	*TFE* [%]	*TEA* [kJ]	*SEA* [kJ/kg]	P_m [kN]	*TFE* [%]
PA2	3.11	11.58	17.32	N/A	2.89	10.53	16.05	N/A
	3.42	12.67	19.31	N/A	2.10	7.70	11.63	N/A
	2.94	10.86	16.49	N/A	2.23	8.12	12.29	N/A
Average	3.16	11.70	17.70	N/A	2.41	8.77	13.32	N/A

**TFE* was not computed as the force response was designed to vary through the domain of displacement.

Table 14: Summary of results for 63.5.PA3 extrusions in T6 and T4 temper conditions.

Extrusion profile	6061-T6 (as-received)				6061-T4 (annealed)			
	TEA [kJ]	*SEA* [kJ/kg]	P_m [kN]	*TFE* [%]	*TEA* [kJ]	*SEA* [kJ/kg]	P_m [kN]	*TFE* [%]
PA3	5.64	13.92	33.64	N/A	5.55	13.55	30.74	N/A
	5.84	14.39	34.47	N/A	5.71	14.13	31.62	N/A
	5.97	14.77	34.50	N/A	5.71	14.10	31.84	N/A
Average	5.82	14.36	34.20	N/A	5.66	13.93	31.40	N/A

**TFE* was not computed as the force response was designed to vary through the domain of displacement.

Table 15: Summary of results for 50.8-3.175 mm extrusions in T6 and T4 temper conditions.

Extrusion thickness [mm]	6061-T6 (as-received)				6061-T4 (annealed)			
	TEA [kJ]	*SEA* [kJ/kg]	P_m [kN]	*TFE* [%]	*TEA* [kJ]	*SEA* [kJ/kg]	P_m [kN]	*TFE* [%]
3.175	8.69	17.94	47.92	92.43	6.71	17.69	37.36	91.42
	8.76	18.15	47.40	93.47	6.82	17.91	38.17	92.22
	8.36	17.14	45.88	93.34	6.60	17.64	37.12	91.64
Average	8.60	17.74	47.07	93.08	6.71	17.75	37.55	91.76

Table 16: Summary of results for 50.8-1.588 mm extrusions in T6 and T4 temper conditions.

Extrusion thickness [mm]	6061-T6 (as-received)				6061-T4 (annealed)			
	TEA [kJ]	*SEA* [kJ/kg]	P_m [kN]	*TFE* [%]	*TEA* [kJ]	*SEA* [kJ/kg]	P_m [kN]	*TFE* [%]
1.588	3.67	18.81	21.09	94.33	N/A	N/A	N/A	N/A
	3.51	17.52	21.59	93.70	N/A	N/A	N/A	N/A
	3.51	17.80	21.63	94.81	N/A	N/A	N/A	N/A
Average	3.56	18.04	21.44	94.28	N/A	N/A	N/A	N/A

*The T4 counterpart of this extrusion category failed prematurely at the dowel holes as such, performance parameters were not calculated.

Table 17: Summary of results for 50.8-1.25 mm extrusions in T6 and T4 temper conditions.

Extrusion thickness [mm]	6061-T6 (as-received)				6061-T4 (annealed)			
	TEA [kJ]	*SEA* [kJ/kg]	P_m [kN]	*TFE* [%]	*TEA* [kJ]	*SEA* [kJ/kg]	P_m [kN]	*TFE* [%]
1.25*	2.62	26.43	14.69	85.64	1.96	13.19	10.94	70.58
	2.41	24.12	13.81	77.89	2.06	13.91	11.34	80.88
	2.62	26.60	14.59	83.87	N/A	N/A	N/A	N/A
Average	2.55	25.72	14.39	82.47	2.01	13.55	11.14	75.73

*One of the extrusions in the T4 counterpart of this category failed prematurely at the pins, as such performance parameters were not calculated for this extrusion. Average values are comprised of the results from the two valid experiments.

Table 18: Summary of results for 50.8-PA1 extrusions in T6 and T4 temper conditions.

Extrusion profile	6061-T6 (as-received)				6061-T4 (annealed)			
	TEA [kJ]	*SEA* [kJ/kg]	P_m [kN]	*TFE* [%]	*TEA* [kJ]	*SEA* [kJ/kg]	P_m [kN]	*TFE* [%]
PA1*	3.75	17.62	24.72	N/A	3.09	14.32	16.93	N/A
	3.43	16.00	20.33	N/A	2.94	13.62	16.13	N/A
	3.61	16.84	20.88	N/A	3.08	14.30	16.65	N/A
Average	3.60	16.82	21.98	N/A	3.04	14.08	16.57	N/A

**TFE* was not computed as the force response was designed to vary through the domain of displacement.

Table 19: Summary of results for 50.8-PA2 extrusions in T6 and T4 temper conditions.

Extrusion profile	6061-T6 (as-received)				6061-T4 (annealed)			
	TEA [kJ]	*SEA* [kJ/kg]	P_m [kN]	*TFE* [%]	*TEA* [kJ]	*SEA* [kJ/kg]	P_m [kN]	*TFE* [%]
PA2*	3.00	13.87	17.62	N/A	2.29	10.71	12.63	N/A
	3.10	14.31	18.96	N/A	2.31	10.90	12.48	N/A
	3.06	14.24	17.81	N/A	2.41	11.25	13.14	N/A
Average	3.05	14.14	18.13	N/A	2.34	10.95	12.75	N/A

**TFE* was not computed as the force response was designed to vary through the domain of displacement.

Table 20: Summary of results for 50.8-PA3 extrusions in T6 and T4 temper conditions.

Extrusion profile	6061-T6 (as-received)				6061-T4 (annealed)			
	TEA [kJ]	*SEA* [kJ/kg]	P_m [kN]	*TFE* [%]	*TEA* [kJ]	*SEA* [kJ/kg]	P_m [kN]	*TFE* [%]
PA3*	N/A	N/A	N/A	N/A	N/A	N/A	N/A	N/A
	N/A	N/A	N/A	N/A	N/A	N/A	N/A	N/A
	N/A	N/A	N/A	N/A	N/A	N/A	N/A	N/A
Average	N/A	N/A	N/A	N/A	N/A	N/A	N/A	N/A

* No parameters were computed for this test category since extrusions failed during experimentation due to inaccurately machined extrusions.

Appendix D: Parametric Scope Measurements

Table 21: Measurements of AA6061-T6-63.5-3.175/PA1/PA2/PA3 mm extrusions.

4-Bladed Quasi Static Tension Cutting					
Material	**Diameter (mm)**	**Inner Diameter (mm)**	**Thickness A (mm)**	**Diameter B (mm)/Length (mm)**	**Diameter C (mm)**
A6061-T6-63.5-3.175-1	63.4	57.36	3.02		
	63.71	57.32	3.195		
	63.65	57.63	3.01		
	63.36	57.71	2.825		
	63.56	57.39	3.085		
	63.536	**57.482**	**3.027**		
A6061-T6-63.5-3.175-2	63.64	57.36	3.14		
	63.76	57.64	3.06		
	63.5	57.71	2.895		
	63.64	57.6	3.02		
	63.64	57.58	3.03		
	63.636	**57.578**	**3.029**		
A6061-T6-63.5-3.175-3	63.7	57.7	3.05		
	63.61	57.16	3.225		
	63.82	57.22	3.3		
	63.57	57.24	3.165		
	63.8	57.13	3.335		
	63.7	**57.29**	**3.215**		
A6061-T6-63.5-3.175-PA2-1	58.52	57.05	0.74	30.91	60.48
	58.31	56.87	0.68	30.86	60.91
	58.52	57.1	0.69	30.75	60.51
	58.31	57.11	0.72	30.58	60.69
	58.32	57.05	0.67	30.68	60.38
	58.396	**57.036**	**0.7**	**30.756**	**60.594**
A6061-T6-63.5-3.175-PA2-2	58.58	57.03	0.76	30.58	60.59
	58.88	57.23	0.71	30.69	60.51
	58.56	57.02	0.7	30.65	60.59
	58.43	57.12	0.72	30.87	60.57
	58.52	57.14	0.75	30.58	60.51
	58.594	**57.108**	**0.728**	**30.674**	**60.554**
A6061-T6-63.5-3.175-PA2-3	58.55	57.2	0.81	30.68	60.52
	58.63	57.11	0.75	30.98	60.54
	58.77	57.02	0.73	30.57	60.41
	58.62	57.23	0.77	30.89	60.57

4-Bladed Quasi Static Tension Cutting					
Material	**Diameter (mm)**	**Inner Diameter (mm)**	**Thickness A (mm)**	**Diameter B (mm)/Length (mm)**	**Diameter C (mm)**
	58.52	57.08	0.63	30.79	60.45
	58.618	**57.128**	**0.738**	**30.782**	**60.498**
A6061-T6-63.5-PA1-1	58.67	56.72	0.68	60.56	63.33
	58.61	57.11	0.79	60.41	63.6
	58.39	57.1	0.77	60.77	63.54
	58.56	57.1	0.81	60.4	63.57
	58.61	57.12	0.71	60.57	63.45
	58.568	**57.03**	**0.752**	**60.542**	**63.498**
A6061-T6-63.5-PA1-2	58.83	57.17	0.71	60.62	63.42
	58.48	57.07	0.64	60.57	63.57
	58.68	57.19	0.7	60.45	63.47
	58.56	57.09	0.75	60.49	63.53
	58.71	57.18	0.73	60.88	63.54
	58.652	**57.14**	**0.706**	**60.602**	**63.506**
A6061-T6-63.5-PA1-3	58.5	57.04	0.7	60.47	63.35
	58.71	57.08	0.77	60.52	63.4
	58.62	56.83	0.79	60.49	63.35
	58.57	57	0.74	60.63	63.4
	58.87	57	0.67	60.45	63.33
	58.654	**56.99**	**0.734**	**60.512**	**63.366**
A6061-T6-63.5-PA3-1	63.64	56.99	3.07	60.61	63.39
	63.37	57.06	3.22	60.59	63.23
	63.22	57.02	3.15	60.62	63.41
	63.3	57.01	3.17	60.65	63.15
	63.57	56.98	3.19	60.8	63.69
	63.42	**57.012**	**3.16**	**60.654**	**63.374**
A6061-T6-63.5-PA3-2	63.62	56.99	3.16	60.63	63.37
	63.2	57.02	3.2	60.64	63.23
	63.21	57	3.2	60.65	63.27
	63.42	56.95	3.23	60.57	63.24
	63.48	57.15	3.16	60.66	63.46
	63.386	**57.022**	**3.19**	**60.63**	**63.314**
A6061-T6-63.5-PA3-3	63.61	57.09	3.11	60.68	63.47
	63.37	57.13	3.17	60.73	63.54
	63.57	56.99	3.17	61.85	63.45
	63.51	56.99	3.18	60.82	63.35
	63.49	56.96	3.21	60.87	63.14
	63.51	**57.032**	**3.168**	**60.99**	**63.39**

Table 22: Measurements of AA6061-T6-63.5-1.588/1.25 mm extrusions.

4-Bladed Quasi Static Tension Cutting			
Material	**Diameter (mm)**	**Inner Diameter (mm)**	**Thickness (mm)**
A6061-T6-63.5-1.59-1	63.61	60.15	1.55
	63.41	59.71	1.54
	63.73	60.1	1.57
	63.66	59.99	1.56
	63.52	60.24	1.61
	63.586	**60.038**	**1.566**
A6061-T6-63.5-1.59-2	63.54	60.2	1.59
	63.56	60.14	1.62
	63.4	60.1	1.58
	63.6	60.13	1.57
	63.58	60.02	1.56
	63.536	**60.118**	**1.584**
A6061-T6-63.5-1.59-3	63.47	60.34	1.58
	63.4	60.13	1.57
	63.52	60.23	1.6
	63.6	60.13	1.59
	63.49	60.15	1.58
	63.496	**60.196**	**1.584**
A6061-T6-63.5-1.25-1	62.65	60.26	1.11
	62.64	60.05	1.25
	62.48	60.33	1.34
	62.65	60.28	1.38
	62.69	60.25	1.09
	62.622	**60.234**	**1.234**
A6061-T6-63.5-1.25-2	62.74	60.02	1.19
	62.84	60.13	1.23
	62.77	60.29	1.12
	62.53	60.37	1.15
	62.76	60.34	1.37
	62.728	**60.23**	**1.212**
A6061-T6-63.5-1.25-3	62.54	59.99	1.15
	62.77	60.09	1.11
	62.74	60.16	1.22
	62.7	60.07	1.17
	62.59	60.33	1.35
	62.668	**60.128**	**1.2**

Table 23: Measurements of AA6061-T4-63.5-3.175/PA1/PA2/PA3 mm extrusions.

4-Bladed Quasi Static Tension Cutting					
Material	**Diameter (mm)**	**Inner Diameter (mm)**	**Thickness A (mm)**	**Diameter B (mm)/Length (mm)**	**Diameter C (mm)**
A6061-T4-63.5-3.175-1	63.71	57.17	3.15		
	63.53	57	3.17		
	63.47	57.15	3.14		
	63.32	57.18	3.12		
	63.41	57.01	3.14		
	63.488	**57.102**	**3.144**		
A6061-T4-63.5-3.175-2	63.47	56.93	3.06		
	63.52	56.94	3.12		
	63.58	57.05	3.13		
	63.7	57.18	3.13		
	63.56	57.27	3.18		
	63.566	**57.074**	**3.124**		
A6061-T4-63.5-3.175-3	63.72	57.16	3.05		
	63.22	57.06	3.09		
	63.77	57.09	3.18		
	63.67	56.91	3.22		
	63.64	56.95	3.25		
	63.604	**57.034**	**3.158**		
A6061-T4-63.5-PA2-1	57.92	57.12	0.77	30.25	60.68
	59.49	57.57	0.83	30.35	60.77
	58.77	56.4	0.81	30.35	60.79
	58.01	56.25	0.85	30.51	60.55
	58.41	56.83	0.82	30.43	60.65
	58.52	**56.834**	**0.816**	**30.378**	**60.688**
A6061-T4-63.5-PA2-2	58.93	56.87	0.76	30.81	60.66
	59.33	57.51	0.81	30.23	60.72
	58.46	56.61	0.77	30.49	60.93
	57.46	57.05	0.75	30.68	60.6
	58.8	56.83	0.84	30.82	60.65
	58.596	**56.974**	**0.786**	**30.606**	**60.712**
A6061-T4-63.5-PA2-3	59.46	57.25	0.79	30.15	60.6
	58.54	56.79	0.89	30.28	60.66
	58.16	57.66	0.73	30.6	60.74
	59.09	57.82	0.71	30.24	60.97
	58.39	56.8	0.85	30.56	60.73
	58.728	**57.264**	**0.794**	**30.366**	**60.74**

4-Bladed Quasi Static Tension Cutting					
Material	**Diameter (mm)**	**Inner Diameter (mm)**	**Thickness A (mm)**	**Diameter B (mm)/Length (mm)**	**Diameter C (mm)**
A6061-T4-63.5-PA1-1	58.5	56.72	0.74	60.58	63.42
	59.1	57.27	0.89	60.53	63.31
	58.95	57.4	0.8	60.77	63.38
	58.48	57.43	0.77	60.74	63.32
	58.99	56.91	0.79	60.53	63.67
	58.804	**57.146**	**0.798**	**60.72**	**63.42**
A6061-T4-63.5-PA1-2	58.56	56.4	0.89	60.54	63.5
	59.42	57.47	0.83	60.63	63.39
	58.39	57.24	0.84	60.76	63.73
	58.12	57.55	0.83	60.81	63.67
	58.75	56.9	0.87	60.55	63.77
	58.648	**57.112**	**0.852**	**60.658**	**63.612**
A6061-T4-63.5-PA1-3	58.23	56.64	0.74	60.97	63.5
	59.03	57.33	0.73	60.75	63.39
	58.4	57.47	0.78	60.68	63.85
	58.47	56.51	0.83	60.79	63.87
	58.87	57.26	0.71	60.59	63.34
	58.6	**57.042**	**0.758**	**60.756**	**63.59**
A6061-T4-63.5-PA3-1	63.51	56.96	3.26	60.67	63.84
	63.6	56.91	3.26	60.75	63.49
	63.42	57.22	3.16	60.89	63.58
	63.52	57.09	3.21	60.73	63.89
	63.74	57.03	3.31	60.92	63.74
	63.558	**57.042**	**3.24**	**60.792**	**63.708**
A6061-T4-63.5-PA3-2	63.65	57.15	3.19	60.63	63.39
	63.63	56.98	3.29	60.84	63.31
	63.57	56.92	3.12	60.78	63.19
	63.47	57	3.23	60.88	63.91
	63.57	57.16	3.2	60.7	63.86
	63.578	**57.042**	**3.206**	**60.766**	**63.532**
A6061-T4-63.5-PA3-3	63.57	56.99	3.18	60.73	63.76
	63.64	56.96	3.11	60.65	63.56
	63.43	57.08	3.16	60.81	63.82
	63.52	56.98	3.19	60.52	63.25
	63.6	57	3.18	60.64	63.07
	63.552	**57.002**	**3.164**	**60.67**	**63.492**

Table 24: Measurements of AA6061-T6-63.5-1.588/1.25 mm extrusions.

4-Bladed Quasi Static Tension Cutting			
Material	**Diameter (mm)**	**Inner Diameter (mm)**	**Thickness (mm)**
A6061-T4-63.5-1.59-1	63.27	60.33	1.61
	63.58	59.96	1.6
	63.76	59.99	1.69
	63.44	60.26	1.67
	63.42	60.12	1.6
	63.494	**60.132**	**1.634**
A6061-T4-63.5-1.59-2	63.3	59.99	1.59
	63.39	60.15	1.62
	63.43	60.05	1.68
	63.55	60.25	1.65
	63.54	60.21	1.6
	63.442	**60.13**	**1.628**
A6061-T4-63.5-1.59-3	63.71	60.46	1.64
	63.68	60.53	1.64
	63.46	59.99	1.66
	63.34	60.26	1.66
	63.81	60.5	1.67
	63.6	**60.348**	**1.654**
A6061-T4-63.5-1.25-1	62.6	60.47	1.26
	62.9	60.36	1.35
	62.85	60.06	0.99
	62.84	60.05	1.12
	62.54	60.3	1.13
	62.746	**60.248**	**1.17**
A6061-T4-63.5-1.25-2	62.82	60.2	1.11
	62.71	60.16	1.25
	62.59	60.4	1.42
	62.68	60.46	1.35
	62.75	60.16	1.27
	62.71	**60.276**	**1.28**
A6061-T4-63.5-1.25-3	62.77	60.07	1.22
	62.76	59.92	1.33
	62.75	60.19	1.39
	62.87	60.25	1.39
	62.74	59.98	1.18
	62.778	**60.082**	**1.302**

Table 25: Measurements of AA6061-T6-50.8-3.175/PA1/PA2/PA3 mm extrusions.

4-Bladed Quasi Static Tension Cutting					
Material	**Diameter (mm)**	**Inner Diameter (mm)**	**Thickness A (mm)**	**Diameter B (mm)/Length (mm)**	**Diameter C (mm)**
A6061-T6-50.8-3.175-1	50.9	44.3	2.95		
	50.86	44.29	3.27		
	50.85	44.48	3.07		
	50.85	44.33	3.06		
	50.7	44.4	3.24		
	50.832	**44.36**	**3.118**		
A6061-T6-50.8-3.175-2	50.76	44.25	3.26		
	50.84	44.25	3.02		
	50.7	44.47	3.15		
	50.78	44.12	3.27		
	50.76	44.29	2.96		
	50.768	**44.276**	**3.132**		
A6061-T6-50.8-3.175-3	50.81	44.17	3.01		
	50.71	44.3	3.21		
	50.83	44.29	3.22		
	50.82	44.27	3		
	50.79	44.3	2.94		
	50.792	**44.266**	**3.076**		
A6061-T6-50.8-PA2-1	45.79	44.21	0.7	30.22	47.76
	45.72	44.43	0.75	30.48	47.99
	45.94	44.36	0.72	30.58	47.94
	45.8	44.29	0.69	30.59	47.66
	45.8	44.18	0.72	30.68	47.82
	45.81	**44.294**	**0.716**	**30.51**	**47.834**
A6061-T6-50.8-PA2-2	45.93	44.35	0.73	30.28	47.79
	45.75	44.3	0.72	30.36	47.72
	45.81	44.25	0.67	30.26	47.82
	45.81	44.36	0.7	30.48	47.88
	45.76	44.21	0.75	30.46	47.9
	45.812	**44.294**	**0.714**	**30.368**	**47.822**
A6061-T6-50.8-PA2-3	45.69	44.3	0.71	30.5	47.81
	45.83	44.34	0.69	30.28	47.71
	45.81	44.39	0.7	30.45	47.71
	45.92	44.34	0.59	30.36	47.82
	45.71	44.41	0.68	30.38	47.7
	45.792	**44.356**	**0.674**	**30.394**	**47.75**

4-Bladed Quasi Static Tension Cutting					
Material	**Diameter (mm)**	**Inner Diameter (mm)**	**Thickness A (mm)**	**Diameter B (mm)/Length (mm)**	**Diameter C (mm)**
A6061-T6-50.8-PA1 -1	45.71	44.39	0.63	47.67	50.63
	45.77	44.31	0.6	47.82	50.71
	45.81	44.44	0.7	47.8	50.78
	45.74	44.42	0.65	47.71	50.75
	45.85	44.28	0.59	47.76	50.72
	45.776	**44.368**	**0.634**	**47.752**	**50.718**
A6061-T6-50.8-PA1-2	45.83	44.19	0.58	47.72	50.68
	45.71	44.37	0.7	47.75	50.78
	45.77	44.46	0.69	47.92	50.68
	45.83	44.39	0.65	47.81	50.78
	45.81	44.23	0.68	47.84	50.78
	45.79	**44.328**	**0.66**	**47.808**	**50.74**
A6061-T6-50.8-PA1-3	45.76	44.43	0.64	47.7	50.9
	45.86	44.34	0.68	47.8	50.87
	45.78	44.35	0.71	47.77	50.65
	45.81	44.39	0.7	47.7	50.76
	45.84	44.25	0.62	47.73	50.77
	45.81	**44.352**	**0.67**	**47.74**	**50.79**
A6061-T6-50.8-PA3-1	50.83	44.43	2.94	46.1	50.93
	50.75	44.19	3.1	46.25	50.84
	50.9	44.36	3.2	46.23	50.76
	50.79	44.38	3.3	46.28	50.6
	50.78	44.38	3.18	46.13	50.87
	50.81	**44.348**	**3.144**	**46.198**	**50.8**
A6061-T6-50.8-PA3-2	50.69	44.28	3.22	46.1	50.8
	50.75	44.3	3.15	46	50.9
	50.77	44.16	3.1	46.14	50.69
	50.9	44.25	3.11	46.15	50.76
	50.84	44.28	2.96	46.15	50.87
	50.79	**44.254**	**3.108**	**46.108**	**50.804**
A6061-T6-50.8-PA3-3	50.76	44.3	3	46.19	50.76
	50.79	44.42	3.22	46.1	50.84
	50.77	44.38	3.29	46.16	50.78
	50.85	44.35	3.23	46.06	50.85
	50.74	44.35	2.91	46.04	50.83
	50.782	**44.36**	**3.13**	**46.11**	**50.812**

Table 26: Measurements of AA6061-T6-50.8-1.588/1.25 mm extrusions.

4-Bladed Quasi Static Tension Cutting			
Material	**Diameter (mm)**	**Inner Diameter (mm)**	**Thickness (mm)**
A6061-T6-50.8-1.59-1	50.72	47.3	1.51
	50.8	47.21	1.6
	51.1	47.4	1.58
	50.76	47.22	1.52
	50.84	47.56	1.54
	50.844	**47.338**	**1.55**
A6061-T6-50.8-1.59-2	50.75	47.6	1.55
	50.72	47.5	1.57
	50.96	47.42	1.67
	50.85	47.34	1.61
	51.02	47.39	1.55
	50.86	**47.45**	**1.59**
A6061-T6-50.8-1.59-3	51	47.39	1.56
	50.8	47.4	1.66
	50.83	47.42	1.52
	50.74	47.37	1.5
	50.74	47.48	1.6
	50.822	**47.412**	**1.568**
A6061-T6-50.8-1.25-1	50.2	47.3	1.17
	50.07	47.5	1.23
	50.21	47.58	1.25
	50.17	47.54	1.14
	50.15	47.39	1.16
	50.16	**47.462**	**1.19**
A6061-T6-50.8-1.25-2	50.05	47.42	1.16
	50.1	47.34	1.21
	50.36	47.39	1.22
	50.06	47.47	1.17
	49.99	47.42	1.24
	50.112	**47.408**	**1.2**
A6061-T6-50.8-1.25-3	49.93	47.6	1.15
	50.34	47.57	1.16
	50.16	47.45	1.17
	50.04	47.35	1.2
	50.09	47.53	1.22
	50.112	**47.5**	**1.18**

Table 27: Measurements of AA6061-T4-50.8-3.175/PA1/PA2/PA3 mm extrusions.

4-Bladed Quasi Static Tension Cutting					
Material	**Diameter (mm)**	**Inner Diameter (mm)**	**Thickness (mm)**	**Diameter B (mm) /Length (mm)**	**Diameter C (mm)**
A6061-T4-50.8-3.175-1	50.67	44.22	3.04		
	50.82	44.45	3.05		
	50.84	44.2	3.09		
	50.82	44.38	3.2		
	50.89	44.38	3.21		
	50.808	**44.326**	**3.118**		
A6061-T4-50.8-3.175-2	50.78	44.41	2.94		
	50.83	44.31	3.07		
	50.92	44.22	3.12		
	50.91	44.37	3.24		
	50.67	44.48	3.26		
	50.822	**44.358**	**3.126**		
A6061-T4-50.8-3.175-3	50.87	44.36	2.95		
	50.82	44.34	2.96		
	50.89	44.27	3.03		
	50.9	44.35	3.12		
	50.83	44.44	3.25		
	50.862	**44.352**	**3.062**		
A6061-T4-50.8-PA2-1	45.9	44.33	0.59	30.59	47.76
	45.74	44.09	0.75	30.58	47.72
	45.42	44.45	0.7	30.78	47.83
	45.18	44.34	0.69	30.79	47.63
	45.95	44.69	0.52	30.85	47.76
	45.638	**44.38**	**0.65**	**30.718**	**47.74**
A6061-T4-50.8-PA2-2	45.79	44.2	0.53	30.7	47.81
	45.61	44.31	0.59	30.5	47.9
	45.69	44.39	0.61	30.58	47.81
	45.88	44.71	0.72	30.59	47.83
	45.78	44.41	0.59	30.5	47.66
	45.75	**44.404**	**0.608**	**30.574**	**47.802**
A6061-T4-50.8-PA2-3	45.78	44.27	0.72	30.52	47.71
	45.59	44.41	0.73	30.46	47.69
	45.88	44.39	0.63	30.5	47.76
	45.67	44.5	0.64	30.47	47.8
	45.83	44.6	0.64	30.47	47.7
	45.75	**44.434**	**0.672**	**30.484**	**47.732**

4-Bladed Quasi Static Tension Cutting					
Material	**Diameter (mm)**	**Inner Diameter (mm)**	**Thickness (mm)**	**Diameter B (mm) /Length (mm)**	**Diameter C (mm)**
A6061-T4-50.8-PA1-1	45.87	44.41	0.76	47.71	50.88
	45.89	44.53	0.69	47.66	50.73
	45.81	44.48	0.62	47.72	50.67
	45.78	44.25	0.74	47.7	50.92
	45.97	44.33	0.74	47.7	50.87
	45.864	**44.4**	**0.71**	**47.698**	**50.814**
A6061-T4-50.8-PA1-2	45.75	44.43	0.69	47.66	50.73
	45.89	44.34	0.64	47.72	50.96
	45.74	44.31	0.72	47.77	51
	45.81	44.41	0.78	47.63	50.83
	45.77	44.2	0.69	47.81	50.72
	45.792	**44.338**	**0.704**	**47.718**	**50.848**
A6061-T4-50.8-PA1-3	45.81	44.25	0.79	47.7	50.77
	45.76	44.42	0.64	47.96	50.87
	45.82	44.21	0.63	47.85	50.85
	45.87	44.32	0.72	47.69	50.77
	45.72	44.29	0.71	47.68	50.8
	45.796	**44.298**	**0.698**	**47.776**	**50.812**
A6061-T4-50.8-PA3-1	50.99	44.37	3.07	46.31	50.89
	50.8	44.42	3.08	46.19	50.78
	50.89	44.32	3.29	46.15	50.89
	50.8	44.47	3.27	46.34	50.91
	50.76	44.09	3.13	46.08	50.87
	50.848	**44.334**	**3.168**	**46.214**	**50.868**
A6061-T4-50.8-PA3-2	50.81	44.49	3.03	46.12	50.95
	50.85	44.19	3.04	46.19	50.9
	50.71	44.16	3.05	46.19	50.87
	50.9	44.18	3.21	46.22	50.78
	50.87	44.43	3.22	46	50.83
	50.828	**44.29**	**3.11**	**46.144**	**50.866**
A6061-T4-50.8-PA3-3	50.9	44.3	2.96	46.08	50.86
	50.86	44.26	3.18	46.13	50.86
	50.83	44.4	3.31	46.03	50.87
	50.87	44.33	3.21	46.18	50.78
	50.75	44.17	3.02	46.2	50.73
	50.842	**44.292**	**3.136**	**46.124**	**50.82**

Table 28: Measurements of AA6061-T4-50.8-1.588/1.25 mm extrusions.

4-Bladed Quasi Static Tension Cutting			
Material	**Diameter (mm)**	**Inner Diameter (mm)**	**Thickness (mm)**
A6061-T4-50.8-1.59-1	50.9	47.3	1.56
	50.8	47.42	1.55
	51.01	47.5	1.7
	50.87	47.32	1.48
	50.92	47.42	1.56
	50.9	**47.392**	**1.57**
A6061-T4-50.8-1.59-2	50.91	47.43	1.59
	50.84	47.39	1.61
	50.92	47.47	1.63
	50.9	47.44	1.55
	50.82	47.52	1.58
	50.878	**47.45**	**1.592**
A6061-T4-50.8-1.59-3	50.8	47.39	1.58
	50.84	47.4	1.64
	50.96	47.42	1.57
	51.03	47.44	1.53
	50.7	47.51	1.56
	50.866	**47.432**	**1.576**
A6061-T4-50.8-1.25-1	50.13	47.31	1.15
	50.09	47.4	1.25
	50.12	47.49	1.21
	50.09	47.29	1.19
	50.05	47.4	1.14
	50.096	**47.378**	**1.188**
A6061-T4-50.8-1.25-2	50.01	47.61	1.12
	50.1	47.41	1.25
	50.13	47.48	1.26
	50.12	47.35	1.22
	50.11	47.38	1.18
	50.094	**47.446**	**1.206**
A6061-T4-50.8-1.25-3	50.17	47.5	1.05
	50.04	47.33	1.2
	50.15	47.45	1.22
	50.2	47.35	1.25
	50.16	47.36	1.19
	50.144	**47.398**	**1.182**

Vita Auctoris

NAME: Anthony Gudisey

PLACE OF BIRTH: Bangalore, India

YEAR OF BIRTH: 1995

EDUCATION: St. Josephs High School, Windsor, ON, 2013

University of Windsor, B.A.Sc., Windsor, ON, 2017

University of Windsor, M.A.Sc., Windsor, ON, 2021